COHERENT STRUCTURES IN PLASMA TURBULENCE: PERSISTENCE, INTERMITTENCY, AND CONNECTIONS WITH OBSERVATIONS

by

Kurt W. Smith

A dissertation submitted in partial fulfillment of
the requirements for the degree of

Doctor of Philosophy

(Physics)

at the

UNIVERSITY OF WISCONSIN–MADISON

2011

ACKNOWLEDGMENTS

To Paul Terry, my adviser: for your patient guidance and helpful instruction; for the stimulating conversations and for honing my physical intuition; and for motivating the topic of study all those years ago. I cannot claim one good idea in this work as solely my own, and that is, perhaps, as it should be.

To my family and friends: for your support and, at times, bewildered amusement at something I cannot quite explain to you.

To my wife, Ellen: quite simply, this humble work would not exist without you. Your encouragement and support have propped me up and kept me going. I love you.

To our daughter, Zélie: if you are reading this, it is probably because you did something you shouldn't have and reading this was the easiest punishment among the alternatives. Regardless, you should know that I started writing this two weeks after you were born, and defended the day before you turned six months. So you can consider this baby your sibling. I love you, too.

LIST OF FIGURES

COHERENT STRUCTURES IN PLASMA TURBULENCE: PERSISTENCE, INTERMITTENCY, AND CONNECTIONS WITH OBSERVATIONS

Kurt W. Smith

Under the supervision of Professor Paul W. Terry
At the University of Wisconsin-Madison

Long-lived coherent structures in small-scale plasma turbulence are considered in the context of spatial intermittency. Connections are made with observations of anomalous pulsar signal scintillation in the interstellar medium (ISM).

Anomalous scaling of pulsar signal widths with dispersion measure indicate that integrated electron density differences do not follow a Gaussian distribution as expected. If the density difference follows a Lévy distribution then the pulsar signal scaling can be brought into a consistent theoretical framework. The scales at which these non-Gaussian density fluctuations are inferred to exist are near the ion sound gyroradius ρ_s.

We propose a kinetic Alfvén wave (KAW) turbulence model that is known to produce intermittent structures at scales near $10\rho_s$ and smaller. It is shown via two-timescale analysis that localized structures are able to persist for timescales long in comparison to typical turbulence timescales. Assuming equipartition between magnetic and internal energies, it is shown that the probability density function for density gradients around a coherent structure admits a Lévy distribution.

Results of numerical simulations of the KAW system are presented. A structure segmentation method based on ψ field topology is described. The method allows the separation of localized flux tubes from the rest of the turbulent domain. The flux tubes selected by the method have an excess of energy density; the localizations of the current, magnetic, and electron density fields are shown to correspond to expectations; and the structure cores are quiescent for many eddy turnover times. These results confirm key predictions of the two-timescale analysis.

The kurtosis and PDFs of simulation ensembles for density, density gradient, current, and magnetic fields are presented. The density gradient field is shown to be strongly non-Gaussian, even though the density field is consistently Gaussian. Specific values of damping parameters suppress filamentary

structures and favor elongated density gradient sheets. Simulation ensembles in the sheet regime yield statistics similar to the filamentary regime: both have non-Gaussian density gradients. This suggests that non-Gaussian statistics are robust to variation in damping parameters, and lends credence to the claim that small-scale electron density gradients in the ISM have non-Gaussian statistics.

Paul W. Terry

ABSTRACT

Long-lived coherent structures in small-scale plasma turbulence are considered in the context of spatial intermittency. Connections are made with observations of anomalous pulsar signal scintillation in the interstellar medium (ISM).

Anomalous scaling of pulsar signal widths with dispersion measure indicate that integrated electron density differences do not follow a Gaussian distribution as expected. If the density difference follows a Lévy distribution then the pulsar signal scaling can be brought into a consistent theoretical framework. The scales at which these non-Gaussian density fluctuations are inferred to exist are near the ion sound gyroradius ρ_s.

We propose a kinetic Alfvén wave (KAW) turbulence model that is known to produce intermittent structures at scales near $10\rho_s$ and smaller. It is shown via two-timescale analysis that localized structures are able to persist for timescales long in comparison to typical turbulence timescales. Assuming equipartition between magnetic and internal energies, it is shown that the probability density function for density gradients around a coherent structure admits a Lévy distribution.

Results of numerical simulations of the KAW system are presented. A structure segmentation method based on ψ field topology is described. The method allows the separation of localized flux tubes from the rest of the turbulent domain. The flux tubes selected by the method have an excess of energy density; the localizations of the current, magnetic, and electron density fields are shown to correspond to expectations; and the structure cores are quiescent for many eddy turnover times. These results confirm key predictions of the two-timescale analysis.

The kurtosis and PDFs of simulation ensembles for density, density gradient, current, and magnetic fields are presented. The density gradient field is shown to be strongly non-Gaussian, even though the density field is consistently Gaussian. Specific values of damping parameters suppress filamentary structures and favor elongated density gradient sheets. Simulation ensembles in the sheet regime yield statistics similar to the filamentary regime: both have non-Gaussian density gradients. This suggests that non-Gaussian statistics are robust to variation in damping parameters, and lends credence to the claim that small-scale electron density gradients in the ISM have non-Gaussian statistics.

1 INTRODUCTION AND MOTIVATION

Spatial intermittency in turbulence is widely observed in nature, in experiment, and in numerical simulations. To cite just a few examples: Jupiter's great red spot (Marcus, 1988); persistent structures in plane flow; vorticity enhancement via vortex-tube stretching, as in tornadoes (Laval et al., 2001); intermittent "blobs" in the Large Plasma Device (Carter, 2006); intermittency in the MST reversed field pinch (Marrelli et al., 2005); and long-lived coherent structures observed in many numerical studies (McWilliams, 1984; Kinney et al., 1995; Waleffe, 1998, 2003).

The Kolmogorov 1941 theory of universal scaling in hydrodynamic turbulence (K41) (Kolmogorov, 1941) does not account for spatial intermittency. K41 implicitly assumes that the energy transfer rate ϵ is constant everywhere in space, and assumes that the energy-containing structures are space-filling at all scales. Observations indicate intermittent structures exist predominantly at small scales relative to an energy injection scale, and are not space-filling. Models have been proposed to account for intermittency in the K41 framework. One such model is the β model (Frisch et al., 1978) which argues for a fractal dimension to account for the non-space filling nature of Navier-Stokes turbulence. The β model is incomplete, however, in that it provides no means to calculate the fractal dimension of intermittent turbulence. Later models (She and Leveque, 1994) provided a complete one-parameter model based on structure functions; this model has justification in experiment.

Models of intermittency are generally phenomenological and statistical in nature. They do not describe intermittent structures locally; neither do they account for intermittent structure persistence in the midst of a turbulent background. By not describing detailed physics of intermittent structures, phenomenological theories do not completely characterize all aspects of inter-

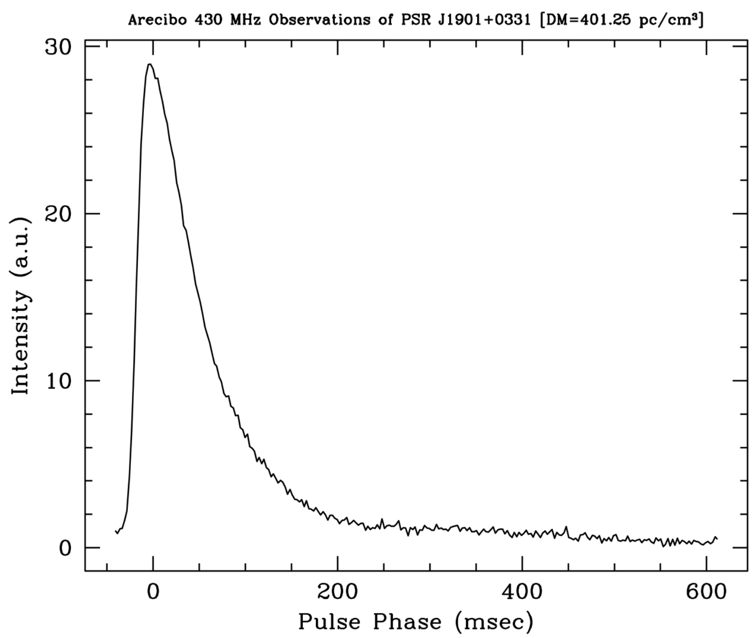

Figure 1.1: Representative pulsar signal intensity vs. time.

mittent structures in turbulence. The present work aims to take initial steps to describe intermittent structures locally in a simple turbulent system, and identify their persistence mechanism.

Besides studying the local physics of intermittent structures and the means by which they persist in turbulence, it is natural to consider the effects that these intermittent structures have on physical processes. Figure 1.1[1] shows a pulsar signal intensity as detected at Earth at 430 MHz. The signal has a sharp rise and a long tail. The tail results from random refractions of the rf signal when interacting with electron density fluctuations along the line of sight between the pulsar and Earth. It is possible to infer features of the statistical distribution of electron density from the shape of pulsar signals (Williamson, 1972; Sutton, 1971; Lee and Jokipii, 1975a). If it is assumed that integrated electron density

[1] From Boldyrev and Gwinn (2003a), used with permission.

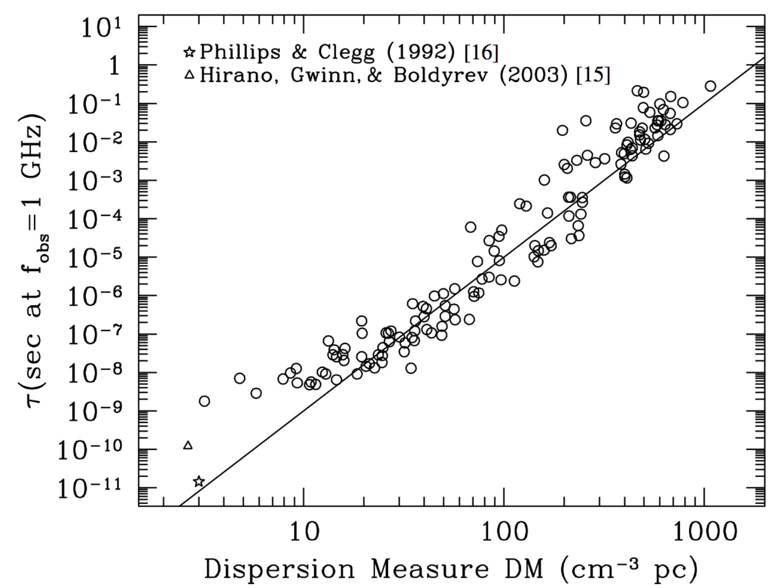

Figure 1.2: Pulsar signal width τ vs. dispersion measure DM.

differences, $\int \mathrm{d}z\ [n(\mathbf{x}_1, z) - n(\mathbf{x}_2, z)]$, are distributed according to a Gaussian distribution, then it can be shown that the temporal width τ of pulsar signals scale with dispersion measure, $DM = \int \mathrm{d}z\, n$, to the second power. Figure 1.2[2] plots on log-log axes τ versus DM for many pulsars. The line of best fit goes like DM^4, not consistent with electron density differences being Gaussian distributed. If it is postulated that electron density differences are distributed according to a Lévy distribution, then the $\tau \propto DM^4$ scaling can be recovered in a consistent theoretical framework (Boldyrev and Gwinn, 2003a). A Lévy distribution is a species of non-Gaussian distributions that is stable and characterized by a power-law tail that render the distribution non-integrable. In this work, we propose that intermittent density gradient fluctuations in kinetic Alfvén wave (KAW) turbulence may account for the non-Gaussian fluctuations inferred.

[2]From Boldyrev and Gwinn (2003a), used with permission.

The remainder of this chapter serves to motivate (1) the local study of intermittent structures and (2) the effect that intermittent structures have on pulsar scintillation. A brief survey of previous work will be offered, and an outline of the rest of the thesis will conclude the chapter.

1.1 Structures in Decaying Turbulence: Local Physics

Just as there is no generally agreed-upon definition of *turbulence* (Schekochihin et al., 2008), there is no general definition of a *turbulent structure*, and efforts to provide one will likely fail in a number of specific cases. Some central considerations are:

1. Resolving the differences in structures between two-dimensional and three-dimensional domains.

2. Whether structure boundaries should be defined vis-a-vis the intrinsic physics of the system (e.g. boundary shear criteria or separatrix surfaces defined by isocontours of X points), or can be approximated in terms of an external parameter (e.g. isosurfaces of $|\mathbf{B}|^2$ at some adjustable threshold).

3. The extent to which temporal persistence is essential to the definition of a structure; and if so, the means by which structures persist in time, and the processes that govern their creation and destruction.

4. Whether a field's topology is sufficient to define structures (e.g. the X points and O points in a 2D field; the separatrices in a 3D configuration), or if the details of the geometry, gradients, integrated quantities, etc., are necessary to define structures.

5. Whether there is a strict separation between *structure* and turbulence, or if structures are at the large-amplitude, large-area, or temporally-persistent end of an adjustable scale of turbulent fluctuations.

6. The morphology structures assume. The dominant large-amplitude fluctuations at small scales often take the form of isolated coherent filaments or extended sheets. What governs the formation of each structure type?

Over the course of the present work, we will address the above considerations in our efforts to define localized structures in decaying turbulence. Our principal concern with regard to localized structures is understanding the interactions of structures with turbulence, and characterizing the structures that arise in small-scale turbulence. The mechanism by which structures arise and persist in turbulence will be investigated, and techniques to distinguish structures from turbulence will be developed. The local-interaction emphasis is complementary to statistical descriptions of filamentary structures such as approaches based on structure functions (She and Leveque, 1994).

1.2 Background Considerations for Structure Formation

Previous simulations of decaying two-dimensional Navier-Stokes turbulence (McWilliams, 1984, for example) observe the spontaneous emergence of large-amplitude localized coherent structures in the vorticity field. These intermittent structures persist in time and are not disrupted by interactions with surrounding turbulence.

Simulations of decaying MHD turbulence (Kinney et al., 1995) and decaying kinetic Alfvén wave turbulence (Craddock et al., 1991) also see the spontaneous generation of large-amplitude coherent structures in the current density field. The associated magnetic field structures are also large-amplitude. The MHD system studied was incompressible, and the kinetic Alfvén wave system heavily damped density fluctuations, so no conclusions can be drawn from those papers as to the sorts of structures that arise in the density field. As will be discussed in the next section, fluctuations in the density field are of central importance to pulsar scintillation measures.

The coherent structures observed in Craddock et al. (1991), whether elongated sheets or localized filaments, are similar to structures observed in Kinney et al. (1995). In the latter, the randomized flow field initialization gives rise to sheet-like structures. After selective decay of the velocity field energy, the system evolves into a state with sheets and filaments. During the merger of like-signed filaments, large-amplitude sheets arise, limited to the region between the merging filaments. These short-lived sheets exist in addition to the long-lived sheets not associated with the merger of filaments. In Craddock et al. (1991), however, there is no flow; the sheet and filament generation is due to a different mechanism which will be discussed in chapter 2. [3]

Other work (Biskamp and Welter, 1989; Politano et al., 1989) observed the spontaneous generation of current sheets and filaments in numerical solutions, with both Orszag-Tang vortex and randomized initial conditions. These 2D reduced-MHD numerical solutions modeled the evolution of magnetic flux and vorticity with collisional dissipation coefficients η and ν, the resistivity and kinematic viscosity, respectively. The magnetic Prandtl number, ν/η, was set to unity. These systems are incompressible and not suitable for modeling compressible density fluctuations; they do however illustrate the ubiquity of current sheets and filaments, and serve as points of comparison. For Orszag-Tang-like initial conditions with large scale flux tubes smooth in profile, current sheets are preferred at the interfaces between tubes. Tearing instabilities can give rise to filamentary current structures that persist for long times, but the large scale and smoothness of flux tubes do not give rise to strong current filaments localized at the center of the tubes. To see this, consider a given flux

[3]The three-field KAW system does include flow, but for small-scales the flow does not participate strongly in the dominant energy exchange between magnetic and density fields, so the two-field analysis applies to the more general three-field system.

tube, and model it as cylindrically symmetric and monotonically decreasing in r with characteristic radial extent a,

$$\psi(r) = \psi_0 \left[1 - \left(\frac{r}{a} \right)^2 \right],$$

for $0 \lesssim r \lesssim a$. The current is localized at the center with magnitude

$$J = -4 \frac{\psi_0}{a^2}.$$

Thus flux tubes with large radial extent a have a corresponding small current filament at their center. Hence, initial conditions dominated by a few large-scale flux tubes are not expected to have large amplitude current filaments at the flux tube centers, but favor current sheet formation and filaments associated with tearing instabilities in those sheet regions. At X points, current sheet folding and filamentary structures can arise (see, e.g. Biskamp and Welter, 1989, Fig. 10), but these regions are small in area compared to the quiescent flux-tube regions. Note that if, instead of Orszag-Tang-like initial conditions, the initial state is random, one expects some regions with flux tubes that have a small, and therefore a sizable current filament at the center.

Consider now the effect of comparatively large or small η. In the case of large η, the central region of a flux tube is smoothed by collisional damping, thus having a strong suppressive effect on the amplitude of the current filament associated with such a flux tube. Large-amplitude current structures are localized to the interfaces between flux tubes. In the process of mergers between like-signed filaments (and repulsion between oppositely signed filaments), large current sheets are generated at these interfaces, similar to the large-amplitude sheets generated in MHD turbulence during mergers (Kinney et al., 1995). For small η, relatively little suppression of isolated current filaments should occur; if these filaments are spatially separated owning to the buffer provided by their associated flux tube, they can be expected to survive a long time and only be disrupted upon the merger with another large-scale flux tube. Large η, then, allows current sheets to form at the boundaries between flux tubes while suppressing the spatially-separated current filaments at flux tube centers. Small η allows interface sheets and spatially separated filaments to exist.

To understand and quantify filamentary structures, we apply two-timescale analysis to a two-field kinetic Alfvén wave system in chapter 2. We then develop techniques in chapter 4 to separate filamentary structures from surrounding turbulence and sheets. We show that filamentary structures have enhanced energy density and that their core regions are regions of enhanced alignment between $\nabla\psi$ and ∇n. We show particular examples of filamentary structures to give an indication of the variety of coherent localized structures that exist. These filamentary structures are shown to correspond to key predictions of the theory of filamentary structures from chapter 2.

The simple arguments above suggest that the evolution of the large-amplitude structures and their interaction with turbulence is strongly influenced by the damping parameters. In chapter 5 the magnitudes of the damping parameters will be shown to affect the pulsar scintillation scalings. That chapter considers the effect of variations of damping parameters η and μ in detail, and shows the emergence of non-Gaussian density gradient PDFs from Gaussian initial conditions, over a range of η/μ ratios.

1.3 Background Considerations for Pulsar Scintillation

Models of scintillation have a long history. Many (Lee and Jokipii, 1975a,b; Sutton, 1971) carry an implicit or explicit assumption of Gaussian statistics, applying to either the electron density field itself or its autocorrelation function (herein referred to as "Gaussian Models"). Lee and Jokipii (1975a) is a representative approach. The statistics of the two-point correlation function of the index of refraction $\epsilon(\mathbf{r})$, $A(\rho) = \int dz' \, \langle \epsilon(x,z)\epsilon(x+\rho,z') \rangle$ determines, among other effects, the scaling of pulsar signal width τ with dispersion measure DM. The index of refraction $\epsilon(\mathbf{r})$ is a function of electron density fluctuation $n(\mathbf{r})$. The quantity $A(0)$ enters the equations, representing the second moment of the index of refraction. If the distribution function of $\epsilon(\mathbf{r})$ has no second-order moment (as in a Lévy distribution) $A(0)$ is undefined. The assumption of Gaussian statistics leads to a scaling of $\tau \sim DM^2$, which contradicts observation for pulsars with $DM > 30$ cm^{-3} pc. For these distant pulsars, $\tau \sim DM^4$ (Sutton, 1971; Boldyrev and Gwinn, 2003a,b).

To explain the anomalous DM^4 scaling, Sutton (1971) argued that the pulsar signal encounters strongly scattering turbulent regions for longer lines of sight, essentially arguing that the statistics, as sampled by a pulsar signal, are nonstationary. Considering the pulse shape in time, Williamson (1972, 1973, 1974) is unable to match observations with a Gaussian Model of scintillation unless the scattering region is confined to $1/4$ of the line of sight between the pulsar and Earth. These assumptions may have physical basis, since the ISM may not be statistically stationary, being composed of different regions with varying turbulence intensity (Boldyrev and Gwinn, 2005).

The theory of Boldyrev and Gwinn (2003a,b, 2005); Boldyrev and Königl (2006) takes a different approach to explain the anomalous DM^4 scaling by considering Lévy statistics for the density difference (defined below). Lévy distributions are characterized by long tails, and a Lévy distribution has no defined moments greater than first-order [i.e., $A(0)$ is undefined for a Lévy distribution]. The theory recovers the $\tau \sim DM^4$ relation with a statistically stationary electron density field. This theory also does not constrain the scattering region to a fraction of the line-of-sight distance.

The determinant quantity in the theory of Boldyrev et al. is the density difference, $\Delta n = n(\mathbf{x}_1, z) - n(\mathbf{x}_2, z)$. According to this model, if the distribution function of Δn has a power-law decay as $|\Delta n| \to \infty$ and has no second moment, then it is possible to recover the $\tau \sim DM^4$ scaling (Boldyrev and Gwinn, 2003b). Assuming sufficiently smooth fluctuations, Δn can be expressed in terms of the density gradient, $\sigma(z)$: $n(\mathbf{x}_1) - n(\mathbf{x}_2) \simeq \sigma(z) \cdot (\mathbf{x}_1 - \mathbf{x}_2)$. Perhaps more directly, the density gradient enters the ray tracing equations [Eqns. (7) in Boldyrev and Gwinn (2003a)], and is seen to be central to determining the resultant pulsar signal shape and width. This formulation of a scintillation theory does not require the distribution of Δn to be Gaussian or to have a second-order moment.

The notion that the density difference is characterized by a Lévy distribution is a constraint on dynamical models for electron density fluctuations in the ISM. Consequently the question of how a Lévy distribution can arise in electron density fluctuations assumes considerable importance in understanding the ISM.

Previous work has laid the groundwork for answering this question. It has been established that electron density fluctuations associated with interstellar magnetic turbulence undergo a significant change in character near the scale $10\rho_s$, where ρ_s is the ion sound gyroradius (Terry et al., 2001). At larger scales, electron density is passively advected by the turbulent flow of an MHD cascade mediated by nonlinear shear Alfvén waves (Goldreich and Sridhar, 1995). At smaller scales the electron density becomes compressive and the turbulent energy is carried into a cascade mediated by kinetic Alfvén waves (KAW) (Terry et al., 2001). The KAW cascade brings electron density into equipartition with the magnetic field, allowing for a significant increase in amplitude. The conversion to a KAW cascade has been observed in numerical solutions of the gyrokinetic equations (Howes et al., 2006), and is consistent with observations from solar wind turbulence (Leamon et al., 1998; Harmon and Coles, 2005; Bale et al., 2005). Importantly, it puts large amplitude electron density fluctuations (and large amplitude density gradients) at the gyroradius scale ($\sim 10^8 - 10^{10}$ cm), a desirable set of conditions for pulsar scintillation (Boldyrev and Königl, 2006). It is therefore appropriate to consider whether large amplitude non-Gaussian structures can arise in KAW turbulence.

The previous studies of filament generation in KAW turbulence leave significant unanswered questions relating to structure morphology and its effect on scintillation. It is well established that MHD turbulence admits structures that are both filament-like and sheet-like. Can sheet-like structures arise in KAW turbulence? If so, what are the conditions or parameters favoring one type of structure over the other? If sheet-like structures dominate in some circumstances, what are the statistics of the density gradient? Can they be sufficiently non-Gaussian to be compatible with pulsar scintillation scaling? It is desirable to consider such questions prior to calculation of rf wave scattering properties in the density gradient fields obtained from numerical solutions.

In chapter 5, we show that both current filaments and current sheet structures naturally arise in numerical solutions of a decaying KAW turbulence model. Each has a structure of the same type and at the same location in the electron density gradient. These structures become prevalent as the numerical solutions progress in time, and each is associated with highly non-Gaussian PDFs. Moreover, we show that small-scale current filaments and current sheets, along with their associated density structures, are highly sensitive to the magnitude of resistive damping and diffusive damping of density fluctuations.

Current filaments persist provided that resistivity η is small; similarly, electron density fluctuations and gradients are diminished by large diffusive damping in the electron continuity equation. The latter results from collisions assuming density fluctuations are subject to a Fick's law for diffusion. The magnitude of the resistivity affects (1) whether current filaments can become large in amplitude, (2) their spatial scale, and (3) the preponderance of these filaments as compared to sheets. The magnitude of the diffusive damping parameter, μ, similarly influences the amplitude of density gradients and, to a lesser degree, influences the extent to which electron density structures are non-localized.

In the ISM, resistive and diffusive damping become important near resistive scales. However, it is well known that collisionless damping effects are also present (Lysak and Lotko, 1996; Bale et al., 2005), and quite possibly play a significant role at scales near the ion Larmor radius. The collisional damping in the present work should be understood as a best attempt to model damping using a fluid model. This approach facilitates analysis of the effects of different damping regimes on the statistics of electron density fluctuations. By varying the ratio of resistive and diffusive damping we can, as suggested above, control the type of structure present in the turbulence. This allows us to isolate and study the statistics associated with each type of structure. It also allows us to assess and examine the type of environment conducive to formation of the structure. We consider regimes with large and small damping parameters, enabling us to explore damping effects on structure formation across a range from inertial to dissipative.

In chapter 5 we present the results of numerical solutions of decaying KAW turbulence to ascertain the effect of different damping regimes on the statistics of the fields of interest, in particular the electron density and electron density gradient. In the $\eta \ll \mu$ regime (using normalized parameters), previous work

(Craddock et al., 1991) had large-amplitude current filaments that were strongly localized with no discernible electron density structures. (The collisional damping parameter μ was large to preserve numerical stability.) This regime is unable to preserve density structures or density gradients. The numerical solutions presented here have $\eta \sim \mu$ and $\eta \gg \mu$; in each limit the damping parameters are minimized so as to allow structure formation to occur, and are large enough to ensure numerical stability for the duration of each numerical solution. We investigate the statistics of both filaments and sheets in the context of scintillation in the warm ionized medium.

First we develop in chapter 2 a fluid model of kinetic Alfvén waves and a nonlinear model of decaying kinetic Alfvén wave turbulence, and give reasons for studying kinetic Alfvén waves in the context of small-scale intermittent density fluctuations. Applying two-timescale analysis, we derive conditions under which circularly symmetric intermittent structures can persist while interacting with turbulence, and we derive the PDFs associated with these intermittent structures.

2 COHERENT STRUCTURES IN FLUID MODELS OF KINETIC ALFVÉN WAVE TURBULENCE

The kinetic Alfvén wave (KAW) (Stéfant, 1970; Goertz, 1984; Lysak and Lotko, 1996; Hollweg, 1999) is the manifestation of the shear Alfvén wave at scales near the ion gyroradius when the wave has a large perpendicular wavenumber, $k_\perp \gg k_\parallel$ with $\perp$ and $\parallel$ indicating directions perpendicular and parallel to the mean magnetic field, respectively. Finite gyroradius effects account for the deviations of KAW physics from shear Alfvén wave physics. These effects play an important role only when KAW wavelengths are on the order of ρ_i, so KAWs have large $k_\perp$ wavenumbers transverse to the local magnetic field direction. The governing relation is $\rho_s k_\perp \sim 1$ where the ion sound gyroradius $\rho_s^2 = (T_e/m_i)/\omega_{ci}^2 = C_s^2/\omega_{ci}^2$. Here T_e is the electron temperature, m_i is the ion mass, $\omega_{ci} = eB/m_i c$ is the ion gyrofrequency, e is the magnitude of the electron/ion charge, B the magnitude of the mean magnetic field, and C_s is the sound speed. When $\rho_s k_\perp \sim 1$, kinetic Alfvén wave modifications to shear Alfvén wave physics begin to take effect and become more prominent for larger $\rho_s k_\perp$. While shear Alfvén waves are linearly incompressible, kinetic Alfvén waves allow for coupling between density fluctuations and magnetic fluctuations, and are linearly compressible. This compressibility is one means by which electron density fluctuations are generated at small scales.

Despite the name, *kinetic* Alfvén waves are often modeled with reduced *fluid* equations rather than the Vlasov-Maxwell equations. Throughout this work, we use fluid models to describe the KAW mode. Our reasons for doing so are these:

1. As will be demonstrated in this chapter, the nonlinear three-field and two-field fluid models have the same dispersion relation as the KAW, and

capture the same physics as in the conventional two-fluid description of the KAW mode.

2. Fernandez and Terry (1997) argue that the KAW mode becomes dynamically active at scales as large as $L \lesssim 10\rho_s$. Density fluctuations can no longer be considered passive at this scale, and the KAW nonlinear interactions detailed below begin to dominate in the energy interchange with the magnetic energy. This scale lies in a regime where Landau damping is not active, at length scales somewhat above the scales at which energy dissipation rates significantly dominate the small-scale dynamics.

3. The $L \lesssim 10\rho_s$ scale regime is sufficiently large to mitigate concerns that collisionless damping at small scales will destroy the nonlinear structures that spontaneously emerge.

4. The KAW fluid equations are amenable to both full closure theory calculations (Terry and Smith, 2007) and numerical simulation with moderate spatial and temporal resolution (Terry and Smith, 2008; Smith and Terry, 2011). The emergent features of the equations would be challenging to observe and analyze in a more detailed kinetic simulation, as these features exist on length scales $L \approx \rho_s$, which lies at the outer length scale of kinetic simulations.

5. Investigation of the statistical properties of the emergent features of KAW turbulence requires many simulation runs, which again favors model equations that can be numerically solved in a reasonable time frame, with reasonable storage requirements. Modeling the same scales in time and space with a kinetic simulation requires significant increases in simulation time and storage.

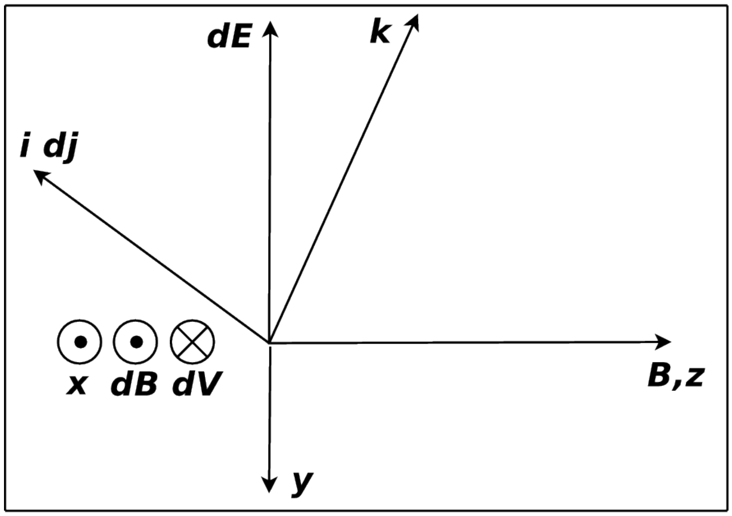

Figure 2.1: Polarization vectors for the shear Alfvén wave with a large $|k_y|$ component.

Before presenting the nonlinear KAW model, it is instructive to derive the linear KAW dispersion relation to see how the KAW differs from the shear Alfvén wave.

2.1 Kinetic Alfvén Wave Dispersion Relation

As a starting point[1], consider a shear Alfvén wave with a large $k_\perp = k_y$ component. The polarization vectors for fields of interest are represented in Fig. (2.1), with $\hat{z}$ the direction of the mean magnetic field; the $\hat{y} - \hat{z}$ plane lies in the plane of the page, and $\hat{x}$ is out of the page. The fluctuating component of the electric field of the shear Alfvén wave, dE, is in the $-\hat{y}$ direction, and dB and dV, the components of the magnetic and velocity fields, are in the $+\hat{x}$ and $-\hat{x}$ directions, resp.

The $\hat{x}$ component of Faraday's Law yields

[1]Here we summarize the derivation of the KAW dispersion relation given in Hollweg (1999).

$$\left(\delta E_y - \frac{k_y}{k_z}\delta E_z\right) = -\frac{\omega \delta B_x}{c k_z}. \tag{2.1}$$

In Eqn. (2.1) we do not exclude the possibility for a finite (but small) δE_z, and will justify its inclusion *a posteriori*. The shear Alfvén wave has $\delta E_z = 0$.

Accounting for nonzero compressive effects in the $\hat{y}$ direction is achieved by substituting

$$\delta E_y \rightarrow \delta E_y - \frac{(\nabla \delta p_i)_y}{q_i n_{0i}}. \tag{2.2}$$

With this substitution, the ion polarization drift in the $\hat{y}$ direction for the shear Alfvén wave becomes[2]

$$\delta V_{yi} = -\frac{q_i}{m_i}\frac{i\omega}{\omega_{ci}^2}\left(\delta E_y - \frac{i k_y \delta p_i}{q_i n_{0i}}\right). \tag{2.3}$$

Assuming the bulk ion motion is dominated by the polarization drift and $\delta V_{yi} \gg \delta V_{zi}$, then the ion continuity equation yields $\delta n_i / n_{0i} = k_y \delta V_{yi}/\omega$. Using this in Eqn. (2.3), we have

$$\delta V_{yi}\left(1 + \rho_s^2 k_y^2\right) = -\frac{q_i}{m_i}\frac{i\omega}{\omega_{ci}}\delta E_y \tag{2.4}$$

where we observe the finite gyroradius correction term—proportional to ρ_s^2—enter the equations.

The relation for the $\hat{z}$ component of the linearized electron momentum equation is $m_e \omega \delta V_{ze} = -ie\delta E_z + k_z \delta p_e / n_{0e}$. From this we can derive a relation between δE_z and δE_y, assuming quasi-neutrality and that electron motion is primarily along the mean magnetic field:

[2]Eqn. (20) in Hollweg (1999).

$$\frac{\delta E_z}{\delta E_y} = \frac{\frac{q_i}{e}\left(\frac{m_e}{m_i}\frac{\omega^2}{k_z^2} - \frac{\gamma_e T_{0e}}{m_i}\right)}{\omega_{ci}^2(1+\rho_s^2 k_y^2)}. \tag{2.5}$$

We can substitute Eqn. (2.5) into Eqn. (2.1) to remove δE_z. Employing the $\hat{y}$ component of Ampere's Law to yield a relation between δV_{yi} and δB_x,

$$n_{0i} q_i \delta V_{yi} = \delta j_y = \frac{ick_z}{4\pi}\delta B_x, \tag{2.6}$$

we can express δB_x in Eqn. (2.1) in terms of δV_{yi}, and using Eqn. (2.4), we can express all quantities in terms of δE_y. The resulting dispersion relation for the kinetic Alfvén wave is[3]

$$\frac{\omega^2}{k_z^2 V_A^2} = \frac{1+\rho_s^2 k_y^2}{1+k_y^2 d_e^2}, \tag{2.7}$$

where $V_A^2 = B^2/(4\pi n_{0i} m_i)$ is the squared Alfvén speed and $d_e^2 = c^2/\omega_{pe}^2 = c^2 m_e/(4\pi n_e e^2)$ is the squared electron skin depth.

In Eqn. (2.7), the right-hand-side contains small-scale corrections from finite Larmor radius and finite skin-depth effects resulting from electron inertial effects. In the limit $\rho_s \to 0$, $d_e = c/\omega_{pe} \to 0$, Eqn. (2.7) reduces to the shear Alfvén wave dispersion relation.

The KAW dispersion relation deals with the linear physics of kinetic Alfvén waves and its derivation reveals how KAWs yield density fluctuations at scales near ρ_s and smaller. Being "descendants" of the shear Alfvén wave, KAWs propagate along the local magnetic field, and are guided by it. This is evident from the expression for the group velocity

$$\mathbf{v}_g(\mathbf{k}) = \frac{\partial \omega}{\partial \mathbf{k}} \approx V_A \frac{4\rho_s^2 k_y^2}{\sqrt{1+\rho_s^2 k_y^2}}\left[\hat{z}\ \left(1+\frac{1}{\rho_s^2 k_y^2}\right) + \hat{y}\ \frac{k_z}{k_y}\right] + \mathcal{O}\left(\frac{d_e^2}{\rho_s^2}\right). \tag{2.8}$$

[3]Eqn. (25) in Hollweg (1999).

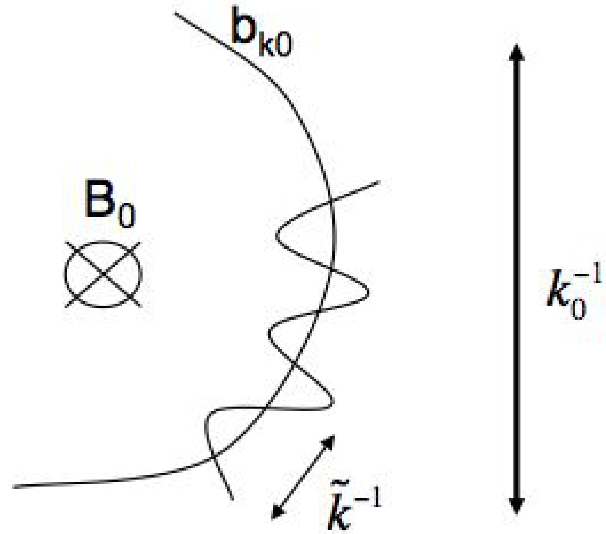

Figure 2.2: Illustration of a small-scale KAW, wavelength $\tilde{k}^{-1}$ propagating along a magnetic field line $\mathbf{b}_{k0}$ with length of variation k_0^{-1}. There is scale separation, such that $k_0 \ll \tilde{k}$.

For KAWs, $k_z/k_y \ll 1$, so to order $\mathcal{O}(k_z/k_y)$ the KAW group velocity propagates along the mean magnetic field. It is seen from the expression for $\mathbf{v}_g$ and the dispersion relation that KAWs are dispersive waves.

In Eqn. (2.8), the small parameter $d_e^2/\rho_s^2 = (m_e/m_i)(2/\beta)$, constraining $\beta \gg m_e/m_i$ from below for the KAW to propagate.

Packets of interacting KAWs propagating along a mean magnetic field are a small-scale manifestation of nonlinear interaction of wave packets in models of large-scale MHD shear Alfvén wave turbulence.[4]

To better illustrate this point, sketched in figure 2.2 is a small-scale KAW wavepacket with wavelength $\tilde{k}^{-1}$ propagating along the "secondary" magnetic field line $\mathbf{b}_{k0}$ with variation scale k_0^{-1}. The wavepacket and field line

[4]KAWs are not the only mode excited at small scales in a turbulent cascade; whistler turbulence is also expected at small scales (Saito et al., 2010). Which mode dominates in the dissipation range of interstellar turbulence is an active area of research, but is not a question we will address in the present work.

vary on different scales such that $k_0 \ll \tilde{k}$. The wavepacket is guided by the magnetic field according to the expression for the group velocity, Eqn. (2.8). The background magnetic field $\mathbf{B}_0$ is directed into the page, along which shear Alfvén waves propagate linearly. The secondary magnetic field $\mathbf{b}_{k0}$ lies in the plane of the page and could be generated by the current filament of a coherent structure, or may be the magnetic field associated with a larger-scale KAW. The small-scale wavepacket propagates along the secondary $\mathbf{b}_{k0}$ field, and it is this nonlinear interaction of waves with the fields of larger-scale KAWs and coherent structures that we wish to capture in the models developed below.

2.2 Nonlinear Fluid Model of Kinetic Alfvén Wave Turbulence

In this section, we propose two systems of nonlinearly coupled scalar fields that capture the essential physics of KAWs at varying outer length scales. In particular, the KAW property of active density fluctuations is a central element of the mode that the simplified scalar models aim to capture. The first model, the three-field model, couples electron density n, the $\hat{z}$ component of the vector potential, ψ, and the electrostatic potential, ϕ (Hazeltine, 1983; Rahman and Weiland, 1983; Fernandez et al., 1995; Fernandez and Terry, 1997). The second model is a small-scale simplification of the three-field model, and is valid for length scales $L < 10\rho_s$. The two-field model decouples the vorticity evolution $\nabla_\perp^2 \phi$ from the ψ and n evolution, leaving only magnetic-internal energy exchange (Craddock et al., 1991; Terry et al., 1998; Terry and Smith, 2007, 2008).

Fluid models of KAWs are unable to capture dissipation physics contained in kinetic descriptions such as Landau damping, transit-time damping, or cyclotron resonances (Hollweg, 1999). The advantage of fluid models is their relative simplicity that allows analytic tractability and exploration of length regimes near the transition region from shear Alfvén waves to kinetic Alfvén waves. These length regimes are challenging to resolve with present kinetic simulation methods, as they are orders of magnitude larger than kinetic length scales of interest.

Three-Field Model

The normalized three-field equations for KAWs are [5]

$$\partial_t \psi + \nabla_{\|} \phi = \alpha \nabla_{\|} n + \eta_0 J - \eta_2 \nabla_{\perp}^2 J, \tag{2.9}$$

$$\partial_t \nabla_{\perp}^2 \phi - \nabla \phi \times \hat{z} \cdot \nabla \nabla_{\perp}^2 \phi = -\nabla_{\|} J, \tag{2.10}$$

$$\partial_t n - \nabla \phi \times \hat{z} \cdot \nabla n + \nabla_{\|} J = \mu_0 \nabla_{\perp}^2 n - \mu_2 \nabla_{\perp}^2 \nabla_{\perp}^2 n, \tag{2.11}$$

where

$$\nabla_{\|} = \partial_z + \nabla \psi \times \hat{z} \cdot \nabla, \tag{2.12}$$

and

$$J = \nabla_{\perp}^2 \psi = \partial_{xx} \psi + \partial_{yy} \psi. \tag{2.13}$$

The perturbed magnetic field is perpendicular to the mean field and can be written as $\mathbf{b}/B = \nabla\psi \times \hat{z}$, where $\hat{z}$ is the direction of the mean field and $\psi = (C_s/c)eA_z/T_e$ is the normalized parallel component of the vector potential. The flow has zero mean and is also perpendicular to the mean field B. It is

[5] Notation: In Eqns. (2.9) - (2.13) "∂_t" is equivalent to the more explicit "$\frac{\partial}{\partial t}$"; multiple subscripts indicate higher order partial derivatives with respect to the subscript.

equivalent to the $\mathbf{E} \times \mathbf{B}$ flow and can be expressed in terms of the electrostatic potential as $-\nabla\phi \times \hat{z}$, where $\phi = (C_s/V_A)e\phi/T_e$ is the normalized electrostatic potential. The normalized density fluctuation is $n = (C_s/V_A)n/n_0$, where n_0 is the mean density, and $\alpha = (\rho_s/L)^2$ is a coupling parameter that determines the relative influence of the $\nabla_\parallel n$ term over the $\nabla_\parallel \phi$ term in Eqn. (2.9). The quantity L is the largest length scale of interest, thus $\alpha \ll 1$ corresponds to a large-scale, MHD regime and $\alpha \gg 1$ corresponds to a small-scale regime. In this system, $\eta_0 = (c^2/4\pi V_A \rho_s)\eta_{Spitzer}$ is the normalized resistivity, where $\eta_{Spitzer}$ is the Spitzer resistivity. The diffusive damping coefficient $\mu_0 = \rho_e^2 \nu_e/(\rho_s V_A)$ captures Fickian collisional diffusion where ρ_e is the electron gyroradius and ν_e is the electron collision frequency. The quantities η_2 and μ_2 are the hyperresistivity and hyperdiffusivity, and are numerical conveniences to preserve fluctuation amplitudes at medium and large scales. Spatial scales are normalized to ρ_s (defined above), time is normalized to the Alfvén time $\tau_A = \rho_s/V_A$, and $V_A = B/(4\pi m_i n_0)^{1/2}$ is the Alfvén velocity.

In Eqn. (2.11), the density continuity equation, the term $\nabla_\parallel J$ is a compressible nonlinearity that allows compressible electron motion along magnetic field perturbations to couple to the density field. The $\nabla_\parallel n$ term in Ohm's law allows electron pressure fluctuations to act on the magnetic field in Eqn. (2.9). At scales larger than the ion gyroradius, i.e. for $\alpha \ll 1$, the magnetic-density coupling is weak and density fluctuations are passive to a good approximation. At scales approaching $L \lesssim 10\rho_s$ and smaller, corresponding to $\alpha \gtrsim 10^{-2}$, $\nabla_\parallel n$ begins to dominate $\nabla_\parallel \phi$ in Eqn. (2.9) and $\nabla_\parallel J$ begins to dominate $\nabla\phi \times \hat{z} \cdot \nabla n$ in Eqn. (2.11) (Fernandez and Terry, 1997). In this length regime, the system behaves very differently from incompressible MHD where the only energy interchange is between the magnetic and velocity fields via shear Alfvén waves. In a turbulent cascade, the magnetic-velocity energy exchange is diminished relative to the magnetic-density exchange, and flow decouples from the magnetic field, evolving as a go-it-alone Kolmogorov cascade. As α increases, the electron density and magnetic fields increasingly interact compressively via kinetic Alfvén waves; once this interaction reaches prominence, the internal and magnetic energies become equipartitioned, $\int n^2 \, dV \approx \int |\nabla\psi|^2 \, dV$. This equipartition at small scales takes place even if internal energy is a fraction of the magnetic energy at large scales.

Four ideal invariants exist: total energy $E = \int d^2x(|\nabla\psi|^2 + |\nabla\phi|^2 + \alpha n^2)$; flux $F = \int d^2x \;\; \psi^2$; cross-correlation $H_c = \int d^2x \;\; n\psi$; and enstrophy $G = \int d^2x(n - \nabla_\perp^2 \phi)^2$. Energy cascades to small scale (large wavenumber) while the flux and cross-correlation undergo an inverse cascade to large scale (small wavenumber) (Fernandez and Terry, 1997). The inverse cascades require the initialized spectrum in numerical solutions to peak at $k_0 \neq 0$ to allow for buildup of magnetic flux at large-scales for later times.

Linearizing the system and introducing dimensional quantities yields a dispersion relation

$$\frac{\omega^2}{V_A^2(\mathbf{b}_0 \cdot \mathbf{k})^2} = 1 + \rho_s^2 k_\perp^2. \tag{2.14}$$

To $\mathcal{O}(d_e^2/\rho_s^2)$, this is equivalent to the more accurate dispersion relation given in Eqn. (2.7). The mode combines perpendicular oscillation associated with a finite gyroradius with fluctuations along a mean field ($\hat{z}$-direction). For $\rho_s^2 k_\perp^2 \ll 1$ the dispersion relation reduces to that of the shear Alfvén wave, and the term proportional to ρ_s^2 is the finite gyroradius correction term. For $\rho_s^2 k_\perp^2 \gtrsim 1$, the waves are increasingly dispersive, which has implications for timestepping constraints in explicit numerical solution schemes.

Two-Field Model

For small-scales, when $\alpha \gtrsim 1$, the model can be simplified by decoupling the flow evolution. The remaining equations couple electron density fluctuations with magnetic fluctuations, and the ions form a neutralizing background. The two-field system is

$$\partial_t \psi = \alpha \nabla_{\|} n + \eta_0 J - \eta_2 \nabla_{\perp}^2 J, \tag{2.15}$$

$$\partial_t n - \nabla_{\|} J = \mu_0 \nabla_{\perp}^2 n - \mu_2 \nabla_{\perp}^2 \nabla_{\perp}^2 n. \tag{2.16}$$

This model assumes isothermal fluctuations. The dispersion relation for Eqns. (2.15)-(2.16) is further simplified: $\omega^2/\{V_A^2(\mathbf{b}_0 \cdot \mathbf{k})^2\} = \rho_s^2 k_{\perp}^2$. This two-field model removes all shear Alfvén wave effects, evident by the absence of the constant term on the RHS.

In the limit of strong mean field, quantities along the mean field ($\hat{z}$-direction) equilibrate quickly, which allows $\partial/\partial z \to 0$, or $k_z \to 0$. Kinetic Alfvén waves still propagate, as long as there is a broad range of scales that are excited, as in fully developed turbulence. As $k_z \to 0$, all gradients are localized to the plane perpendicular to the mean field. Presuming a large-scale fluctuation at characteristic wavenumber $\mathbf{k}_0$, smaller-scale fluctuations propagate linearly along this larger-scale fluctuation so long as their characteristic scale k satisfies $k \gg k_0$.

2.3 Two-timescale Analysis

The nonlinear interaction of KAWs in a fully turbulent system can give rise to interesting and non-obvious structures that evolve on a much longer timescale than the turbulence (Craddock et al., 1991). A simple calculation serves to demonstrate that the system of Eqns. (2.9)–(2.11) can give rise to persistent structures with near circular symmetry in two dimensions.

In polar coordinates, if the fields $n(r,\theta)$ and $\psi(r,\theta)$ have no θ dependence, then the parallel gradient term, $\nabla_\parallel$, simplifies to $\nabla_\parallel = (-\hat{\theta}\cdot\hat{r})\partial_r\psi\partial_r = 0$. Since $\hat{\theta}\perp\hat{r}$, the $\alpha\nabla_\parallel n$ and $\nabla_\parallel J$ are identically zero. The same holds for the $\nabla\phi\times\hat{z}\cdot\nabla$ advective nonlinearity. In this radially symmetric system the only nonzero terms are the linear diffusive terms, and the circularly symmetric structures are affected by linear damping only. If a structure has a large characteristic length scale relative to the linear damping scales, it can persist for a long time relative to small-scale turbulence.

A similar argument in Cartesian coordinates for structures with one ignorable dimension, such that $\partial_y\psi(x,y) = 0$, reveals that elongated, sheet-like structures have no nonlinear interaction either. These trivial derivations yield little physical insight as to how structures persist when interacting with turbulence at their boundary, but they indicate that one can expect long-lived structures in KAW turbulence to take the form of localized, circularly symmetric filaments or elongated sheets. Both of these formations have one ignorable coordinate in their local frame.

To better understand the means by which a (circular) structure persists when interacting with turbulent fluctuations, outside the region where the structure has no θ dependence, we summarize the two-timescale analysis in Terry (1989, 2000); Terry and Smith (2007). We focus on the dimensional analysis part of the discussion and do not cover the full closure theory. We refer the reader to Terry (1989) and Terry (2000) for an application of two-timescale analysis to Navier-Stokes turbulence, and Terry and Smith (2007) for a fuller treatment, including the eddy-damped quasi-normal Markovian closure calculations for Eqns. (2.15)-(2.16).

Assume a circular current structure, azimuthally symmetric with an associated polar coordinate system. We presume that the current in this structure is localized such that for all $r > R$, $J_0(r) = 0$ for some radial distance R. The current filament has an associated $\hat{\theta}$-directed magnetic field, $B_\theta(r)$. Using symmetry and Ampere's Law, it is elementary to show that, for $r > R$, $B_\theta(r) \propto r^{-1}$. This structure interacts with turbulence at its boundary, and the structure is assumed to evolve on a long timescale τ, while the turbulence evolves on a short timescale t. The n and ψ fields of equations (2.15)-(2.16) can be decomposed into long- and short-timescale parts,

$$\hat{F} = F_0(r, \tau) + \tilde{F}(r, \theta, t), \tag{2.17}$$

where F is either n or ψ, with F_0 the magnetic flux and density of the structure and $\tilde{\psi}$ and $\tilde{n}$ the turbulent fields of flux and density.

An evolution equation for the turbulent fields can be derived from Eqns. (2.15)-(2.16) by means of the two-timescale analysis[6]. With circular symmetry, it is appropriate to introduce a Fourier transform in the θ coordinate. The turbulence evolves from some initial state, so we can transform the time coordinate using a Laplace transform. The fields (2.17) can be expressed as

$$\tilde{F}(r, \theta, t) = \frac{1}{2\pi i} \int_{-i\infty+\gamma_0}^{+i\infty+\gamma_0} d\gamma \sum_m \tilde{F}_{m\gamma}(r) \exp(-im\theta) \exp \gamma t. \tag{2.18}$$

We find that the evolution equations for the fast-timescale turbulent fluctuations are

[6]Equations for the evolution of the structures can be derived as well, but are not presented here. See Terry and Smith (2007), Section 3.

$$\begin{aligned}
\gamma\tilde{\psi}_{m\gamma} + im\frac{B_\theta(r)}{r}\tilde{n}_{m\gamma} + \frac{1}{2\pi i}\int_{-i\infty+\gamma_0}^{+i\infty+\gamma_0} d\gamma' \times \\
\sum_{m'}\left[\frac{im'}{r}\tilde{\psi}_{m'\gamma'}\partial_r - \frac{i(m-m')}{r}\partial_r\tilde{\psi}_{m'\gamma'}\right]\tilde{n}_{m-m',\gamma-\gamma'} \\
= \frac{im}{r}\tilde{\psi}_{m,\gamma}\partial_r n_0(r),
\end{aligned} \tag{2.19}$$

$$\begin{aligned}
\gamma\tilde{n}_{m\gamma} + im\frac{B_\theta(r)}{r}\nabla_m^2\tilde{\psi}_{m\gamma} - \frac{1}{2\pi i}\int_{-i\infty+\gamma_0}^{+i\infty+\gamma_0} d\gamma' \times \\
\sum_{m'}\left[\frac{im'}{r}\tilde{\psi}_{m'\gamma'}\partial_r - \frac{i(m-m')}{r}\partial_r\tilde{\psi}_{m'\gamma'}\right]\nabla_{m-m'}^2\tilde{\psi}_{m-m',\gamma-\gamma'} \\
= \frac{im}{r}\tilde{\psi}_{m,\gamma}\partial_r J_0(r),
\end{aligned} \tag{2.20}$$

where

$$\nabla_m^2 = \frac{1}{r}\partial_r\left(r\partial_r\right) - \frac{m^2}{r^2}$$

is the Laplacian. (The dissipative terms are not shown, motivated by our focus on inertial scales.) Three terms drive the evolution of $\partial_t\hat{\psi}$ and $\partial_t\hat{n}$ in Eqns. (2.19)-(2.20). The first term describes linear KAW propagation along the inhomogeneous secondary magnetic field B_θ of the coherent structure. The nonlinearity—the second term—describes turbulence of random KAWs. The third term is a source term proportional to mean field gradients.

Magnetic shear in the second terms of Eqns. (2.19)-(2.20), implicit in the above expressions, plays a central role in structure-turbulence interaction. It can be made explicit by expanding the shear term in a Taylor series about some radius $r_0 > 0$,

$$\frac{B_\theta(r)}{r} = \frac{B_\theta(r_0)}{r_0} + (r - r_0)\,\frac{d}{dr}\frac{B_\theta}{r}\Big|_{r_0} + \cdots . \tag{2.21}$$

Eqn. (2.21) can be truncated as indicated if $B_\theta(r)$ varies smoothly, as is the case when the current profile is monotonically decreasing. When substituting Eqn. (2.21) into Eqns. (2.19)-(2.20), the $\frac{B_\theta(r_0)}{r_0}$ term Doppler shifts the frequency by a constant amount. The remaining term in the expansion describes KAW propagation in an inhomogeneous medium.

Substituting Eqn. (2.21) into Eqn. (2.20) yields

$$\begin{aligned}\hat{\gamma}\tilde{n}_{m\gamma} - im\,(r-r_0)\,\frac{d}{dr}\frac{B_\theta(r)}{r}\Big|_{r_0}\nabla^2_m\tilde{\psi}_{m\gamma} - \frac{1}{2\pi i}\int_{-i\infty+\gamma_0}^{+i\infty+\gamma_0} d\gamma'\times \\ \sum_{m'}\left[\frac{im'}{r}\tilde{\psi}_{m'\gamma'}\partial_r - \frac{i(m-m')}{r}\partial_r\tilde{\psi}_{m'\gamma'}\right]\nabla^2_{m-m'}\tilde{\psi}_{m-m',\gamma-\gamma'} \\ = \frac{im}{r}\tilde{\psi}_{m,\gamma}\partial_r J_0(r)\end{aligned} \tag{2.22}$$

where

$$\hat{\gamma} = \gamma + im\frac{B_\theta(r_0)}{r_0}. \tag{2.23}$$

We focus on the $\mathcal{S}_{B_\theta} \equiv d/dr[B_\theta/r]|_{r_0}$ term. When it is large, the shear in B_θ refracts KAW activity, as can be argued using asymptotic analysis. The refraction of KAW phase fronts is visualized in Fig. 2.3, where in the core of the structure, with $B_\theta \propto r$, the phase fronts propagate in the $\hat{\theta}$ direction undistorted. In the core, $\mathcal{S}_{B_\theta}$ is zero. As nonzero radial shear develops for greater r, the phase fronts of KAWs are distorted by the nonzero $\mathcal{S}_{B_\theta}$. In the limit that $\mathcal{S}_{B_\theta}$ becomes large asymptotically, the solution develops a small-scale boundary layer structure to allow the higher derivative nonlinear term to remain in balance with $\mathcal{S}_{B_\theta}$ term. The boundary layer's width is constrained to become narrower as $\mathcal{S}_{B_\theta}$ becomes larger; otherwise the highest order derivative drops out of the balance and the equation changes order (Bender and Orszag, 1978). Dimensional analysis gives an estimate of the boundary width Δr. Noting

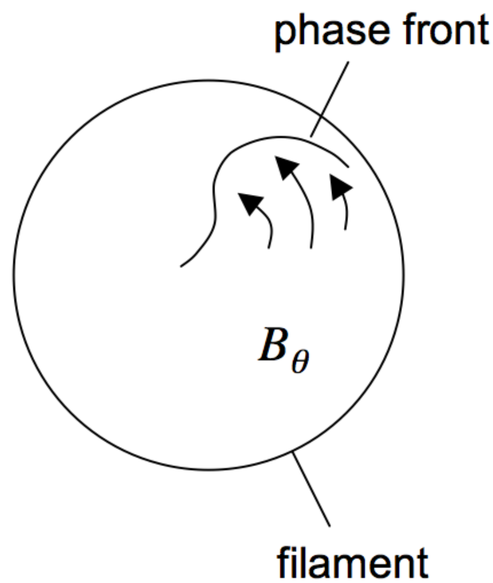

Figure 2.3: Illustration of propagating KAW phase fronts in an azimuthally-symmetric filamentary structure. Near $r = 0$ the phase fronts form radial spokes; as radial shear in the B_θ field of the structure develops for greater r, the phase fronts are distorted.

that $r - r_0 \sim \Delta r$, $\partial_r \tilde{n}_m(t) \sim \tilde{n}_m/\Delta r$, and treating $d/dr[B_\theta/r]|_{r_0} \equiv j'$ as the diverging asymptotic parameter, the balance is

$$\Delta r j' \tilde{n}_m(t) \sim \frac{\tilde{\psi}_m(t)}{a}\frac{\tilde{n}_m(t)}{\Delta r} \qquad (j' \to \infty). \tag{2.24}$$

Simplifying,

$$\Delta r \sim \sqrt{\frac{\tilde{\psi}_m}{a j'}} \qquad (j' \to \infty). \tag{2.25}$$

The length Δr is the scale of fluctuation variation within the coherent structure, and represents a fluctuation penetration depth into the structure. An analogous derivation applies to the terms in Eqn. (2.19), and yield the same scaling. Hence

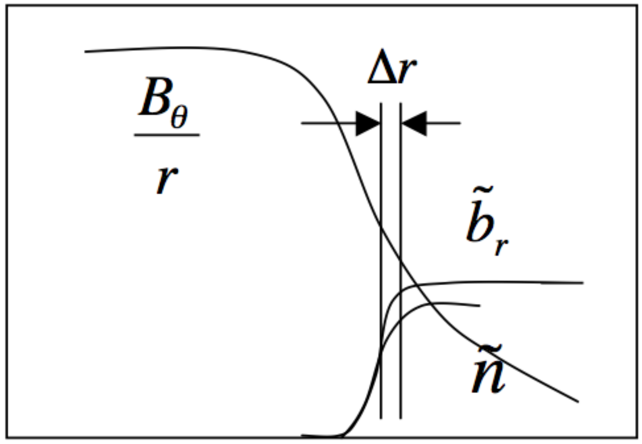

Figure 2.4: Illustration of the boundary layer in B_θ/r for a filamentary structure. The boundary layer has characteristic width Δr, and the turbulent fluctuations $\tilde{b}$ and $\tilde{n}$ cannot penetrate many Δr layer widths into the structure.

Δr is the width of a single layer with respect to refracted fluctuations in both density and current structures. The boundary layer is visualized in Fig. 2.4, with the structure B_θ/r constant in the core, and has a large radial derivative. The turbulent fluctuations are visualized to the right in the figure, and the turbulent amplitude is unable to sustain itself many Δr layer widths into the structure.

While this analysis yields a layer width, it does not give the functional variation of current and density fluctuations within the layer, either relative or absolute. The details of structure-turbulence interaction are investigated in numerical simulations, and will be addressed in the following chapters.

2.4 Global PDFs and Structure Geometry

Scintillation in the ISM depends on the statistics of the density difference, $\Delta n \equiv n(\mathbf{x}, z) - n(\mathbf{x} + \Delta\mathbf{x}, z)$ (Boldyrev and Gwinn, 2005) which is approximated by the density gradient, $\Delta n \approx \Delta\mathbf{x} \cdot \nabla_\perp n|_{\mathbf{x},z}$ for small $|\Delta x|$. The KAW system, by coupling fluctuations in the density and magnetic fields, is expected to yield similar amplitudes and structures in these fields. If the magnetic field around a structure with $J_0(r) = 0$ for $r \geq R$ yields a $1/r$ mantle due to Ampere's Law, then, arguing from turbulent equipartition between δn fluctuations and δB fluctuations via kinetic Alfvén wave interactions, the density field will have a mantle of a similar form, and extend to the same radius. We will show in this section that assuming $n(r) \propto 1/r$ in the mantle of a filamentary density structure is sufficient to yield non-Gaussian statistics for the density gradient field. This analysis neglects the influence on the PDF from fluctuations between structures, and considers only the immediate region around structures themselves. Accounting for fluctuations between structures poses considerable challenges, as this region is a mixture of turbulence and non-filamentary structures that are not easily characterized by a few parameters, such as maximum current amplitude, or structure radius.

Assuming $n(r) \propto 1/r$ in the structure mantle makes the density structure less localized than the associated current filament, and results in a greater likelihood of low values of density than those of decaying turbulence. This yields a density kurtosis closer to the Gaussian value of 3 than the current kurtosis. The density PDF will not likely be Gaussian, however.

Consider an idealized density structure, sketched in figure 2.5. It has a flat core that extends to radius $r = a$, and for $r > a$,

$$n(r) = an_0/r, \tag{2.26}$$

where n_0 is the value of the density at $r = a$. As indicated in figure 2.5, the area occupied by a given density value in the mantle region is $2\pi r\, \mathrm{d}r$. When normalized, this area is proportional to the probability of density value $n(r)$; thus

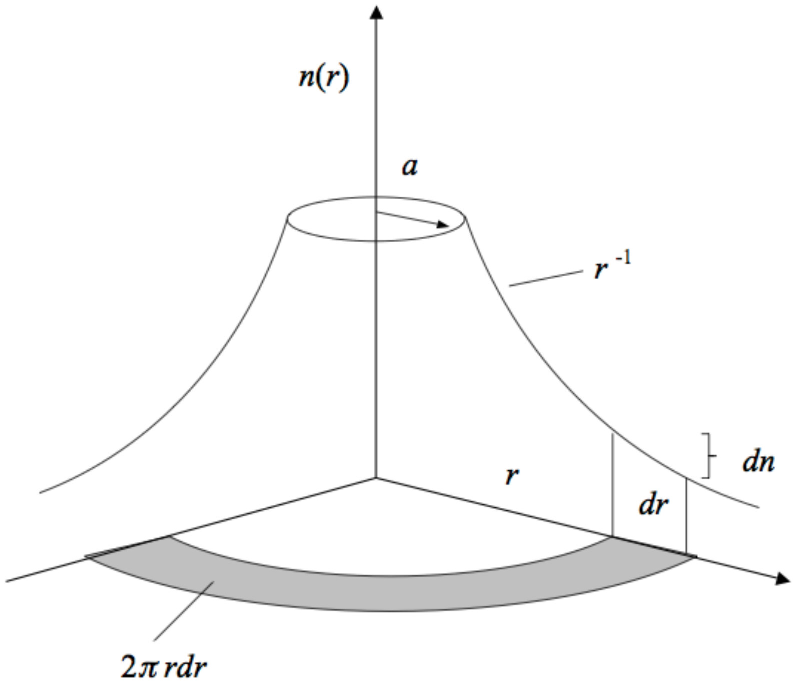

Figure 2.5: Schematic of an idealized density structure. The structure core extends to radius a, and its mantle for $r > a$ goes as $n(r) \propto r^{-1}$.

$$P(n)\ \mathrm{d}n = 2\pi r\ \mathrm{d}r. \tag{2.27}$$

Eqn. (2.26) can be used to remove rdr from Eqn. (2.27); doing so yields

$$P(n)\ \mathrm{d}n = \frac{C_n}{n^3}\ \mathrm{d}n \tag{2.28}$$

where C_n is a normalization constant chosen such that the probability integrated over the whole filament is equal to filament packing fraction, which is the probability of finding the filament in a given area.

The PDF for density gradients is found following the same procedure as above, and noting that $\nabla n \equiv n' \sim r^{-2}$. Expressing rdr in terms of $n'\ \mathrm{d}n'$ using

$r \sim (n')^{-1/2}$, we have

$$P(n')\ \mathrm{d}n' = \frac{C_{n'}}{(n')^2}\ \mathrm{d}n', \tag{2.29}$$

where $C_{n'}$ is another normalization constant. This is a Lévy distribution, the type of non-Gaussian distribution inferred from pulsar signal width scaling (Boldyrev and Gwinn, 2003b).

2.5 Initial averaging during structure formation

In the previous section, it was argued that a density profile $n(r) = an_0r^{-1}$ is a reasonable assumption from KAW dynamics and turbulent equipartition. A significant correction to this argument addresses the effect of density fluctuation averaging during the initial stages of filament formation.

In the initial stages of structure formation, when a circular structure is establishing its shear boundary layer, the region that eventually becomes a structure entrains density fluctuations of positive and negative sign. The entrained initial density fluctuations mix preferentially in the $\hat{\theta}$ direction—being the direction of KAW propagation within a structure core—which gives rise to radial density variations inside a structure's boundary. This averaging process results in the density of the structure having arbitrary sign and amplitude relative to the current. Correlation between the radius of the density structure and the radius of the $|B|$ structure is expected, as they both have $1/r$ mantles, beyond which the density field is no longer preserved from turbulence. For structures with radial extent on the order of the initial density correlation length, the density field in the structure has decreased radial variation, and will be nearly monotonic in the radial coordinate.

Upon formation, the density field inside the structure is preserved from mixing with turbulence by virtue of being inside the shear boundary layer, where turbulence cannot disturb it.

2.6 Discussion and Conclusions

In this chapter we derived the KAW dispersion relation, making note of the capacity of this mode to generate density fluctuations on small scales. A nonlinear scalar three-field fluid model was shown to capture the essential physics of the KAW mode. The model and its two-field simplification allow for nonlinear interaction of KAWs at varying scales, such that a KAW with small wavelength can propagate along the $\mathbf{B}$ field of a larger-scale KAW wave.

By considering non-trivial configurations in which the nonlinearities of Eqns. (2.9) - (2.11) are zero, it was a simple matter to demonstrate that long-lived structures can be expected to be circularly symmetric with arbitrary radial profiles, or elongated, sheet-like structures with one direction of symmetry; however, this yields no insight into how these structures persist in the midst of turbulent mixing at the structure boundary.

Dimensional analysis applied to a two-timescale formulation of Eqns. (2.15)-(2.16) revealed the importance of a shear boundary layer in $B_\theta(r)$ at the edge of a circular structure as the means by which a structure preserves itself when interacting with turbulence.

The statistical properties of a density structure with a $n(r) \propto 1/r$ mantle were shown to yield non-Gaussian statistics for the gradient of density. This result is significant for pulsar scintillation in the ISM which predicts non-Gaussian statistics in the density difference field.

More detailed aspects of structures will be investigated in the next chapters. Chapter 4 discusses in detail the means by which a structure clearly distinguishes itself from turbulence. It proposes the Hessian field of ψ as a way to measure the combined importance of a large current filament in the core of a structure that is surrounded by a shear boundary layer in $B_\theta(r)$. It will be shown that flux tubes that are delimited in isosurfaces of ψ are an appropriate way to robustly and algorithmically separate circular structures from turbulence.

In contrast to the *local* analysis of individual structures in chapter 4, the *global* statistical properties of the magnetic, current, density, and density gradient fields will be presented in chapter 5. That chapter will investigate the deviations from Gaussian statistics in the fields of interest, and investigate the effect of structures on the kurtosis.

The next chapter gives details of the numerical scheme used to evolve Eqns. (2.9) - (2.11) and describes the initialization of the ψ, ϕ, and n fields.

3 NUMERICAL SOLUTION METHOD AND INITIAL CONDITIONS

We present here an explicit pseudo-spectral method for numerically integrating a nonlinear PDE in the Fourier domain. We employ an explicit rather than implicit scheme to resolve physics at all timescales, as is often required in multi-scaled turbulence simulations. Before devising a numerical scheme for evolving a solution, we employ an integrating factor transformation (Canuto et al., 1990). To within numerical precision, this transformation makes possible the exact integration of the linear terms and removes their associated time stepping constraints (Courant et al., 1967). All stability constraints come from the numerical evolution of the nonlinear terms. We formulate the scheme in general and then apply it to model Eqns. (2.9) - (2.11) for completeness.

We begin with a generalized PDE in time t and space $\mathbf{x}$, with periodic boundary conditions. We collect the linear terms in a linear transform $\mathcal{L}$ and the quadratic nonlinearities are collected in $\mathcal{N}$:

$$\partial_t \mathbf{v}(\mathbf{x},t) = \mathcal{L}\mathbf{v}(\mathbf{x},t) + \mathcal{N}\left[\mathbf{v}(\mathbf{x},t)\right]. \tag{3.1}$$

We make the substitutions

$$\mathbf{v}(\mathbf{x},t) = \mathcal{F}^{-1}\left[\mathbf{v}_k(t)\right] \tag{3.2}$$

$$\mathcal{L}\mathbf{v}(\mathbf{x},t) = \mathcal{F}^{-1}\left[\mathcal{L}_k\mathbf{v}_k(t)\right] \tag{3.3}$$

and

$$\mathcal{N}\left[\mathbf{v}(\mathbf{x},t)\right] = \mathcal{F}^{-1}\left[\mathcal{N}_k\left[\mathbf{v}_k(t)\right]\right] \tag{3.4}$$

into Eqn. (3.1), where $\mathbf{y}(\mathbf{x},t) = \mathcal{F}^{-1}\left[\mathbf{y}_k(t)\right]$ is the inverse Fourier transform of $\mathbf{y}(\mathbf{x},t)$ with $\mathbf{y}(\mathbf{x},t) = \mathcal{F}^{-1}\left[\mathcal{F}\left[\mathbf{y}(\mathbf{x},t)\right]\right]$. The resulting nonlinearly coupled ODEs are

$$\frac{d}{dt}\mathbf{v}_k(t) = \mathcal{L}_k\mathbf{v}_k(t) + \mathcal{N}_k\left[\mathbf{v}_k(t)\right] \tag{3.5}$$

where we assume the $\mathcal{L}_k$ matrix is time-independent.

To employ an integrating factor that transforms Eqn. (3.5), we use the matrix exponential $\exp(t\mathcal{L}_k)$, noting the commutability relation $\exp(t\mathcal{L}_k)\mathcal{L}_k = \mathcal{L}_k\exp(t\mathcal{L}_k)$. To use the integrating factor, we note the equality

$$\frac{d}{dt}\left[\mathrm{e}^{-t\mathcal{L}_k}\mathbf{v}_k(t)\right] = \mathrm{e}^{-t\mathcal{L}_k}\left[\frac{d}{dt}\mathbf{v}_k(t) - \mathcal{L}_k\mathbf{v}_k(t)\right], \tag{3.6}$$

which allows us to introduce the integrating factor $\exp(-t\mathcal{L}_k)$ into Eqn. (3.5) and express it in the compact form

$$\frac{d}{dt}\left[\mathrm{e}^{-t\mathcal{L}_k}\mathbf{v}_k(t)\right] = \mathrm{e}^{-t\mathcal{L}_k}\mathcal{N}_k\left[\mathbf{v}_k(t)\right]. \tag{3.7}$$

The matrix exponential of $t\mathcal{L}_k$ is computationally feasible if the linear coefficient matrix $\mathcal{L}_k$ is diagonal (the case for Eqns. (2.9) - (2.13)) or easily diagonalizable.

Defining

$$\mathbf{u}_k(t) = \mathrm{e}^{-t\mathcal{L}_k}\mathbf{v}_k(t) \tag{3.8}$$

and

$$\mathbf{N}_k\left[t,\mathbf{u}_k(t)\right] = \mathrm{e}^{-t\mathcal{L}_k}\mathcal{N}_k\left[\mathbf{v}_k(t)\right] = \mathrm{e}^{-t\mathcal{L}_k}\mathcal{N}_k\left[\mathrm{e}^{t\mathcal{L}_k}\mathbf{u}_k(t)\right], \tag{3.9}$$

Eqn. (3.7) becomes

$$\frac{d}{dt}\mathbf{u}_k(t) = \mathbf{N}_k\left[t,\mathbf{u}_k(t)\right], \tag{3.10}$$

which is the canonical form appropriate for discretization by a numerical scheme.

For example, a simple two-stage second-order Runge-Kutta scheme to approximate $\mathbf{u}_k(t+\Delta t)$ given $\mathbf{u}_k(t)$ is

$$\begin{aligned}
\mathbf{u}_k^{(n+1/2)} &= \mathbf{u}_k^{(n)} + \frac{\Delta t}{2}\mathbf{N}_k\left[t^{(n)}, \mathbf{u}_k^{(n)}\right] \\
\mathbf{u}_k^{(n+1)} &= \mathbf{u}_k^{(n)} + \Delta t\mathbf{N}_k\left[t^{(n+1/2)}, \mathbf{u}_k^{(n+1/2)}\right],
\end{aligned} \tag{3.11}$$

where Δt is the time step. In Eqns. (3.11) we used the standard notation $x^{(n)}$ to indicate discrete time level n, so $t^{(n+1/2)} = t^{(n)} + \Delta t/2$ and $\mathbf{u}_k^{(n+1)}$ is the numerical approximation for $\mathbf{u}_k(t+\Delta t)$.

In terms of $\mathbf{v}_k(t) = \exp(t\mathcal{L}_k)\mathbf{u}_k(t)$, Eqns. (3.11) take the more explicit form

$$\begin{aligned}
\mathbf{v}_k^{(n+1/2)} &= \mathrm{e}^{\Delta t/2\mathcal{L}_k}\left[\mathbf{v}_k^{(n)} + \frac{\Delta t}{2}\mathcal{N}_k\left[\mathbf{v}_k^{(n)}\right]\right] \\
\mathbf{v}_k^{(n+1)} &= \mathrm{e}^{\Delta t\mathcal{L}_k}\mathbf{v}_k^{(n)} + \mathrm{e}^{\Delta t/2\mathcal{L}_k}\Delta t\mathcal{N}_k\left[\mathbf{v}_k^{(n+1/2)}\right].
\end{aligned} \tag{3.12}$$

To apply scheme (3.12) to model Eqns. (2.9) - (2.13), we make the substitutions

$$\mathbf{v}_k(t) = \begin{pmatrix} \psi_k(t) \\ k^2\phi_k(t) \\ n_k(t) \end{pmatrix}, \tag{3.13}$$

$$\mathcal{L}_k = -\begin{pmatrix} \eta_0 k^2 + \eta_2 k^4 & 0 & 0 \\ 0 & \nu_0 + \nu_2 k^2 & 0 \\ 0 & 0 & \mu_0 k^2 + \mu_2 k^4 \end{pmatrix}, \tag{3.14}$$

and

$$\mathcal{N}_k\left[\mathbf{v}_k(t)\right] = \begin{pmatrix} \mathcal{F}\left[\alpha\nabla_\parallel n - \nabla_\parallel \phi\right] \\ \mathcal{F}\left[\nabla_\parallel J - \nabla\phi \times \hat{z}\cdot\nabla\nabla_\perp^2\phi\right] \\ \mathcal{F}\left[\nabla\phi\times\hat{z}\cdot\nabla n - \nabla_\parallel J\right] \end{pmatrix}, \tag{3.15}$$

where ψ_k, $-k^2\phi_k$, and n_k are the spatial Fourier transform of ψ, $\nabla_\perp^2\phi$, and n. Here we do not expand the nonlinear transformed terms in convolutions over k because the numerical scheme will integrate these terms pseudospectrally.

The matrix exponential takes the simple form

$$\mathrm{e}^{t\mathcal{L}_k} = \begin{pmatrix} \mathrm{e}^{-(\eta_0 k^2+\eta_2 k^4)t} & 0 & 0 \\ 0 & \mathrm{e}^{-(\nu_0+\nu_2 k^2)t} & 0 \\ 0 & 0 & \mathrm{e}^{-(\mu_0 k^2+\mu_2 k^4)t} \end{pmatrix}. \tag{3.16}$$

We evolve Eqns. (2.9) - (2.13) according to a second-order scheme similar to scheme (3.12) or a fourth-order scheme with minimal storage requirements (Carpenter and Kennedy, 1994). The equations are modeled in a 2D periodic domain of size $2\pi L \times 2\pi L$ on a mesh with typical resolution of 512×512. The nonlinearities are advanced pseudospectrally and with full $2/3$ dealiasing in each dimension (Orszag, 1971).

The resolution is not large due to unfavorable scaling of dispersive KAWs. The dispersion relation Eqn. (2.7) indicates that the wave frequency of KAWs with large wavenumber scale as $\omega \propto k^2$. To double the dynamic range for 2D KAW turbulence requires a factor-of-four decrease in the time step to sufficiently resolve all Fourier modes in time, which becomes prohibitive for large resolutions.

3.1 Initial Conditions

The ψ_k, ϕ_k and n_k fields are initialized such that the energy spectra are broadband with a peak near $k_0 \sim 6 - 10$ and a power law spectrum for $k > k_0$. Spectral exponents of decaying turbulence are not of central concern for the present work. As long as the initial conditions excite a broad range of KAW modes such that they interact nonlinearly for many Alfvén times, the results are not sensitive to the particulars of the spectral exponent, but are sensitive to the values of the damping coefficients. The falloff in k is predicted to be k^{-2} for small-scale turbulence. Craddock et al. (1991) use k^{-3}, between the current-sheet limit of k^{-4} and the kinetic-Alfvén wave strong-turbulence limit of k^{-2}. The numerical solutions considered here have either k^{-2} or k^{-3}. The primary qualitative difference between the two spectra is the scale at which structures initially form. The k^{-2} spectrum has more energy at small scales, leading to small initial characteristic structure size relative to simulations with k^{-3}. After a few tens of Alfvén times these small-scale structures merge and the system resembles the initial k^{-3} spectra.

The mode amplitude for magnetic, internal, and kinetic spectra is set according to

$$E(k) \propto \frac{k}{k^{-s+1} + k_0^{-s+1}}, \tag{3.17}$$

where $s = -3$ or $s = -2$ is the spectral exponent. In figure 3.1 the initial energy spectrum for a representative simulation with resolution 512×512 is shown. The spectra approach $E(k) \propto k^{-3}$ for intermediate and large k.

In terms of the discretized transformed quantities ψ_k, n_k, and ϕ_k, the spectra are

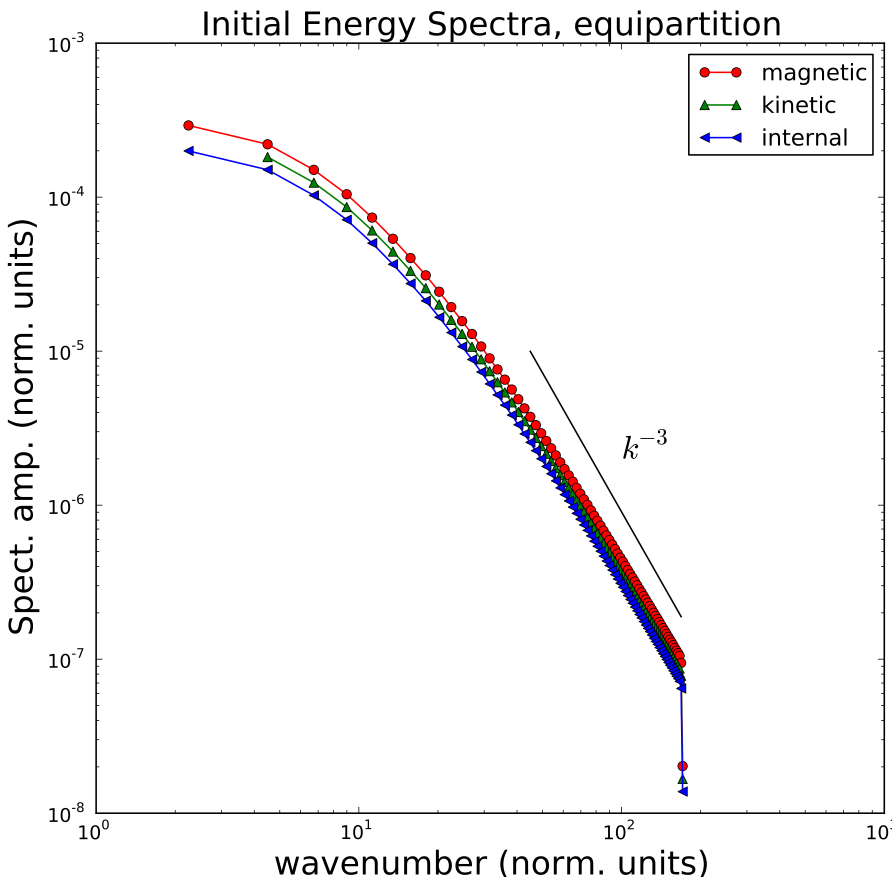

Figure 3.1: Initial energy spectra for simulation with equipartition between internal, kinetic, and magnetic components. The magnetic (red circles) and internal (blue triangles) spectra are offset by a small factor ($\pm\log(1.1)$, respectively) from the kinetic spectra (green triangles) to reveal the identical spectral exponents. Without the offset, the three spectra align exactly. A line with spectral exponent k^{-3} is plotted for comparison. The energy spectra approach k^{-3} for medium-to-large k.

$$\begin{aligned} E_B(k) &= k^2|\psi_k|^2 \\ E_K(k) &= k^2|\phi_k|^2 \\ E_I(k) &= \alpha|n_k|^2. \end{aligned} \tag{3.18}$$

The initial phases are either cross-correlated or uncorrelated. By cross-correlated we mean that the phase angles for each Fourier component for different fields are equal. In general,

$$n_k = A_k \mathrm{e}^{i\theta_1(\mathbf{k})}, \qquad \psi_k = B_k \mathrm{e}^{i\theta_2(\mathbf{k})}, \qquad \phi_k = C_k \mathrm{e}^{i\theta_3(\mathbf{k})}, \tag{3.19}$$

where A_k, B_k, and C_k are the (real) amplitudes of the Fourier modes, set according to the spectrum power law. For cross-correlated initial conditions, $\theta_1(\mathbf{k}) = \theta_2(\mathbf{k}) = \theta_3(\mathbf{k})$ for each $\mathbf{k}$. For uncorrelated initialization, there is no phase relation between corresponding Fourier components of the n_k, ψ_k, and ϕ_k fields.

The initial correlations have implications for the amplitudes of the long-lived structures in density, magnetic, and current fields. Ampere's Law dictates that mergers between circular structures occur for parallel current filaments only. When the initial conditions are correlated, a positive (negative) current filament will be associated with a positive (negative) density fluctuation for the duration of the simulation. A merger between two current filaments will merge their like-signed density fluctuations, and like-signed density fluctuations will frequently merge with other like-signed fluctuations. This provides many opportunities for merged density fluctuations to grow in intensity through successive mergers. For uncorrelated initial conditions, a positive current filament may be associated with a positive or negative density fluctuation. Mergers between current filaments will frequently merge density fluctuations of opposite sign, providing the opportunity for net cancellation of the density field in the merged region. If significant differences in the large-scale structures in the density field exist between uncorrelated and correlated initial conditions, this merger cancellation effect may be in play.

One mitigating factor in the above picture of density structure amplification through mergers is the generation of uncorrelated turbulence in the course of merger events. Mergers being high-energy events, they generate turbulence in a local (in real space) cascade. Relative to the length scales of merging density structures, the generated turbulence has a small correlation scale. A fraction of the turbulence inevitably is incorporated into the merged structure, and this incorporated turbulence decreases the density structure amplitude.

The effect of phase correlation on the profiles of filamentary structures and on the global statistics will be seen in chapters 4 and 5.

The results in Craddock et al. (1991) focused on the formation and longevity of current filaments in a turbulent KAW system, and solved the two-field model, Eqns. (2.15) - (2.16). To preserve small-scale structure in the current filaments, these numerical solutions set $\eta = 0$ and had $\mu \sim 10^{-3}$, with a resolution of 128×128, corresponding to a k_{max} of 44. Large-amplitude density structures that would have arisen were damped to preserve numerical stability up to an advective instability time of a few hundred Alfvén times, for the parameter values therein.

The numerical solutions presented in subsequent chapters explore a range of parameter values for η and μ. They make use of hyper-diffusivity and hyper-resistivity of appropriate strengths to preserve structures in n, B, and J. An advective instability is excited after $\sim 10^2$ Alfvén times if resistive damping is negligible. The $\eta = 0$ solutions—not presented here due to their poor resolution of small-scale structures—see large-amplitude current filaments arise, but they can be poorly resolved at this grid spacing. With no resistivity, the finite number of Fourier modes cannot resolve arbitrarily small structures without Gibbs phenomena resulting and distorting the current field.

We have found through experience that small hyper-resistivity and small hyper-diffusivity preserve large-amplitude density structures and their spatial correlation with the magnetic and current structures, while preventing the distortion resulting from poorly-resolved current sheets and filaments. They allow the numerical solutions to run for arbitrarily long times, and the effects of structure mergers become apparent. These occur on a longer timescale than the slowest eddy turnover times.

3.2 Discussion and Conclusions

This chapter has described a general framework for explicit numerical schemes that employ an integrating factor to evolve the linear terms exactly. The integrating factor formulation can incur significant computational cost, depending on the difficulty in diagonalizing the linear coefficient matrix $\mathcal{L}_k$ and the computational cost in computing $\exp(\Delta t \mathcal{L}_k)$. These computational costs are to be weighed against the stability constraints coming from the linear terms in $\mathcal{L}$. If the CFL constraints are dominated by constraints stemming from discretizing the parabolic damping terms, then the integrating factor formulation may possibly provide net computational gain by evolving these terms exactly. Parabolic constraints are often more strict than hyperbolic constraints stemming from nonlinear terms. An alternative method to evolve equations with strict stability constraints is to formulate the scheme implicitly, rather than explicitly. In our system, it is desirable to resolve KAW modes over a wide range of scales so that the long-term emergent features that result after small-scale structures merge may become evident. Resorting to implicit numerical schemes to evolve quadratic nonlinearities incurs some degree of approximation for small-scale modes. Employing an implicit scheme to evolve the nonlinear terms does not resolve the small-scale features as accurately as an explicit scheme, which can be a requirement in turbulent systems. It is possible to evolve the linear terms implicitly and the nonlinear terms explicitly, however, and would circumvent these shortcomings.

The second part of this chapter described the initializations used in the numerical solutions to be presented in subsequent chapters. The importance of the effect of different phase correlations on the amplitudes of density structures was also described.

4 LOCAL ANALYSIS OF STRUCTURES IN KAW TURBULENCE

Filaments, sheets, and active turbulence comprise the three categories into which decaying turbulence partitions itself, and these three components are expected in driven turbulence as well.[1] The two-timescale analysis and subsequent asymptotic balances presented in chapter 2 indicate that KAW turbulence can be expected to have quasi-circular filaments in density, current, and magnetic fields. A large-amplitude current filament at the center of each filament generates a $B_\theta(r)$ field with sufficient radial shear to preserve the structure from turbulent disruption. In addition to these radially symmetric structures, elongated sheet-like structures are also expected in KAW turbulence, as both quasi-circular and sheet-like structures have identically zero nonlinear terms in Eqns. (2.9)–(2.11). The significance is that filaments and sheets do not participate in nonlinear transfer of energy to different scales, and can exist on long timescales in relation to turbulent timescales.

In this chapter we focus on refining methods and techniques for separating filamentary structures from the rest of a turbulent domain. First we investigate the Hessian of ψ, a scalar field calculated from the matrix of second-order derivatives of ψ. The usefulness of the Hessian is its ability to characterize coherent structures having a magnetic shear boundary layer in the edge. Following that, we develop a technique inspired by Geographical Information Science using, again, the ψ field to separate all flux tubes from the background field. We will show that the flux-tube population in decaying KAW turbulence has unique properties as compared to the background field. We argue that the flux tubes serve as an adequate proxy for the filamentary structures defined in chapter 2.

[1]No analytical development for sheet-like structures was presented in chapter 2, however, and sheet-like structures will be quantified statistically in chapter 5.

This chapter does not develop techniques for separating long-lived sheet-like structures from filamentary structures or turbulence. Sheets are non-localized, and their boundaries are significantly more difficult to delineate in a robust fashion, whether analytically or algorithmically. Certain statistical properties of sheets will become evident in following chapters; their local analysis is deferred to future work.

Throughout the chapter, our focus is on the local physical properties of quasi-circular structures, rather than a global statistical description of the turbulent fields. Our approach makes necessary a means to define the center and boundary of filamentary structures, which motivates our development of a technique for distinguishing filaments from everything else. Other approaches that emphasize a global statistical understanding do not require separating components from each other in a turbulent field. Representative of the global statistical approach are the structure functions of She and Leveque (1994). Here we confine our focus to a localized understanding of how filamentary structures can exist when immersed in a turbulent bath, and how these structures can then contribute to making the turbulent field intermittent. For example, rather than describing the structure functions for the velocity field, we are interested in the radial profiles of the current, magnetic, density, density gradient, and Hessian fields of individual quasi-circular structures.

In the following sections we investigate the theoretical properties of the Hessian of ψ for turbulence, sheets, and quasi-circular structures. We then develop a technique for robustly distinguishing flux tubes from turbulence, and investigate their properties. Combined, these two means of distinguishing quasi-circular structures from the other two components of decaying KAW turbulence emphasize the quantifiable uniqueness of quasi-circular structures when compared to the remaining components, suggesting that these structures may contribute significantly to large scattering events in pulsar scintillation.

Examples of four individual structures demonstrate the variety of radial profiles in different fields associated with each structure. We show that the characteristic radii of structures in different fields correspond to theoretical expectations; that structures have suppressed nonlinearity densities and enhanced energy densities; and that structures have a greater degree of alignment than the background.

4.1 Structure Identification - Hessian Field

Key aspects of the analysis in chapter 2 can be quantified via the *Hessian matrix*, H, and its determinant (Servidio et al., 2010; Craddock et al., 1991; Terry, 2000; Terry and Smith, 2007) [2]. (Hereafter the term *Hessian* is used interchangeably with *Hessian determinant*.) If ξ is a C^2 scalar field, the Hessian of ξ is the matrix of second partials of ξ,

$$H(\xi) = \begin{pmatrix} \partial_{xy}\xi & -\partial_{xx}\xi \\ \partial_{yy}\xi & -\partial_{yx}\xi \end{pmatrix}. \tag{4.1}$$

Equating mixed partial derivatives, the determinant of Eqn. (4.1) is

$$det(H(\xi)) = \partial_{xx}\xi \; \partial_{yy}\xi - (\partial_{xy}\xi)^2. \tag{4.2}$$

The Hessian has desirable properties, among which are its ability to distinguish some coherent structures from turbulence, and to serve as a predictive diagnostic. By formal inspection, the Hessian field is positive (and has a local maximum) whenever the underlying scalar field ξ is at a local maximum or

[2] In Craddock et al. (1991), Terry (2000) and Terry and Smith (2007), the field known as the *Gaussian Curvature*, C_T is actually the determinant of the Hessian. The Gaussian Curvature is directly proportional to the Hessian determinant; the quantities differ by a denominator term. Compare the definition for C_T in Porteous (1994) to the Hessian in Binmore and Davies (2007).

minimum, where the repeated partial term dominates the mixed partial term. The Hessian is negative at saddle points (and has a local minimum) where the mixed partial term dominates the repeated partial term.

It is helpful to consider $H(\psi)$, the Hessian of the flux field, in polar coordinates. Transforming Eqn. (4.2) from Cartesian to polar coordinates and distinguishing fluctuating from coherent components yields

$$det(H(\psi)) = \left[J_0 + \tilde{j}\right]^2 - \left[r\partial_r\left(\frac{\tilde{b}_r}{r}\right) - \frac{1}{r}\partial_\theta \tilde{b}_\theta\right]^2 - \left[r\partial_r\left(\frac{B_\theta + \tilde{b}_\theta}{r}\right) + \frac{1}{r}\partial_\theta \tilde{b}_r\right]^2. \tag{4.3}$$

In Eqn. (4.3), $det(H(\psi))$ is large and positive at the center of a structure, where turbulence is suppressed and J_0 is at a maximum. At the edge of a coherent localized structure, J_0 diminishes relative to the core, and the shear term, $\partial_r(B_\theta/r)$ becomes maximum, making $det(H(\psi))$ large and negative. Outside the filament, $det(H(\psi))$ is governed by $\tilde{b}_\theta$, $\tilde{b}_r$ and $\tilde{j}$. These components are in approximate balance; otherwise the conditions for forming a coherent structure are satisfied and a structure should be present. Hence, $det(H(\psi))$ for a coherent structure will have a large positive core surrounded by a negative annulus of magnetic shear. In turbulent regions, $det(H(\psi))$ will be small.

The Hessian of ξ can be formulated in terms of the local curvature of a field, and this formulation can help give insight into the Hessian's limitations as a diagnostic tool. At every point on the scalar field ξ one defines two quantities termed the *principal curvatures*. For a hemisphere, the principal curvatures at every point are both constant, and are both positive for domes, both negative for cups. At saddle points, the principal curvatures are of opposite signs. For a flat region, both principal curvatures are exactly zero. An elongated sheet will have one curvature zero, the other positive or negative. The Hessian is proportional to the product of the principal curvatures, and this has implications as to the

Hessian's suitability for distinguishing sheet-like structures from turbulence. This formulation makes it obvious as to why the Hessian is always positive for both peaks and troughs, since the product of two negative principal curvatures will be a positive quantity. The Hessian is always negative for saddle-like regions because the principal curvatures there are of opposite sign.

Elongated sheet-like structures have one dimension that has large curvature (the dimension transverse to the sheet's length) and a second dimension with diminished curvature that approaches zero (the dimension along the sheet's length). The Hessian for sheet-like structures is diminished by the diminished curvature dimension, and the Hessian for sheets is small. As demonstrated previously, the nonlinear terms in the KAW equations are identically zero for sheets, so sheets do not participate in nonlinear interactions and may persist for long timescales in comparison to turbulent timescales. The Hessian will not distinguish sheets from turbulence even though sheets are persistent, large-scale and large-amplitude structures. The Hessian's value is in distinguishing coherent filaments from turbulence and sheets.

Figure 4.5 shows $|B|$ and the Hessian of the underlying ψ field after evolving some time from randomized initial conditions for a representative run with $\alpha = 1$. Associated with each quasi-circular structure in $|B|$ is a prominent peak in $H(\psi)$, and each large peak in $H(\psi)$ is surrounded by a negative annulus where the radial shear in B_θ is at a maximum. The elongated sheet-like structures visually prominent in $|B|$ are suppressed by $H(\psi)$.

The positive-core-negative-annulus signature of the Hessian field for a coherent structure gives an indication that a coherent filamentary structure has a center containing a large current filament and an edge with large radial magnetic shear. Another formulation of structures by means of flux tubes and their separatrices encompasses all coherent structures as defined by the Hessian

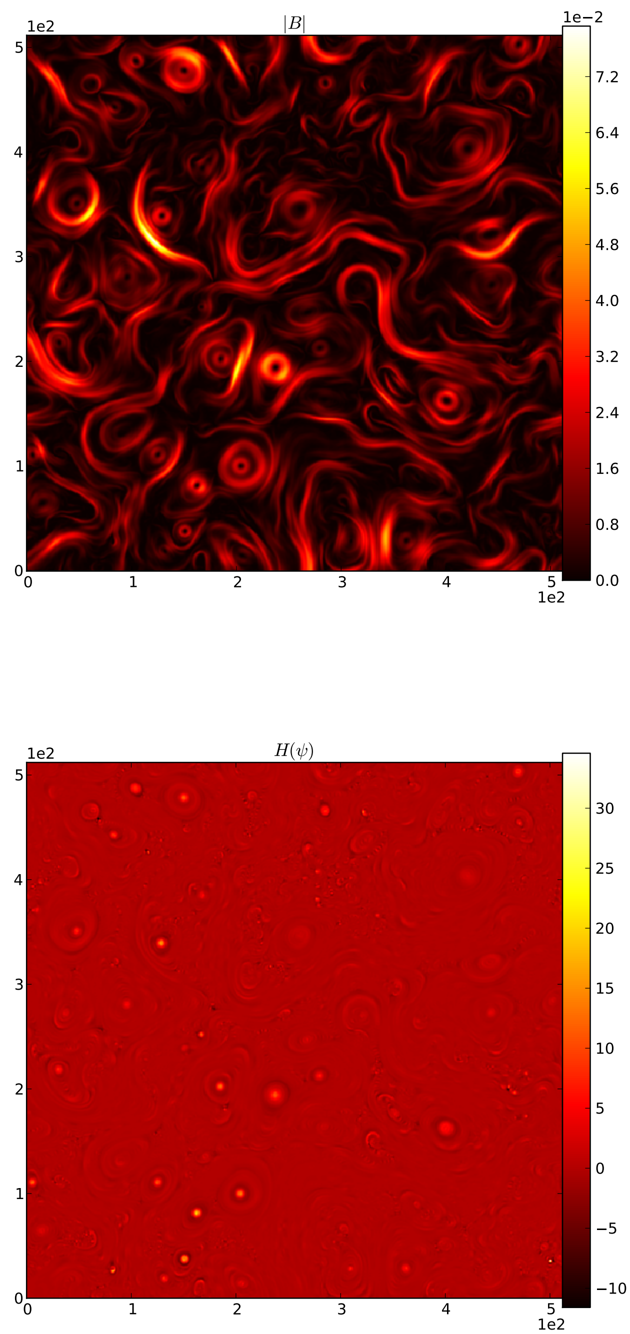

Figure 4.1: $|B|$ and $H(\psi)$ for the same ψ field. The nearly circular $|B|$ structures are enhanced in the $H(\psi)$ field, while the elongated sheet-like structures in $|B|$ are suppressed in $H(\psi)$. The enhanced structures in $H(\psi)$ have the positive-core-negative-annulus signature discussed in the text.

field and has the added benefit of easily delineating the structure boundary. This technique is developed in the next section.

4.2 Structure–Turbulence Discrimination

Magnetic nulls, the set of points at which $\nabla\psi = \mathrm{B} = \mathbf{0}$, include all points that are local extrema in ψ—known as *O points*, *peaks*, or *pits*—and the locations of magnetic reconnection—known as *X points*, *saddle points*, or *passes*. In a turbulent field, O points and X points move as the magnetic field is advected in time. The nulls are destroyed when reconnection merges two like-signed flux regions (or like-signed current filaments), and they are created in the presence of tearing instabilities. Details of critical point selection and identification on a discrete grid are discussed in appendix A.

There exist physically meaningful spatial regions definable by X points and O points, and the boundaries of these regions separate filaments from turbulence and sheets in a robust manner. To describe these regions, it is instructive to consider the two-dimensional ψ field as a topological surface embedded in three dimensions. By treating ψ as a surface, we can bring to bear the constructs developed in Geographical Information Science (Servidio et al., 2010; Rana, 2004; Carr et al., 2003; Carr, 2004), which has developed useful techniques for extracting connections between critical points on an N-dimensional scalar manifold (in our case, the magnetic nulls on the 2-dimensional ψ field) (Rana, 2004). The O points are local extrema of ψ, and the X points are the saddle points of ψ. One way of connecting X points and O points, the *surface network*, will be described presently. Each saddle point has associated with it one direction of positive curvature $\mathbf{c}_+$ and one direction of negative curvature $\mathbf{c}_-$. By ascending along every ridge line starting at $\pm\mathbf{c}_-$, it is possible to associate each X point with two peaks (possibly not unique). By descending along every course line

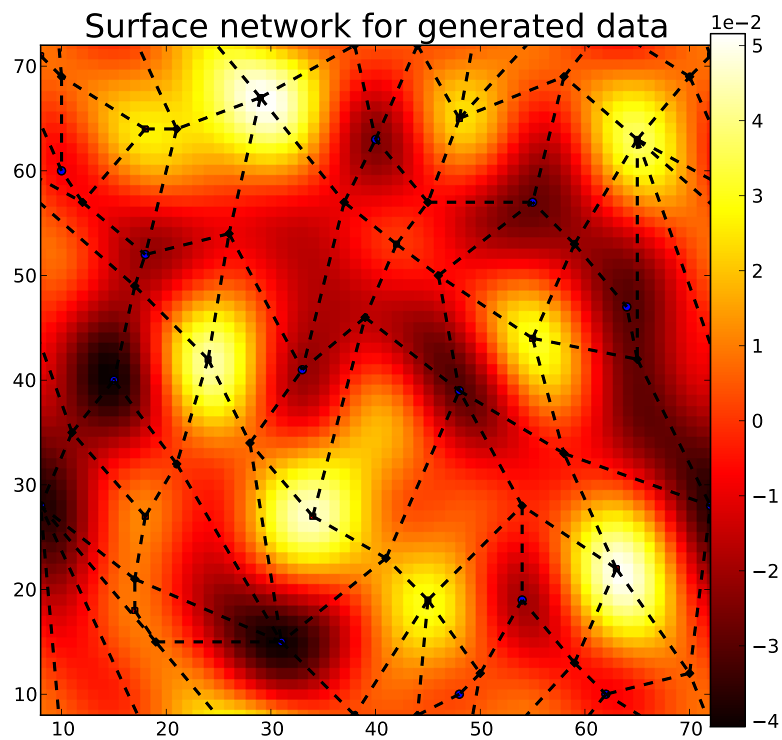

Figure 4.2: The surface network for a generated 2D scalar field. The critical points are indicated as red squares for local maxima (peaks), blue circles for local minima (pits) and black diamonds for saddle points (passes). Together, the peaks and pits comprise the O points, and the saddle points are the X points. The surface network of connections between X points and O points are indicated. Each X point is connected to four O points, two peaks and two pits. Each peak and each pit is connected to one or more saddle points.

starting at $\pm\mathbf{c}_+$, one can do the same for two pits. These connections form the surface network, and in it every X point is connected to two peaks (local maxima) and two pits (local minima). Every O point in the surface network is connected to one or more X points.

A surface network for generated data is shown in figure 4.2. There, the edge connectivity is periodic in both dimensions, and the connections of the surface network are shown in dotted lines. In the figure, the number of X points equals the number of O points, a constraint dictated by the Euler equality and the edge connectivity (Rana, 2004).

The surface network allows one to define disjoint spatial regions, each of which encompasses a magnetic flux tube. Consider a peak critical point in the surface network, p_a, and the set of its connected saddle points, $S_X = \{X|X \text{ is connected to } p_a \text{ in the surface network}\}$. Each saddle point in S_X has a ψ value of $\psi(X)$, all of which are smaller than $\psi(p_a)$, p_a being a local maximum. The saddle point X_m with the largest value of $\psi(X)$ for all $X \in S_X$ is the closest saddle point to p_a in terms of the flux field ψ isocontours. The point p_a and its maximal saddle point X_m define bounding isocontours, p_a from above, X_m from below. The spatial region of ψ bounded by these isocontours is the flux-tube region we are after. By associating every O point with its closest X point in this manner, and defining the region in ψ bounded by their isocontours, one defines a flux tube associated with every O point. An advantage to this method of defining flux tubes is that it is not dependent on an amplitude cutoff or adjustable parameter, and the method distinguishes both small- and large-scale flux tubes from their surrounding environment.

In addition to selecting individual flux-tube regions, the surface network also associates flux tubes in an hierarchical manner, such that flux tubes that are "closest" in terms of flux coordinates are grouped before flux tubes that are further away. These higher-order flux tubes can be thought of as larger flux tubes with interior structure, and a hierarchy of nesting flux tubes results.

Coherent filamentary structures correspond to flux tubes with a large associated area, with large amplitude in an appropriately averaged sense, and with no or very little interior structure—i.e. the interior of the flux tube contains exactly one magnetic null, an O point. Turbulent regions correspond to regions that contain flux tubes with small area and small amplitude. Sheet regions are regions devoid of magnetic nulls, and are what remains after discarding coherent filaments and turbulent flux-tube regions. Sheets have large amplitude and contain no X points or O points.

Examples of Flux-Tube Selection

An example of flux-tube detection using a randomly generated scalar field is shown in figure 4.3. It uses the same example data as figure 4.2. In the figure, flux tubes are shown in white, and each flux tube encompasses an O point, and abuts an X point on its edge. The abutting X point for each flux tube is the closest X point in ψ contour distance to the O point of the flux tube, and in many cases is not the nearest X point to an O point in Euclidean distance. Also evident is that not every X point abuts a flux tube – these X points are associated with higher-order flux tubes, i.e. flux tubes that are a conglomerate of nested flux tubes. Details of the algorithm used to select flux tubes is given in appendix A.

Figure 4.4 visualizes the ψ field for numerical results that have advanced in time before many large structure mergers have taken place. Also plotted in the figure are the critical points—blue circles are local minima, red squares are local maxima, and black diamonds are the saddle points (X points). Three features are qualitatively apparent:

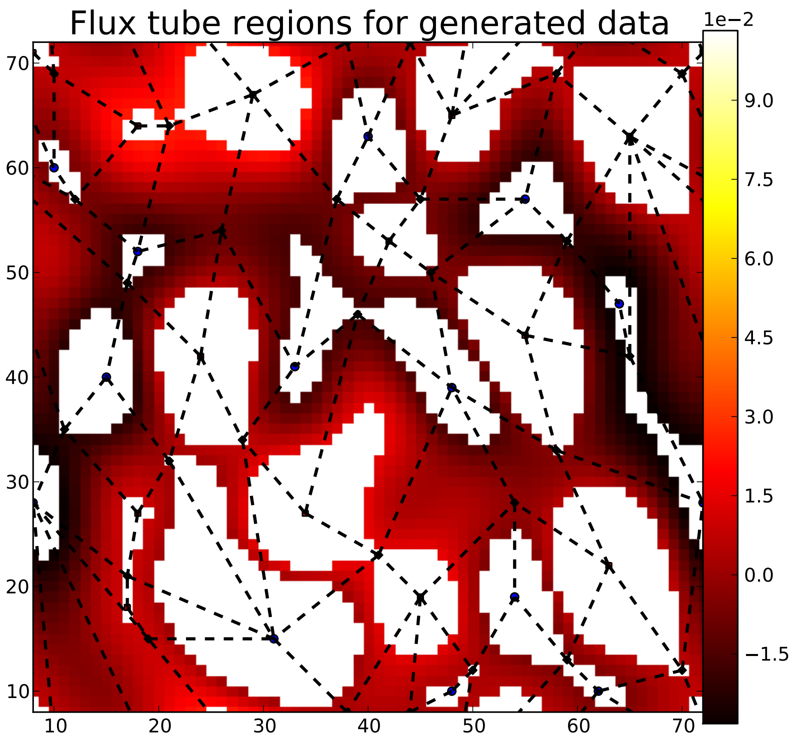

Figure 4.3: Same example data and surface network as figure 4.2, with flux-tube regions shown in white. Each flux tube encompasses an O point (red square for local maximum, blue circle for local minimum) in its interior and abuts an X point on its edge. The X point abutting a flux-tube region is the closest X point to the O point in flux surface contours. In many cases the nearest X point to an O point in flux contours is not the nearest X point in Euclidean distance.

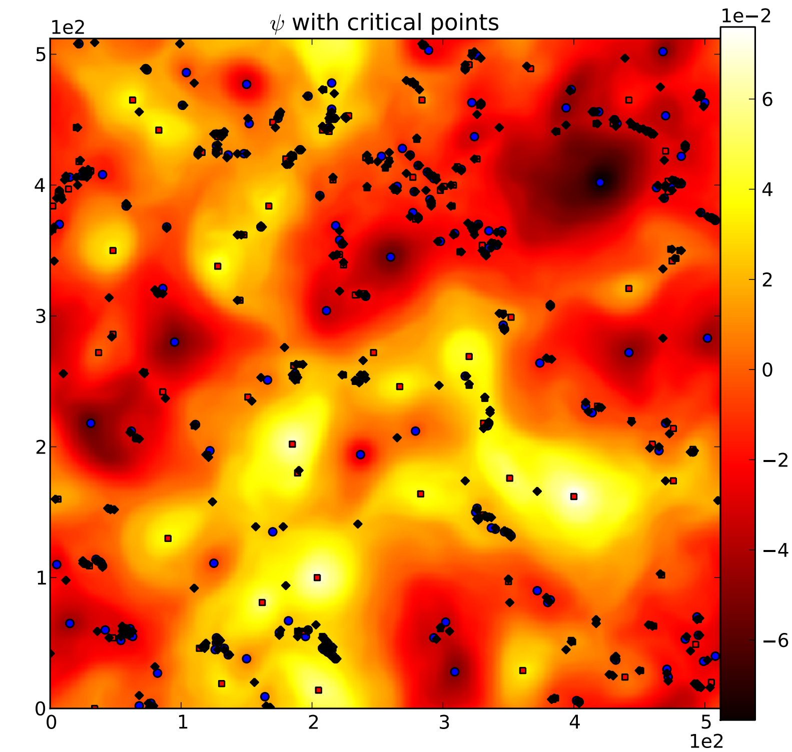

Figure 4.4: The ψ field with associated critical points. Blue circles are local minima, red squares are local maxima, black diamonds are saddle points. Together the local minima/maxima comprise the O points and the black diamonds are the X points.

- isolated large-scale basins with a minimum (maximum) point and large separation between the minimum (maximum) and the nearest critical point;
- regions with small inter-point distance and clustering of many critical points;
- regions devoid of all critical points and not evidently associated with either of the previous two classifications.

If a qualitative mapping from critical point regions to domain classifications is to be made, then the critical points with large separation correspond to the O points and X points of large-scale flux tubes, the critical points with small-separation are turbulent regions, and regions associated with no critical points are associated with magnetic field sheets.

The magnitude of the magnetic field, $|B|$, computed from the ψ field of figure 4.4 is shown in figure 4.5. The visually prominent large quasi-circular regions in $|B|$ correspond to the peak or pit basins in ψ associated with large-scale flux tubes. Each quasi-circular structure has $|B| = 0$ at the center where $|\nabla\psi| = 0$ and has a large-amplitude annulus surrounding the $|B| = 0$ core. Some quasi-circular structures in $|B|$ have a secondary ring at larger radius, often elliptically distorted. It is these large-scale quasi-circular regions that we propose to select and separate from the surrounding turbulence and elongated sheet-like structures. The behavior of the radial shear in B_θ outside the $|B| = 0$ core is of central interest to the theory developed in chapter 2.

Also prominent in figure 4.5 are elongated sheets that extend throughout the domain. Other than their elongation, sheets have arbitrary geometry and are not easily characterized by a few parameters; neither are they locatable to a confined region. The maximum sheet amplitudes are on the order of the

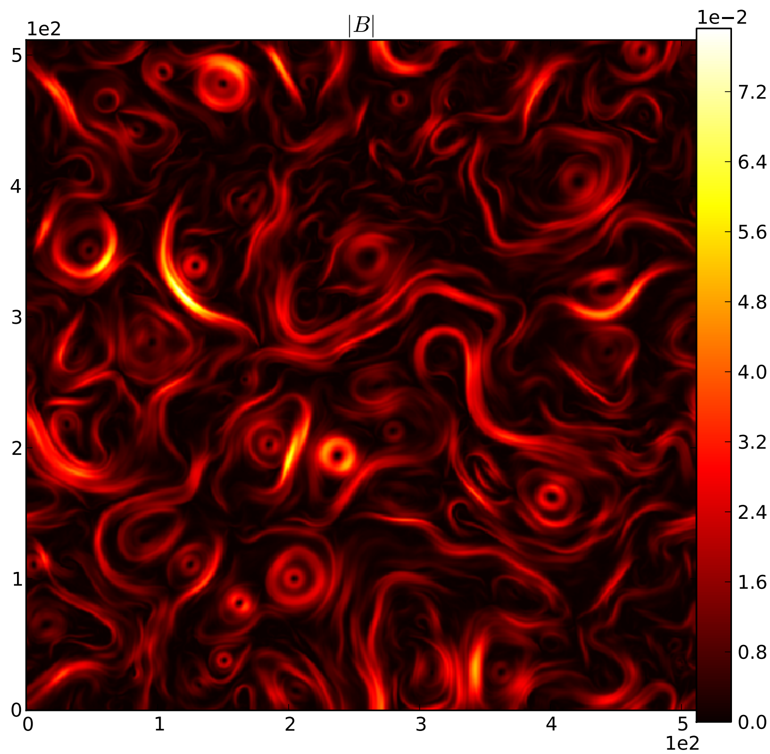

Figure 4.5: The $|B|$ field computed from figure 4.4. Visually prominent are the large-amplitude quasi-circular structures associated with the O points designated in the ψ figure.

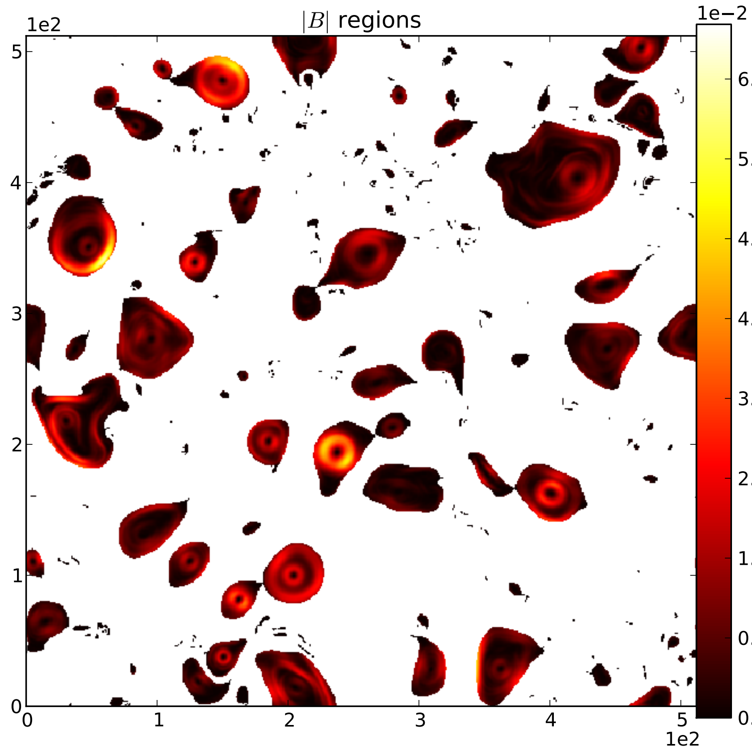

Figure 4.6: The regions selected using the algorithm described in the text. The field is the same $|B|$ field as in figure 4.5 with the unselected regions set to white. The selection procedure captures the large-amplitude/large-scale features visually evident in figure 4.5 in addition to small-scale features associated with turbulent regions.

maximum amplitudes for the quasi-circular filamentary structures. Given their non-local extent, sheets pose challenges for selection that filaments do not, and we do not develop techniques in the present work for separating sheets from the other components. Their aggregate features are described below and their statistical properties are included in subsequent chapters.

Figure 4.6 shows the same $|B|$ field as figure 4.5 with the non-flux-tube areas masked out (shown in white). The flux-tube regions and their associated quasi-circular structures are selected by the algorithm, and the algorithm captures the visually prominent circular features in $|B|$. The areas of the flux-tube regions range from a few grid points to thousands of grid points for the largest regions. The smallest flux-tube regions are associated with turbulent regions and the clusters of critical points in figure 4.4. The largest flux-tube areas contain a central filamentary structure that is quasi-circular, and the surrounding penumbra is often highly distorted and non-circular. It is the central quasi-circular structure that the shear boundary layer theory describes; the region surrounding the core structure is a secondary region that evolves with the background.

The primary limitation of the surface network and flux-tube selection as analysis tools is that they are only defined for a scalar valued field (ψ in our case). The analogue of the surface network for a three-dimensional magnetic field is the magnetic skeleton (Haynes and Parnell, 2010). The magnetic skeleton of a three-dimensional magnetic field is significantly more challenging to robustly calculate, and its generality is not necessary for the present work.

The isolation of individual flux tubes makes local region analysis possible. For example, a large amplitude flux tube selected by the selection algorithm can be characterized by its value at the O point and its associated X point, and the boundary radial magnetic shear can be approximated by probing the values of the magnetic field amplitude at the flux-tube boundary. The selected regions follow the magnetic field lines of the local separatrix, and gives a natural and physical delineation of the boundary for each flux tube, which is to be contrasted with threshold-based measures based on curvature. Selection methods based on the amplitude of current filaments, or on the amplitude of the Hessian of ψ (Terry and Smith, 2008), are successful at identifying the largest amplitude structures with a strong central filament that distinguishes it from surrounding turbulence and sheets. However, these criteria do not yield information on the radial extent of a coherent structure, and they are dependent on an arbitrary threshold parameter to select structures. The Hessian has value in that it is large and positive in amplitude at the core of filamentary structures, which can be used to indicate which filaments are the most dominant in amplitude and persistent in time in a domain. But it is unable to partition the domain into components.

The contour tree of the density field, as above, partitions the density field into three components: filaments, sheets, and turbulence. The KAW system would be expected to have general correspondence between structures in the density field and structures in the magnetic and current fields.

4.3 Radial Profile of Filamentary Structures

After defining structure boundaries via flux-tube extraction in the previous section, it is possible to investigate the dependence of fields of interest on distance from the flux-tube center. Here distance can specify radial distance from the flux tube's O point, or it can specify the ψ flux coordinate from the O point. The flux coordinate is a well-defined proxy for distance from the O point within the flux tube, where there is a one-to-one relationship between a single connected isocontour and flux coordinate. Radial distance from an O point is an acceptable measure for sufficiently quasi-circular flux tubes, but fails to accurately quantify distance from the O point in the case of elongated flux tubes. In the following figures, we use Euclidean distance as the radial measure, as it is generally applicable when the ψ vs. r relation is non-monotonic.

Figures 4.7–4.10 show four representative quasi-circular structures across six scalar fields. The field visualization for the structure is shown on the left and the $\hat{\theta}$-averaged radial profiles for each field are plotted on the right. The error bars in the $\hat{\theta}$-averaged profiles indicate the $\pm 2\sigma$ spread in values. The fields shown in each figure are, top to bottom, ψ, $|B|$, n, $|\nabla n|$, J, and $H(\psi)$. Overlaid on the field visualizations on the left are the separatrix in black surrounding the central quasi-circular structure. In many cases the separatrix is highly irregular and non-circular. The radial plots on the right include a horizontal zero-level in orange for reference.

Ideal Structure

Figure 4.7 displays a structure that corresponds to the theory in both qualitative and quantitative aspects. The ψ vs. r dependence is nearly linear with small deviations, and the core magnetic field structure is azimuthally symmetric and extends to $r \sim 0.1\rho_s$. In the density field, inside the separatrix, the core density structure is also azimuthally symmetric and well defined as determined by the error bars for $r < 0.15\rho_s$. The same can be said for the $|\nabla n|$ field, with a well-defined central core and small values between the central core and the separatrix radius. The density structure in the core is monotonically decreasing with radius until $r \sim 0.07\rho_s$. The $|\nabla n|$ field has a similar structure to the $|B|$ field: nearly zero for $r = 0$, a linear rise with a turn over at $r \sim 0.05\rho_s$ and flat outside the central core, with large fluctuations about the mean. The core $|\nabla n|$ structure is contained within a smaller $\langle r \rangle$ than the core $|B|$ structure. This is to be expected; if $n(r) \sim B(r) \sim r^{-1}$, then $n'(r) \sim r^{-2}$, and $\langle r_{\nabla n} \rangle < \langle r_n \rangle$, where

$$\langle r_F \rangle = \frac{\int_0^{r_{max}} \mathrm{d}r \, r|F(r)|}{\int_0^{r_{max}} \mathrm{d}r \, |F(r)|}. \tag{4.4}$$

The current field and J vs. r plot in figure 4.7 correspond to the theoretical expectations. The J field peaks at $r = 0$ then monotonically decreases to radius $r_J \sim 0.07\rho_s$, which is less than the $|B|$ core structure radius of $r_B \sim 0.10\rho_s$. For $r > r_J$ the $J(r)$ profile is near zero.

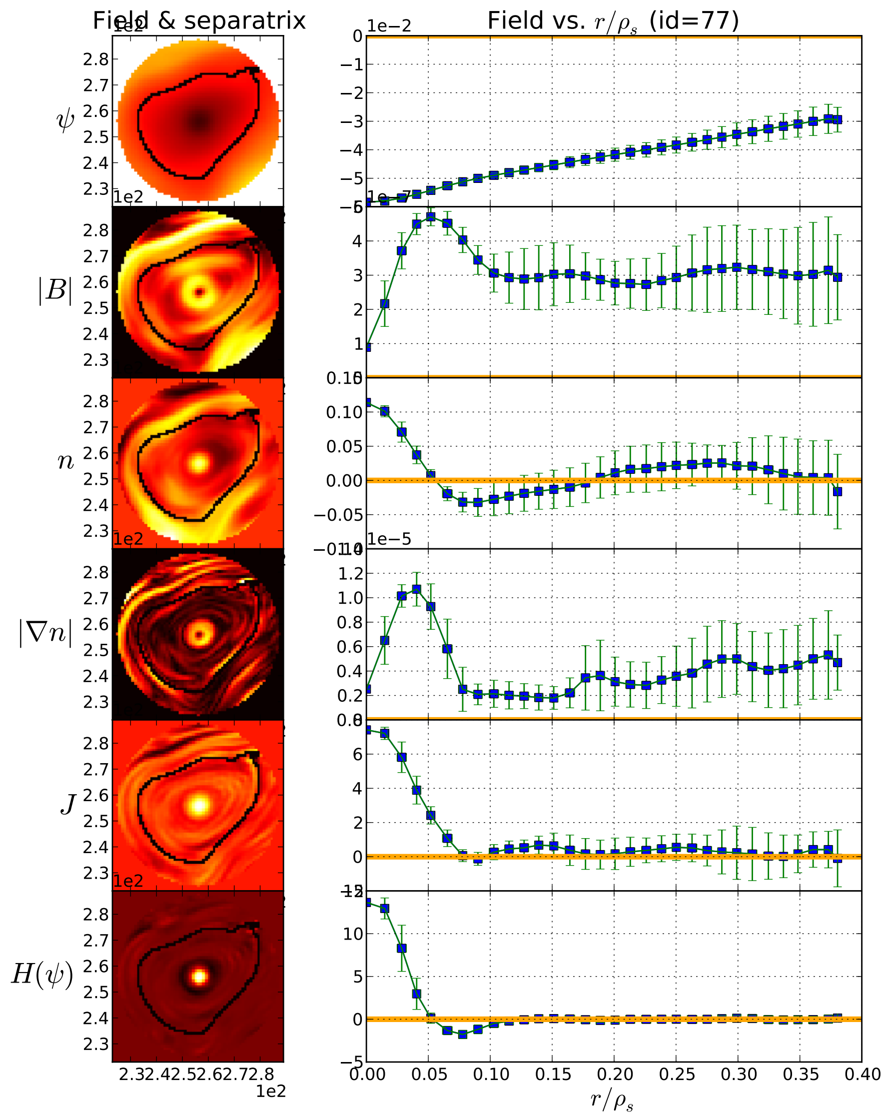

Figure 4.7: Fields, separatrix, and radial profiles with typical fluctuation levels for a structure that corresponds closely to theoretical expectations. The fields are shown in color on the left, with the separatrix indicated in black. The $\hat{\theta}$-averaged fields are plotted on the right. The error bars indicate typical fluctuation levels for the $\hat{\theta}$-averaged radius. The horizontal orange line indicates the zero-level for reference.

The Hessian of ψ, $H(\psi)$, in figure 4.7 also corresponds closely to theory for a coherent structure. From a peak at $r = 0$, $H(\psi)$ has a zero crossing at $r \sim 0.05\rho_s$, and is negative out to radius $r \sim 0.10\rho_s$. The positive central core is the large J_0^2 component in Eqn. (4.3). For $0.05 < r/\rho_s < 0.10$, $H(\psi)$ is negative, which corresponds to the negative square of the radial shear in B_θ, $-[\partial_r(B_\theta/r)]^2$ for the coherent structure. The shear is largest in absolute value surrounding the core J_0^2 component. For $r > 0.10\rho_s$, $H(\psi)$ is zero, with small fluctuation levels in relation to the maximal squared shear (about -2 at $r \sim 0.07\rho_s$) and the maximal squared current (about 14 at $r = 0$). The $H(\psi)$ core structure extends to $r \sim 0.05\rho_s < r_J$, which is expected from the form of Eqn. (4.3). In Eqn. (4.3) the competition between the positive J_0^2 term in the core and the negative $-[\partial_r(B_\theta/r)]^2$ term at the edge of the coherent structure necessarily reduces the zero-crossing point for $H(\psi)$ in relation to r_J.

Structure with Density Variation in Core

In comparison to the circularly symmetric structure in figure 4.7, the structure in figure 4.8 is an example of a coherent structure with strong elliptical distortion, but retains many expected characteristics nonetheless. The elliptical distortion in ψ is manifest in the distortion in the separatrix as well as the large fluctuations about the mean evident in the $\hat{\theta}$-averaged plots. Despite the elliptical distortion, it is possible to identify a coherent structure in all fields. In the n and $|\nabla n|$ fields it is discernible where the separatrix outlines the boundary between a region with lower overall density values inside as compared to outside, and the peak in $|\nabla n|$ that coincides with the separatrix demonstrates this fact quite clearly. The $n(r)$ and $|\nabla n|(r)$ plots show variation in the core. The variation in $n(r)$ is an example of the $\hat{\theta}$-smoothing process described in section 2.5, and the variations are seen in $|\nabla n|$ as well.

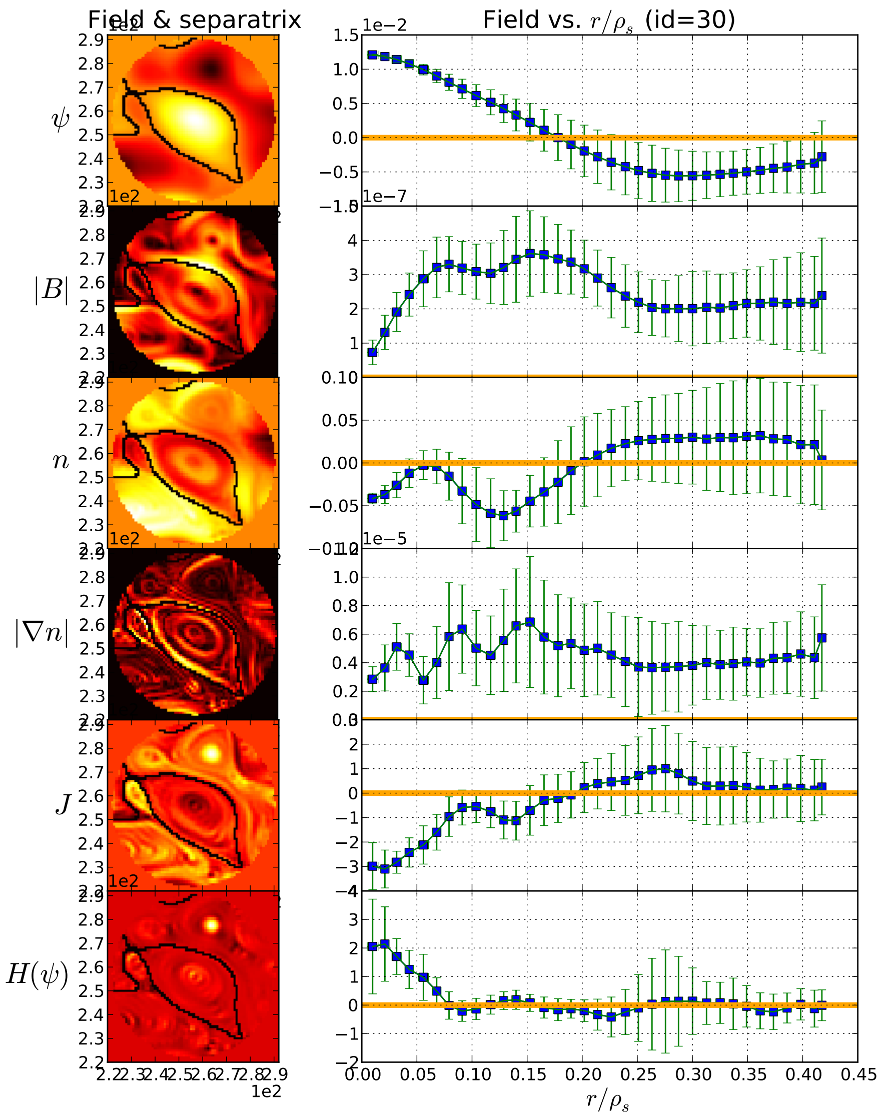

Figure 4.8: Structure with elliptical distortion and variation in the core of n and $|\nabla n|$.

The J and $H(\psi)$ radial profiles are less well-defined than the structure in figure 4.7, but the general theoretical predictions for these fields hold. The large fluctuation values in all radial plots are a manifestation of the elliptical distortion of the field, and the nearby structures that add to the fluctuation values for $r > 0.25\rho_s$.

The correspondence between the interior and exterior of the separatrix is clearly seen in the n and $|\nabla n|$ fields, revealing that the n and B fields have, in aggregate, similar correlation length scales in the vicinity of coherent structures.

For this structure, despite the elliptical distortion, n-B correspondence is evident, as expected from KAW interaction.

Structure with Small B_θ Amplitude

The third structure, shown in figure 4.9, is an example of a structure with weak $|B|$ amplitudes in the core while retaining strong n amplitudes in the core. The structure is well-defined and persistent, despite the weak $|B|$ core amplitudes. This structure gives an indication, again, that the overall amplitudes of n and $|B|$ may not correlate strongly in the core, but their spatial distributions do tend to correlate, when restricted to regions inside the separatrix for a given structure.

Magnetic Structure with Small Density Variation

The structure in figure 4.10 is an example of a structure with a localized separatrix region—about $1/4$ the area of the separatrix region of the previous three structures. The separatrix delineates the core structure in ψ, and cuts the $|B|$ field at its maximum value for the core structure. Notable is the absence of a structure in both n and $|\nabla n|$, despite the presence of a structure in all fields derivable from ψ. The absence of a structure in n and $|\nabla n|$ is borne out in the

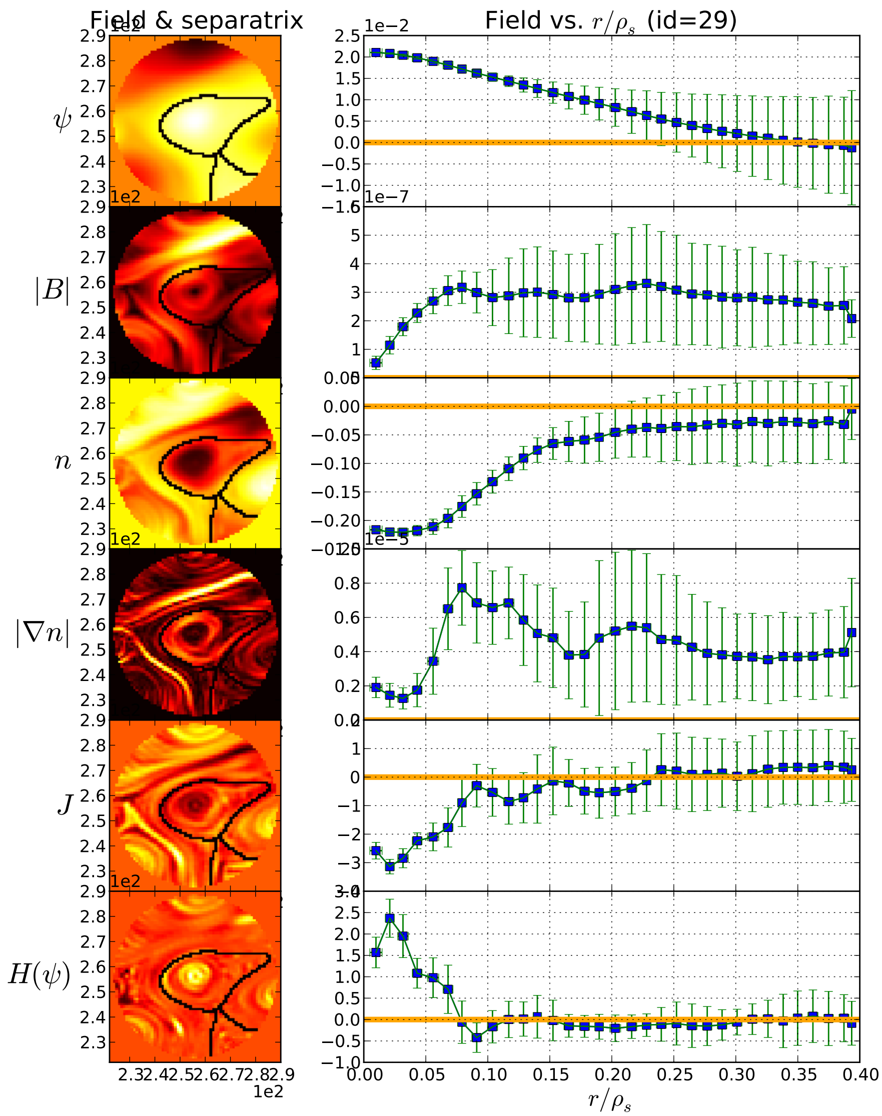

Figure 4.9: Structure with locally weak $|B|$ field and locally strong n field inside the separatrix boundary. The spatial correspondence between the $|B|$ and n core structure is evident within the separatrix.

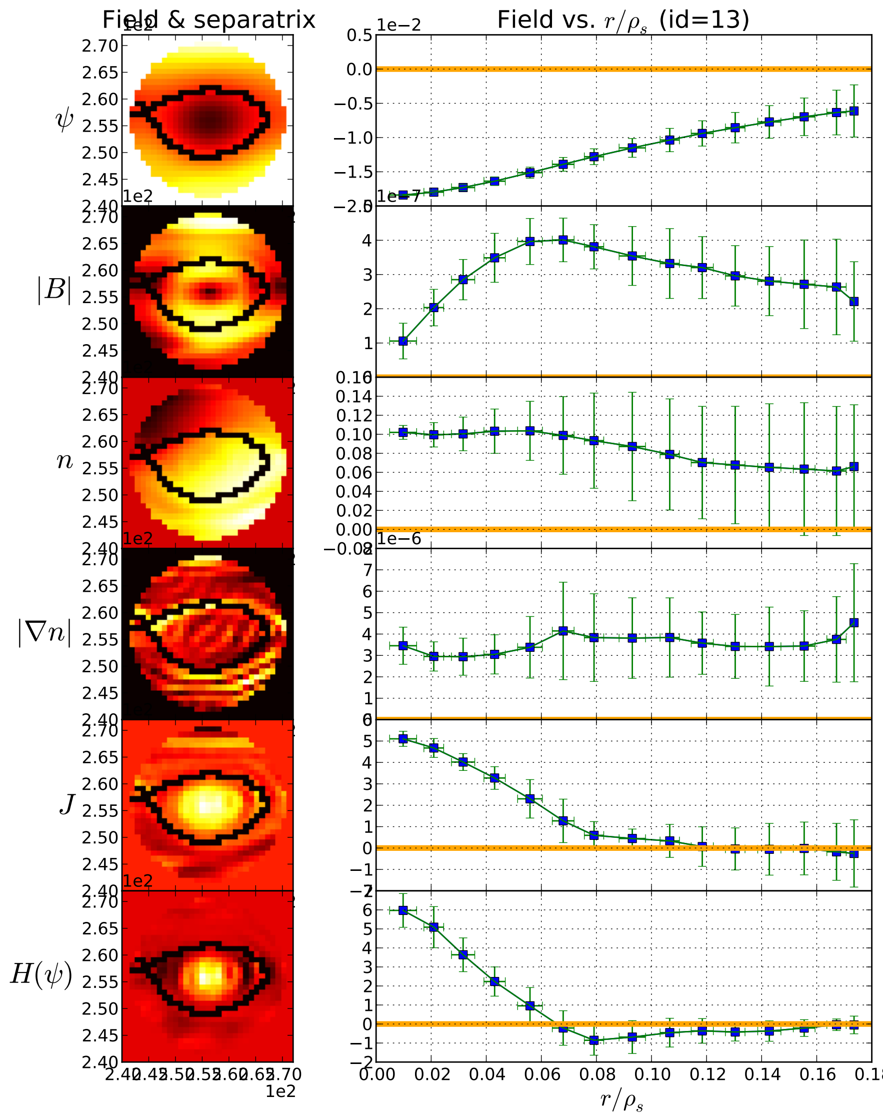

Figure 4.10: Structure with localized separatrix and clear definition in ψ, $|B|$, J and $H(\psi)$. The n and $|\nabla n|$ fields do not indicate the presence of a structure, however.

radial profiles, which are relatively flat with large fluctuations about the mean. The structure in figure 4.10 is a specific example of a central characteristic of KAW physics: that is, correspondence between n and B in the previous structures is an emergent feature of a turbulent KAW system. The averaging of n during structure mergers in the initial stages of turbulence decay accounts for the absence of a structure in n in this case.

Results in following sections will show that, despite the absence of a necessary link between n and B structures, the presence of a coherent structure in ψ, B, J, and especially $H(\psi)$ does tend to imply the presence of a density structure in n and $|\nabla n|$.

4.4 Radial Extent of Structure Fields

Key aspects of the theory in chapter 2 predict whether a field is more or less localized for an ideal structure. We use as measure of localization a typical radius, defined by Eqn. (4.4). For the particular structure shown in figure 4.7, the principal aspects of the theory hold: $\langle r_J \rangle \lesssim \langle r_B \rangle$, $\langle r_J \rangle \lesssim \langle r_B \rangle$ and, of particular significance, $\langle r_B \rangle \sim \langle r_n \rangle$. Do these relations hold over the range of structure sizes, amplitudes, and shapes?

Figure 4.11 shows $\langle r_{\nabla n} \rangle$ vs. $\langle r_n \rangle$ for a range of structure sizes. The squared correlation coefficient is 0.82, and the trend line has slope 0.89, indicating that $\langle r_{\nabla n} \rangle \sim 0.89 \langle r_n \rangle$ over a range of typical radii. Gradients tend to enhance and sharpen small features, and the typical density-gradient radius is expected to be smaller than the typical density radius. The non-negligible spread in values about the trend line is due to at least four factors:

- Elliptical distortion of structures introduces uncertainty in the structure radial profiles—uncertainty that grows with r. These are legitimately co-

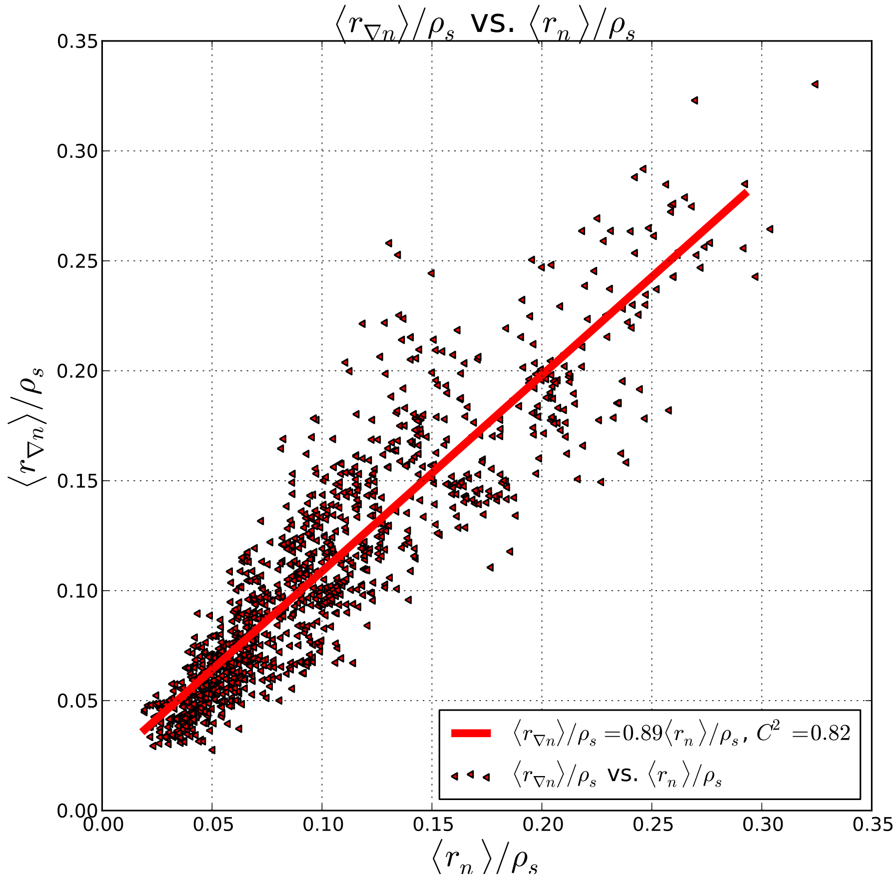

Figure 4.11: $\langle r_{\nabla n}\rangle$ vs. $\langle r_n\rangle$ for a range of structure sizes and time values. The trend line has slope 0.89, indicating that the typical radius for gradient structures is smaller than that of density structures. Processes that contribute to the spread about the trend line are described in the text.

herent structures, but their distortion from circular symmetry introduces error into $\langle r_F \rangle$.

- The calculation of $\langle r_F \rangle$ for significantly non-circular structures includes averaging fluctuations at the edges that are not within the structure separatrix.

- The $\langle r_F \rangle$ calculation yields consistent results for monotonically varying $F(r)$. Variation within the structure core can place more weight in the periphery of the density structure than would otherwise be present for a non-varying density structure.

- While the O point of structures is a slowly varying point in space, the X point can change from one time-step to the next for X points that are in dynamically active regions. The X-point variation changes the outer boundary of the separatrix from one timestep to the next, sometimes by large values. In terms of $\langle r_F \rangle$, this means the separatrix region can change by large values from one time step to the next, and tends to affect the structures with the largest areas. This is consistent with the typical spread in values being small for $\langle r_n \rangle < 0.07\rho_s$ as compared with the spread at $\langle r_n \rangle \sim 0.20\rho_s$.

Each of these factors introduces variation in the relation between $\langle r_{\nabla n} \rangle$ and $\langle r_n \rangle$, and contributes to the variation about the trend line in figures 4.11-4.14.

As in figure 4.11, figure 4.12 shows $\langle r_J \rangle$ vs. $\langle r_B \rangle$ for the same structures. Again, the trend line fits $\langle r_J \rangle \sim 0.90 \langle r_B \rangle$, indicating that the typical radius of the current field tends to be within the typical radius of the magnetic field of the structure.

Figures 4.11 and 4.12 plot the typical radius for the gradient of a field versus the typical radius for the field itself, limited to structure radii only. Given the

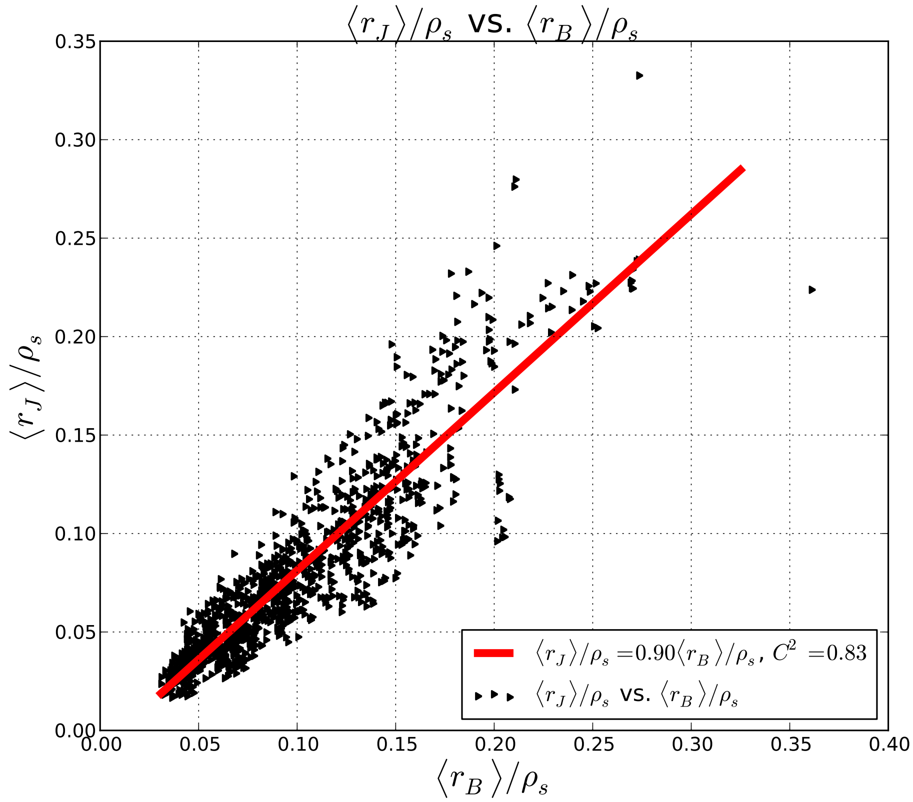

Figure 4.12: $\langle r_J \rangle$ vs. $\langle r_B \rangle$ for a range of structure sizes and time values. The trend line has slope 0.90, consistent with the 0.89 slope for the trend line in figure 4.11. The characteristic radius for the current of a coherent structure is typically smaller than that of the magnetic field. See the text for discussion of processes that contribute to the spread about the trend line.

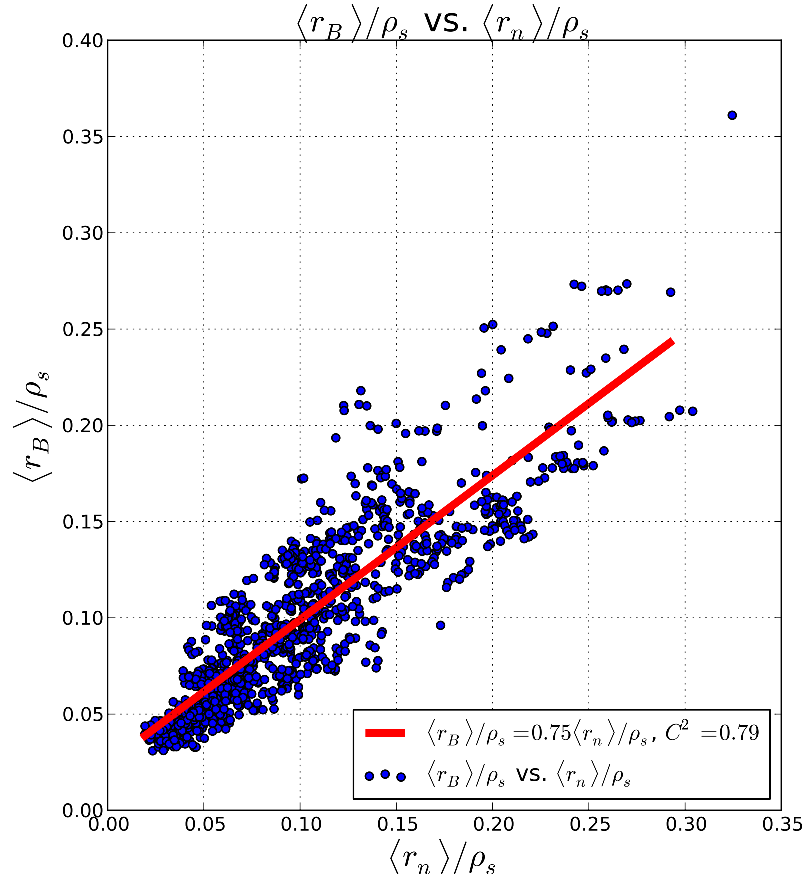

Figure 4.13: $\langle r_B \rangle$ vs. $\langle r_n \rangle$ for a range of structure sizes and time values. The trend line has slope 0.75, with a squared correlation coefficient consistent with figures 4.11 and 4.12. The slope value and moderate correlation indicate the density field is less localized than the magnetic field over a range of structure sizes, consistent with theoretical expectations.

strong relation between a field and its gradient in the core of a coherent structure, the relations shown in these figures are not unexpected. When either J or n are monotonic in the core of a coherent structure, the B field and the ∇n field take simple forms that have consistently larger $\langle r_B \rangle$ and smaller $\langle r_{\nabla n} \rangle$, respectively. The n and B fields are not related through a gradient; nevertheless figures 4.7-4.9 suggest that in many cases these fields can be expected to have comparable characteristic radii in the vicinity of coherent structures. The strength of the relation between $\langle r_B \rangle$ and $\langle r_n \rangle$ is a key test of the theory, which posits a near-linear scaling, and strong correlation.

Shown in figure 4.13 is $\langle r_B \rangle$ vs. $\langle r_n \rangle$ for the same population of structures. The trend line indicates $\langle r_B \rangle \sim 0.75 \langle r_n \rangle$, with squared correlation coefficient $C^2 = 0.79$. The value for the trend-line slope indicates that density is significantly less localized than B for a structure; the strong correlation indicates that quasi-circular density structures and magnetic field structures tend to exist together.

Lastly, with the relation $\langle r_J \rangle \sim 0.9 \langle r_B \rangle$ and $\langle r_B \rangle \sim 0.75 \langle r_n \rangle$, it is expected that $\langle r_J \rangle < \langle r_n \rangle$, with a slope somewhat less than 0.75. Figure 4.14 plots $\langle r_J \rangle$ vs. $\langle r_n \rangle$. Although it has a large spread in values and a correspondingly smaller squared correlation coefficient, the trend is consistent with the $\langle r_B \rangle$ vs. $\langle r_n \rangle$ and $\langle r_J \rangle$ vs. $\langle r_B \rangle$ plots, with slope 0.68.

4.5 Critical Point Numbers over Time

Over the course of a simulation of decaying turbulence, the number of critical points of all kinds will generally decrease, as mergers between regions reduce the number of critical points, and the median flux-tube area increases. Figure 4.15 plots the number of critical points and median areas of flux tubes vs. normalized time for the duration of a simulation initialized with energy

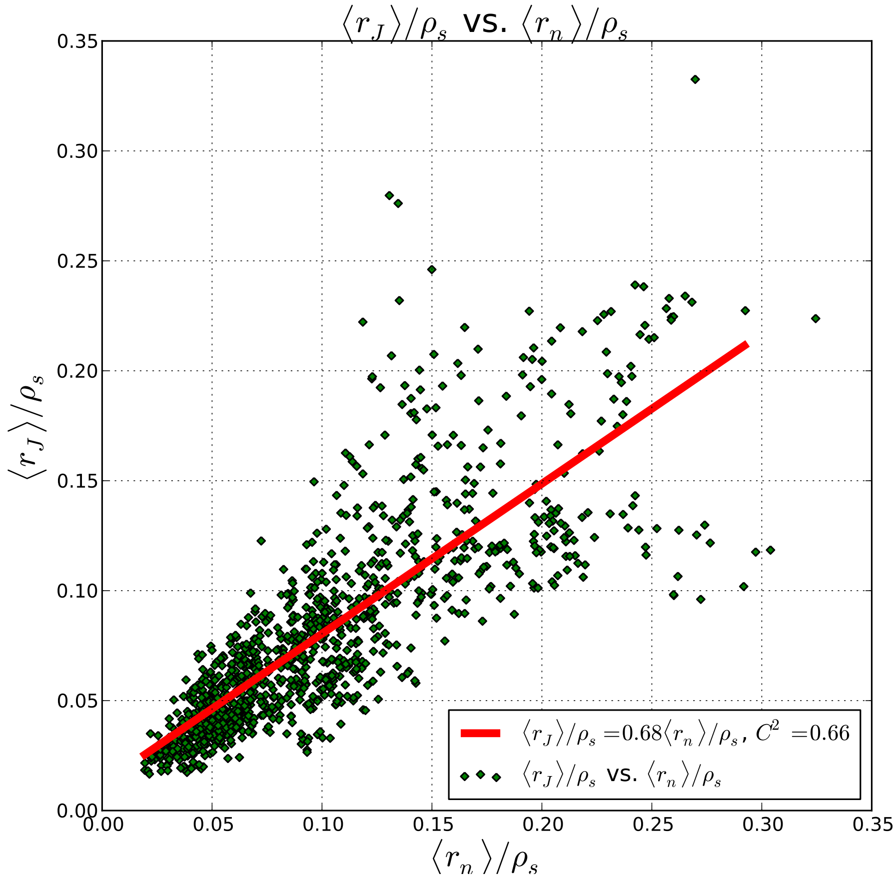

Figure 4.14: $\langle r_J \rangle$ vs. $\langle r_n \rangle$ for a range of structure sizes and time values. The trend line has slope 0.68, a value which is consistent with the product of the slopes in $\langle r_B \rangle$ vs. $\langle r_n \rangle$ (slope=0.75) and $\langle r_J \rangle$ vs. $\langle r_B \rangle$ (slope=0.90). The large spread in values about the trend line is discussed in the text.

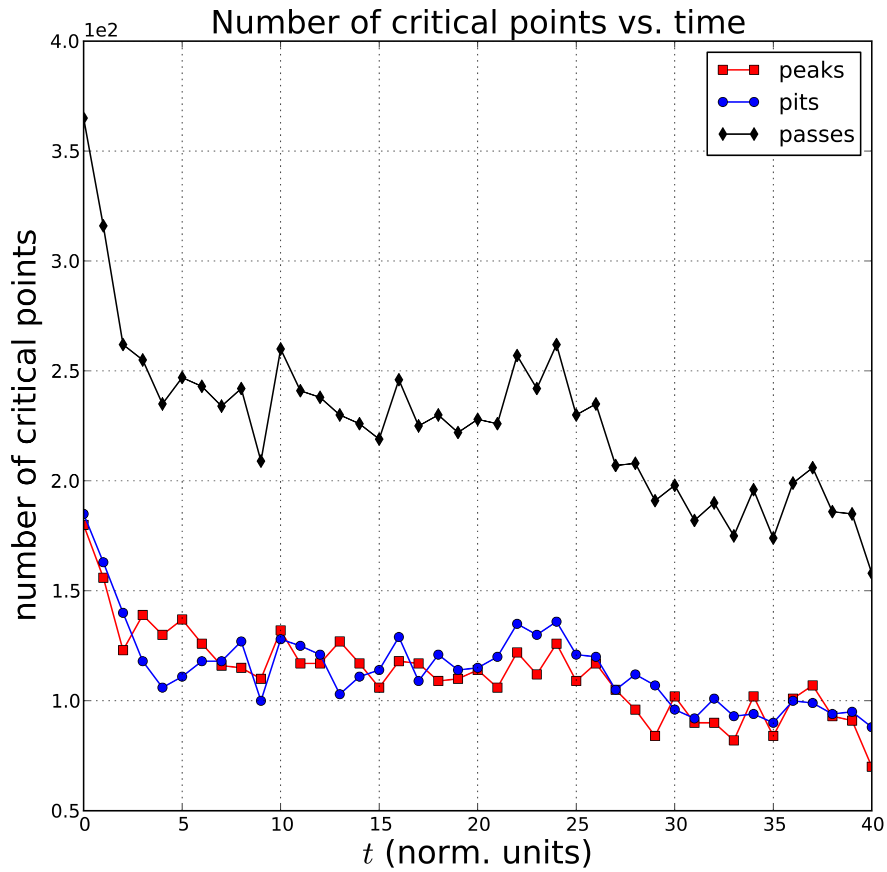

Figure 4.15: Number of critical points vs. time, according to the type of critical point. Passes (saddle points or X points) are plotted with black diamonds, peaks plotted in red squares, and pits plotted in blue circles. The relation $n_{peaks} + n_{pits} - n_{passes} = 0$ is an identity that holds for most of the values plotted, with deviations on the order of 2-3. The number of critical points, after decreasing initially, is fairly constant throughout the run, an indication of relatively constant flux-tube numbers in turbulent domains.

equipartition. The number of critical points decreases markedly in the initial stage, as many mergers occur between flux-tube regions. The quantity $|\frac{\Delta N}{\Delta t}|$ decreases, where ΔN indicates the change in number of critical points for peaks, pits, or passes over a time step. This decrease in the rate of change of the number of critical points indicates a relatively constant flux-tube population for small-sized flux tubes, corresponding to turbulent regions.

4.6 Energy Densities and Nonlinearity Densities

Variation of ψ within Flux Tube

Figure 4.16 plots the maximal change in flux inside the flux-tube regions vs. flux-tube area. This approximates $\Delta\psi$ inside a flux tube as a function of the areal extent of the flux tube. It is expected that $\Delta\psi$ varies with the flux tube area, as a larger flux tube samples a larger region and is expected to have a greater change in flux over its domain. Included in the figure is a trend line of this dependence, indicating a nearly-linear scaling between $\Delta\psi$ and flux-tube area. Also plotted (red circles) for comparison are $\Delta\psi$ for random regions in the domain. The quantity $\Delta\psi$ for random regions is an order of magnitude larger than for flux-tube regions for a given area, and the spread in values for $\Delta\psi$ is also an order of magnitude larger. The flux-tube regions are, in comparison to randomly chosen regions, areas within the domain with relatively small variation whose amplitudes scale as the area of the flux tube.

Energy Densities vs. Time

The coherent structures separated by the flux-tube selection algorithm detailed above form a sub-population embedded within a turbulent and dynamic background. It is of interest as to whether the energy density of the coherent structures is greater than that of the background. Theoretical expectations are

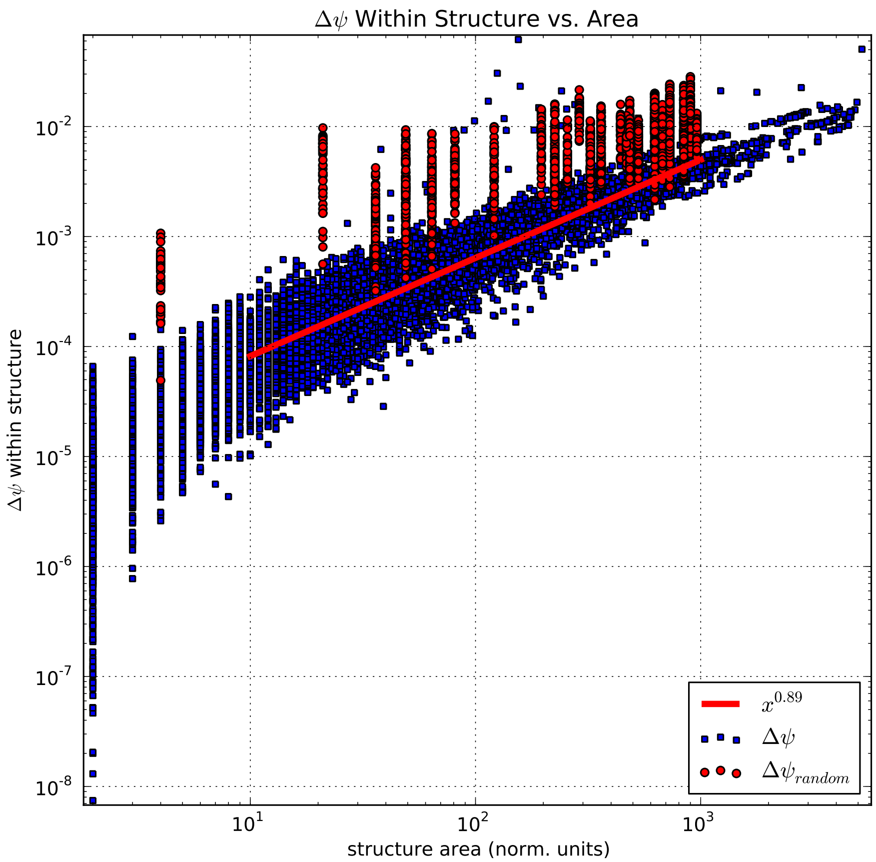

Figure 4.16: Log-log plot of the maximal change in ψ inside a flux tube vs. flux-tube area, with trend line. Plotted in red is the same quantity for random regions. Flux-tube regions have systematically smaller $\Delta\psi$ than random regions, with a smaller spread in values for a given area. The exponent on the trend line is consistently sub-linear for a range of simulation parameters and timescales.

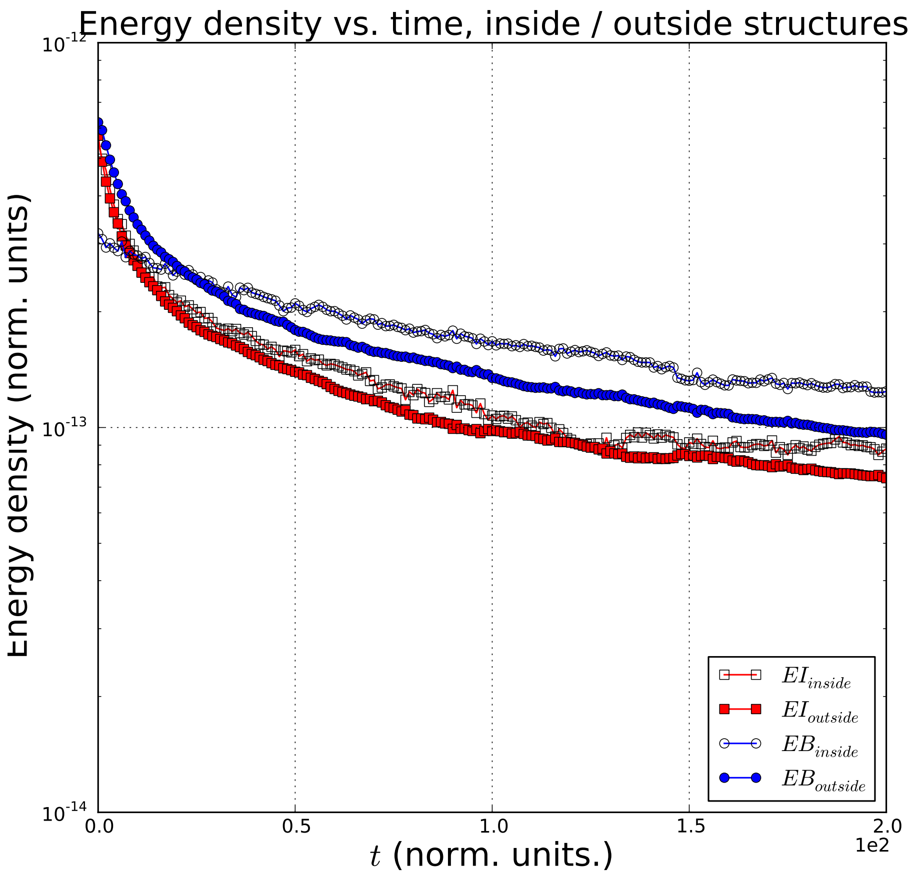

Figure 4.17: Energy density vs. time for inside and outside flux-tube regions, and for internal ($\propto n^2$) and magnetic energy. After an initial correlation stage, the E_{inside} for both internal and magnetic energies are consistently greater than $E_{outside}$.

that these structures would display a measurable increase in energy density over the background population, and retain their increase in energy density over time. This is an ancillary property of the shear preservation mechanism, preserving the fluctuation levels within the coherent structures from turbulent decay.

Shown in figure 4.17 is the energy density vs. time for four components: $E_{B_{outside}}/E_{B_{inside}}$, the magnetic energy outside and inside the flux-tube regions, and $E_{I_{outside}}/E_{I_{inside}}$, the internal energy $\propto n^2$ outside and inside the flux-tube regions. The time scale on the plot is from initialization until just prior to the merger between the largest coherent structures. All four components decrease in time due, primarily, to the nonzero damping terms in the KAW system. It is evident that $E_{B_{inside}} > E_{B_{outside}}$ for the majority of the time values, and this relation is reversed only during the initial stages. More significant is that $E_{I_{inside}} > E_{I_{outside}}$ for the entirety of the run. Because the flux-tube regions are selected based solely on the ψ field, the fact that $E_{I_{inside}}$ is greater than $E_{I_{outside}}$ is further corroboration that the KAW fluctuations are trending together. Whether the field under consideration is B or n, a quasi-circular structure in one is likely to correspond with a quasi-circular structure in the other. The selection routine based on X and O point bounding iso-contours tends to select regions that have larger-than-background energy densities in the fields of interest, B and n.

Shown in figure 4.18 are the ratios $E_{inside}/E_{outside}$ for magnetic, internal, and kinetic energy densities. The figure indicates that for the majority of the time values, the magnetic and internal energy density ratios are as large as 1.3, and are consistently above 1. For the simulation shown, the magnetic energy density is initially a factor of 2 greater outside the structures as compared to inside. They equilibrate in a few Alfvén times, after which $E_{B_{inside}} > E_{B_{outside}}$

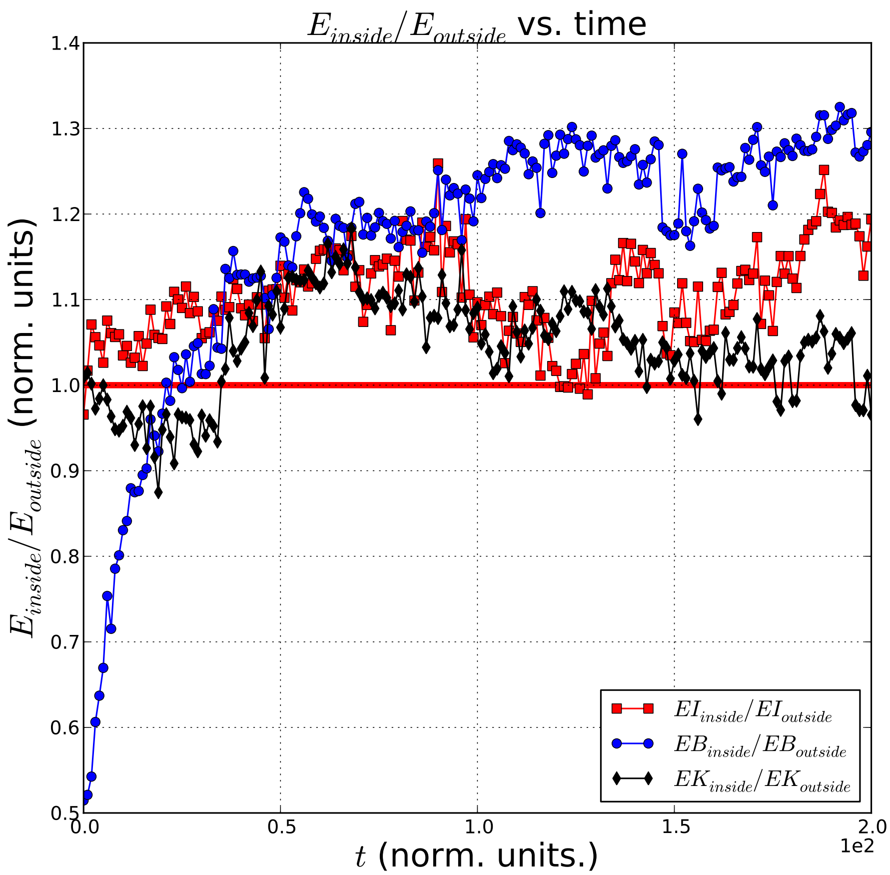

Figure 4.18: Ratio of $E_{inside}/E_{outside}$ for internal, magnetic, and kinetic energies vs. time. After an initial correlation stage, $E_{B_{inside}}$ and $E_{I_{inside}}$ are up to a factor of 1.3 times their corresponding $E_{outside}$ energy densities.

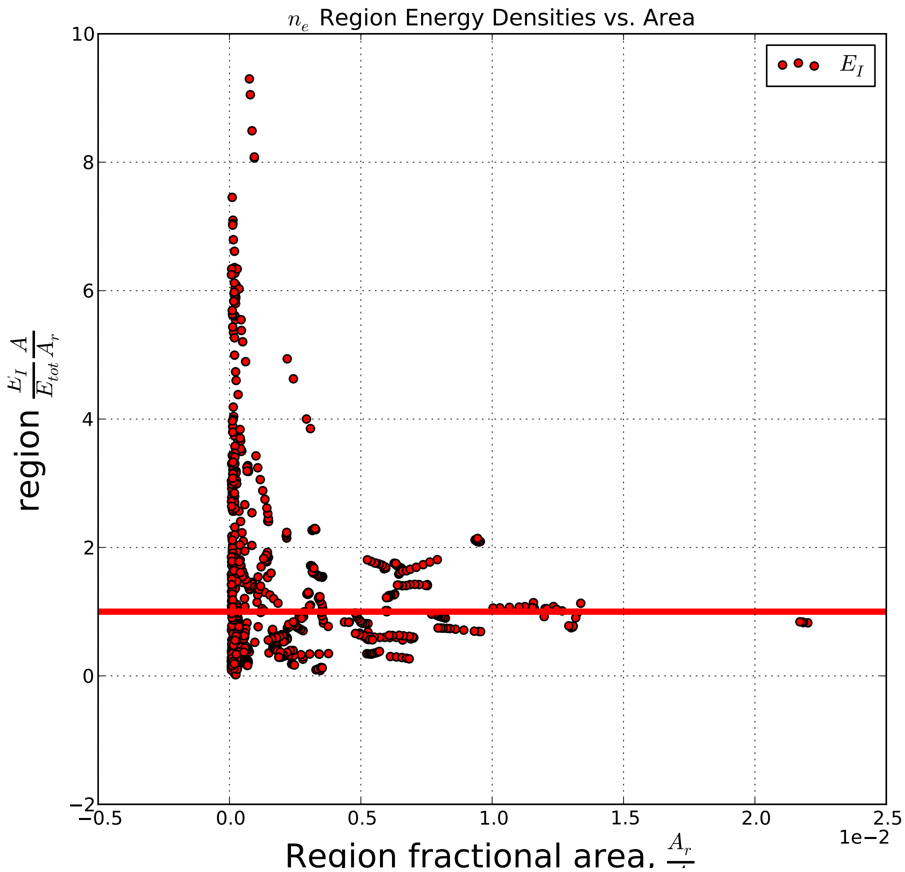

Figure 4.19: Internal energy density of flux tube vs. flux-tube area. For reference, the red line indicates the background internal energy density. The largest variance is for small flux tubes; larger flux tubes have energy densities near the background level.

for the remainder of the run shown.

Structure Energy Densities vs. Area

To determine which structures contain the largest share of enhanced energy density, we show in figures 4.19 and 4.20 the internal and magnetic energy densities for individual flux tubes vs. the flux-tube area. For internal energy, the

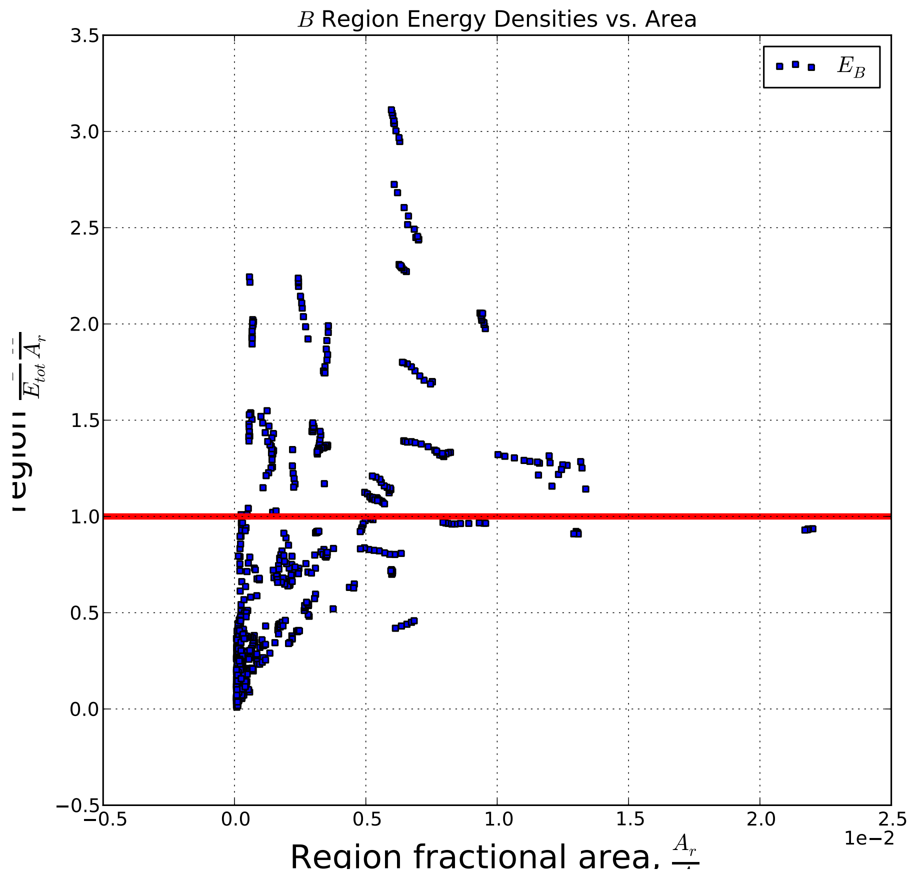

Figure 4.20: Magnetic energy density of flux tubes vs. flux-tube area. For reference, the red line indicates the background magnetic energy density. Unlike the internal energy density, the largest magnetic energy density exists in flux tubes with intermediate values for the flux-tube area.

largest energy densities belong to small-sized flux tubes. For magnetic energy, the largest energy densities are found at intermediate-sized flux tubes. The discrepancy—large internal energy density values for small flux tubes, large magnetic energy density for intermediate flux tubes—is consistent with the density-averaging process that takes place during mergers. Larger structures become larger as a result of mergers, and mergers occur only between like-signed current filaments and like-handed magnetic field orientations; thus larger B structures would be expected to have a larger share of energy density. The density fluctuations associated with the flux tubes before mergers may be of either sign; the density fluctuation associated with the merged structure results from the averaging of the initial density fluctuations. The averaging in density suppresses the internal energy density for larger structures relative to the internal energy density in smaller structures, consistent with figure 4.19.

Nonlinearity Amplitudes vs. Time, Inside and Outside

The nonlinearities in all fields—ψ, n, and $\nabla_\perp^2 \phi$—for an ideal circularly-symmetric structure are identically zero. As evident in figure 4.6, the flux-tube regions of all sizes are not circularly symmetric. The larger regions have a circularly symmetric core with an asymmetric buffer surrounding the symmetric core structure. From observations of time sequences of flux-tube regions, the structure boundaries for the largest structures evolve on a shorter timescale than do the symmetric cores of the structures. Hence, the flux-tube regions do not encapsulate only the quasi-circular structure cores, but include regions that have larger nonlinearity amplitudes in the buffer regions. A measure of the total nonlinearity amplitudes in flux-tube regions will conflate the minimal core values with the nonzero edges.

Shown in figure 4.21 are the integrated nonlinearity density amplitudes for

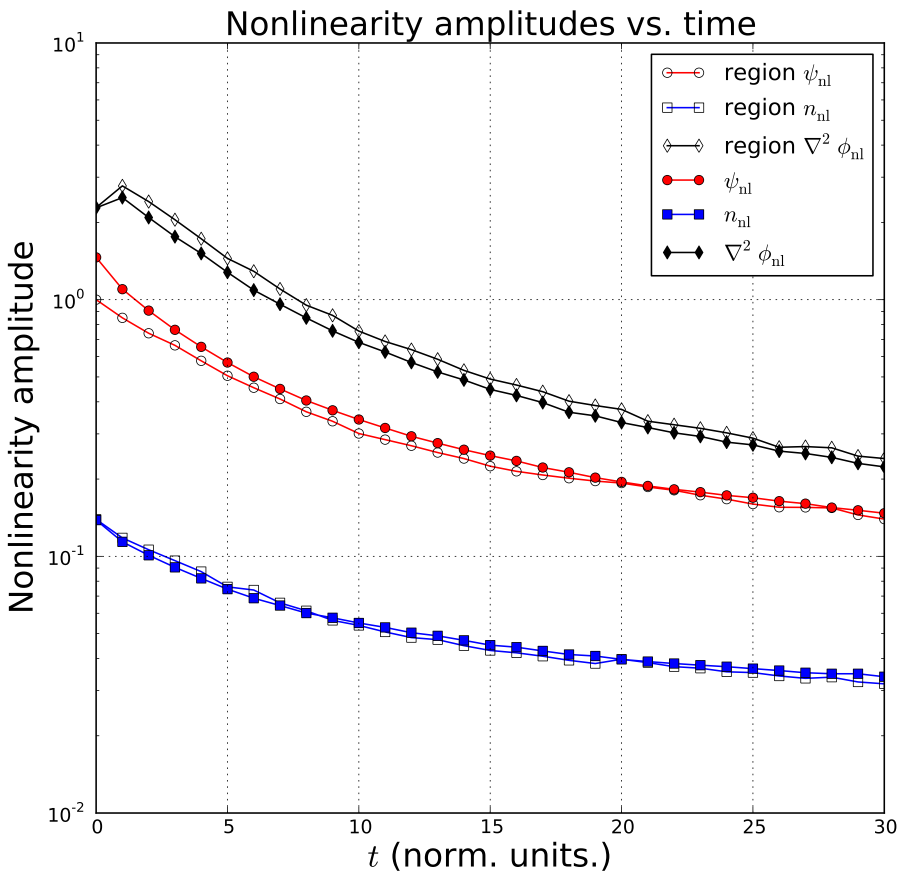

Figure 4.21: Nonlinearity areal density vs. time for each nonlinearity in Eqns. (2.9)–(2.11). The nonlinearity density amplitude inside the flux-tube regions is initially suppressed for the ψ nonlinearities. The flux-tube regions have suppressed nonlinearity amplitudes, even in the initialized state of the simulation.

both inside and outside flux-tube regions. The nonlinearity density amplitudes are defined, for the nonlinearities in Eqns. (2.9)–(2.11), as

$$\begin{aligned} \psi_{nl} &= \int_{\Omega_{in}} \mathrm{d}\mathbf{x}\, (\alpha\nabla_{\parallel} n - \nabla_{\parallel}\phi)^2 / A_{in} \\ \nabla_{\perp}^2 \phi_{nl} &= \int_{\Omega_{in}} \mathrm{d}\mathbf{x}\, (\nabla\phi \times \hat{z} \cdot \nabla\nabla_{\perp}^2 \phi - \nabla_{\parallel} J)^2 / A_{in} \\ n_{nl} &= \int_{\Omega_{in}} \mathrm{d}\mathbf{x}\, (\nabla\phi \times \hat{z} \cdot \nabla n - \nabla_{\parallel} J)^2 / A_{in} \end{aligned} \tag{4.5}$$

where Ω_{in} restricts the integration domain to regions inside selected flux tubes, and $A_{in} = \int_{\Omega_{in}} \mathrm{d}\mathbf{x}$, the total area of the flux-tube regions.

In figure 4.21, the nonlinearity density amplitude inside the flux-tube regions is initially suppressed for the ψ nonlinearities. This suppression holds for the initial, randomized state of the system. Evidently the flux tubes select regions with small ψ nonlinearity densities in comparison to the background, and these regions are identifiable from the ψ field in an initially randomized state. The nonlinearities in n and $\nabla_{\perp}\phi$ show no significant suppression inside flux-tube regions in relation to the background. The ψ nonlinearity inside flux tubes equilibrates with the background values after initial stages; both the inside and outside regions see nonlinearity amplitudes decay with time.

Only two nonlinearities in Eqns. (2.9)–(2.11) distinguish the KAW from the shear Alfvén wave, these being $\alpha\nabla_{\parallel} n$ in Ohm's Law, and $\nabla_{\parallel} J$ in the density continuity equation. The nonlinearity density amplitudes for $\alpha\nabla_{\parallel} n$ and $\nabla_{\parallel} J$ are shown in figure 4.22, and are separated into *inside* and *outside* components. In both the $\nabla_{\parallel} J$ and $\alpha\nabla_{\parallel} n$ nonlinearities, the *inside* regions have suppressed nonlinearity densities. Also noteworthy is the rapid decline in $\alpha\nabla_{\parallel} n$ in comparison to $\nabla_{\parallel} J$. From an initially randomized state, the KAW system quickly evolves so as to minimize $\alpha\nabla_{\parallel} n$. The discrepancy between *inside* and *outside* flux-tube regions is apparent, again, from the initial state.

What the nonlinearity densities demonstrate is that for flux-tube regions, the nonlinearities are diminished relative to the background. The flux-tube

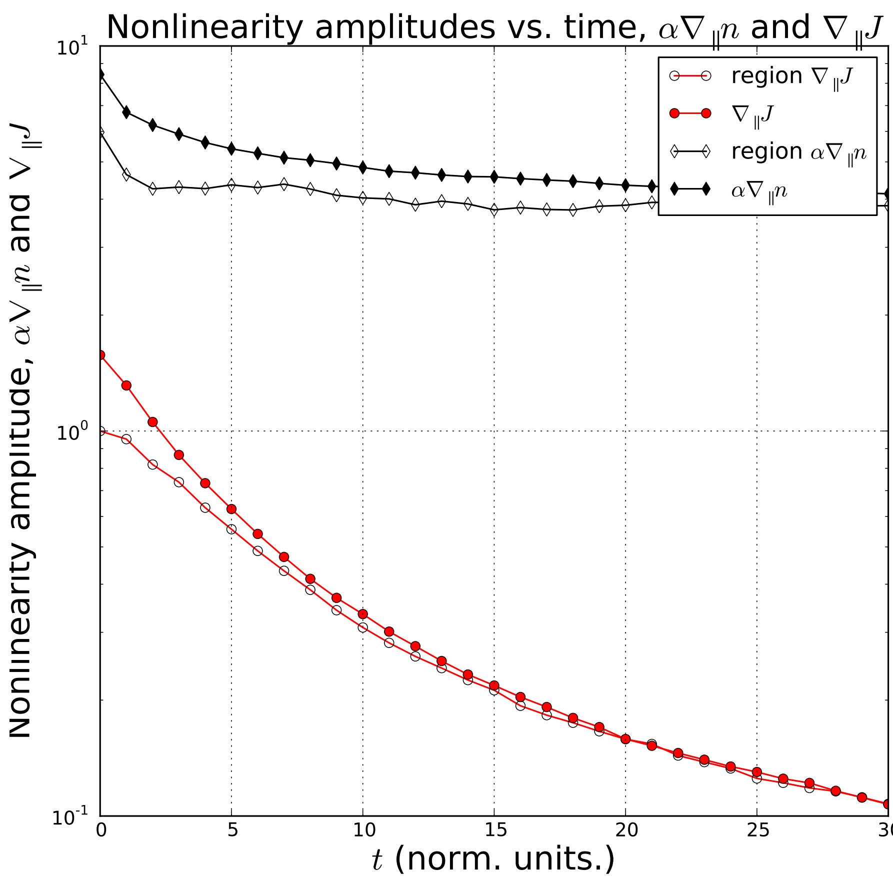

Figure 4.22: Nonlinearity areal density vs. time for the nonlinearities specific to the KAW mode. In the initial stages both the $\alpha\nabla_{\|}n$ and $\nabla_{\|}J$ nonlinearities inside the flux-tube regions are suppressed in comparison to outside. The inside and outside amplitudes equilibrate for later times, as shown.

regions, particularly the circularly symmetric core regions of large flux tubes, are privileged in relation to the regions outside the flux tubes, and are allowed to evolve on a longer timescale. The difference in KAW nonlinearity densities, $\alpha\nabla_{\parallel}n$ and $\nabla_{\parallel}J$, demonstrate that the flux-tube regions evolve on a longer timescale.

4.7 $\nabla\psi$ and ∇n Alignment Inside and Outside of Structures

In a circularly symmetric structure with no radial shear, phase fronts of KAWs form radial spokes, and $\mathbf{B}$ and ∇n are perpendicular to each other. The gradient in ψ, which is perpendicular to $\mathbf{B}$, will be parallel or anti-parallel to ∇n in coherent structures. Measurement of the alignment angle between $\nabla\psi$ and ∇n is another way to quantify the extent of the coherence of a structure. The alignment angle measure generalizes beyond purely circularly symmetric structures. A structure with non-circular distortion will demonstrate a high degree of alignment between $\nabla\psi$ and ∇n. For example, the coherent structures in figs. 4.8 and 4.9 have elliptical distortion in the separatrix, but these modes have $\nabla\psi$ parallel or anti-parallel to ∇n for the core of the structure. This alignment is expected so long as the structure is coherent, and is one manifestation of that coherence.

We plot in figure 4.23 the alignment angle θ between $\nabla\psi$ and ∇n. The four histograms capture different time periods in the evolution of the system. Initially, the histograms for inside and outside flux-tube regions are flat, as shown in the upper left plot. This is to be contrasted with the lower right figure, which is the alignment for later times. Here, the alignment for inside and outside flux tubes has peaks at $\theta = 0$ and $\theta = \pi$, indicating parallel and anti-parallel alignment between $\nabla\psi$ and ∇n. The alignment inside flux tubes is enhanced.

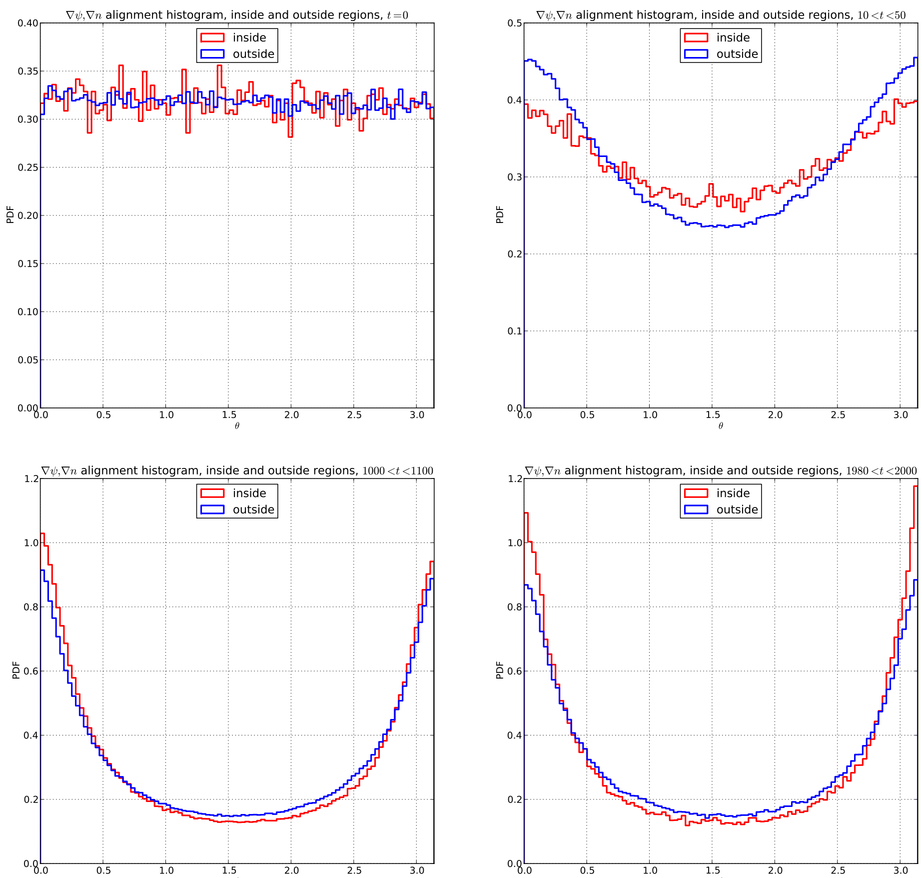

Figure 4.23: Histograms of θ, the alignment angle between $\nabla\psi$ and ∇n for inside (red) and outside (blue) flux-tube regions, and for four time values. The upper left is at time $t = 0$; upper right $10 < t < 50$; lower left $1000 < t < 1100$; lower right $1980 < t < 2000$.

The upper right histogram, the alignment for the initial stages of the simulation, indicate that the background has a greater degree of alignment than coherent structures. By the time of the lower left plot, the coherent structures have greater alignment than the background, and this relation continues. The reduced rate of alignment inside flux tubes suggests that coherent structures align on a longer timescale, but nevertheless have a greater degree of alignment than the background. This longer timescale is seen also in the suppressed nonlinearity densities, and is consistent with the two-timescale hypothesis that treats the coherent structures on a longer timescale than background turbulence.

To better demonstrate the alignment within flux tubes over time, figure 4.24 shows $\zeta_{\psi n}$ vs. time, where $\zeta_{\psi n}$ is defined as

$$\zeta_{\psi n} = \frac{4}{\pi} \left\langle \left| \theta_{\psi n} - \frac{\pi}{2} \right| \right\rangle - 1, \tag{4.6}$$

with $\theta_{\psi n}$ the angle between $\nabla\psi$ and ∇n. Here, $\zeta_{\psi n}$ ranges from $-1 < \zeta_{\psi n} < 1$. A $\zeta_{\psi n}$ value near zero indicates no overall alignment; $\zeta_{\psi n}$ values near -1 indicate overall perpendicular alignment, and ζ_{ψ_n} values near 1 indicate overall parallel or anti-parallel alignment.

In figure 4.24, both regions inside and outside flux tubes begin with no net alignment, with $\zeta_{\psi n} = 0$. As the simulation evolves in time, both regions inside and outside have a sharp rise in alignment, and the outside region initially has a greater degree of alignment, consistent with the histograms in figure 4.23. Around a normalized time of $t \sim 25$, the alignment within flux-tube regions overtakes the alignment outside flux-tube regions, and the flux tubes retain greater alignment from that point onwards. The rate of alignment decreases for greater time values, with alignment inside the flux-tube regions approaching an apparent asymptote of 0.6; outside the asymptote is 0.5.

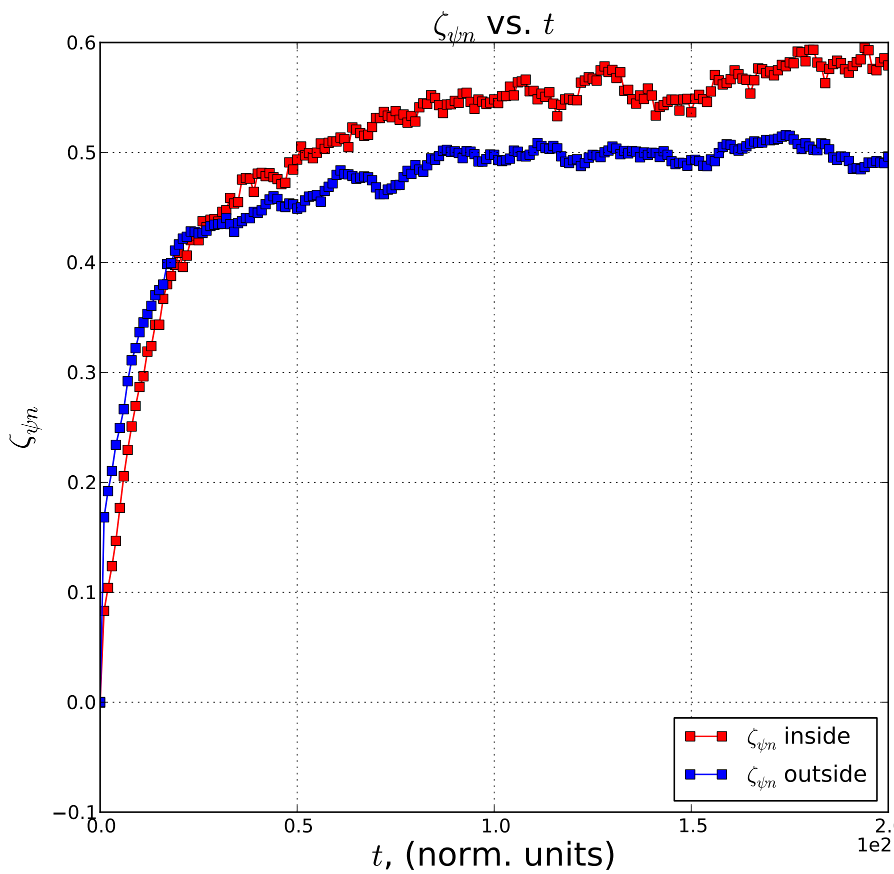

Figure 4.24: Plot of $\zeta_{\psi n}$ vs. time for inside (red) and outside (blue) flux-tube regions. The $\zeta_{\psi n}$ value of zero at $t = 0$ indicates no overall alignment inside or outside flux-tube regions. As time progresses, alignment between $\nabla\psi$ and ∇n increases, with $\zeta_{\psi n}$ approaching an asymptote of 0.6 for inside flux-tube regions, and approaching 0.5 for outside flux-tube regions.

4.8 Structure Core Values in Time

The theory of coherent structures posits that structure cores are relatively quiescent regions, undisturbed by the surrounding turbulence. So long as a structure does not interact with another like-signed structure of sufficient amplitude, it will sustain itself when interacting with background turbulence. Consequently, the ψ, n, and J value at the O point of each structure is expected to be slowly varying in time.

Figure 4.25 plots the ψ value at the O point for every flux tube versus time in a typical simulation. To reduce visual clutter, only structures that last for more than 20 time units are shown. The relative variation in ψ is at most a few percent of the average ψ value for any given structure. The cores of structures are seen to be quiescent and undisturbed.

Plotted in figure 4.26 are the n values at O points versus time. To reduce visual clutter, structures that last for more than 40 time units are shown. (A threshold of 20, used in figure 4.25, did not sufficiently reduce visual noise.) As in figure 4.25, the density core values for many structures are fairly constant, exhibiting relative fluctuations on the order of 10%. The density core values exhibit more relative variation in each structure core than do the ψ core values. This increased variation can be attributed to a number of factors:

- For one, the time frame under consideration is the initial stages of a simulation, where the structures are still forming, so greater variability in the initial stages is expected.
- The values shown are the approximate O points on the grid, so some small degree of variability can be attributed to interpolation errors.
- Third, the algorithm used to track structures from one time frame to the next has a small error rate, which contributes to the fluctuation levels.

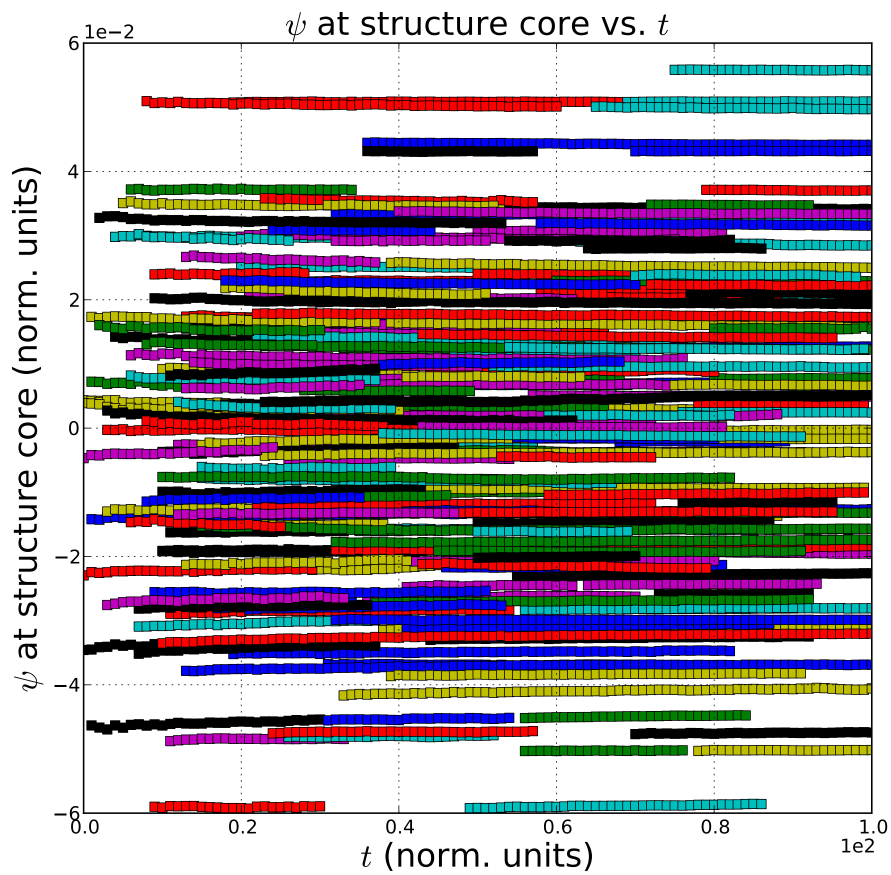

Figure 4.25: ψ field at structure O points vs. time. A structure tracking algorithm tracks structures between time steps, and each O-point time trace is identified in a different color. Notable are the 1% to 3% relative fluctuations in ψ values, indicating that the core of coherent quasi-circular structures are quiescent and preserved from background turbulence. To reduce clutter, traces that last fewer than 20 time steps are not shown.

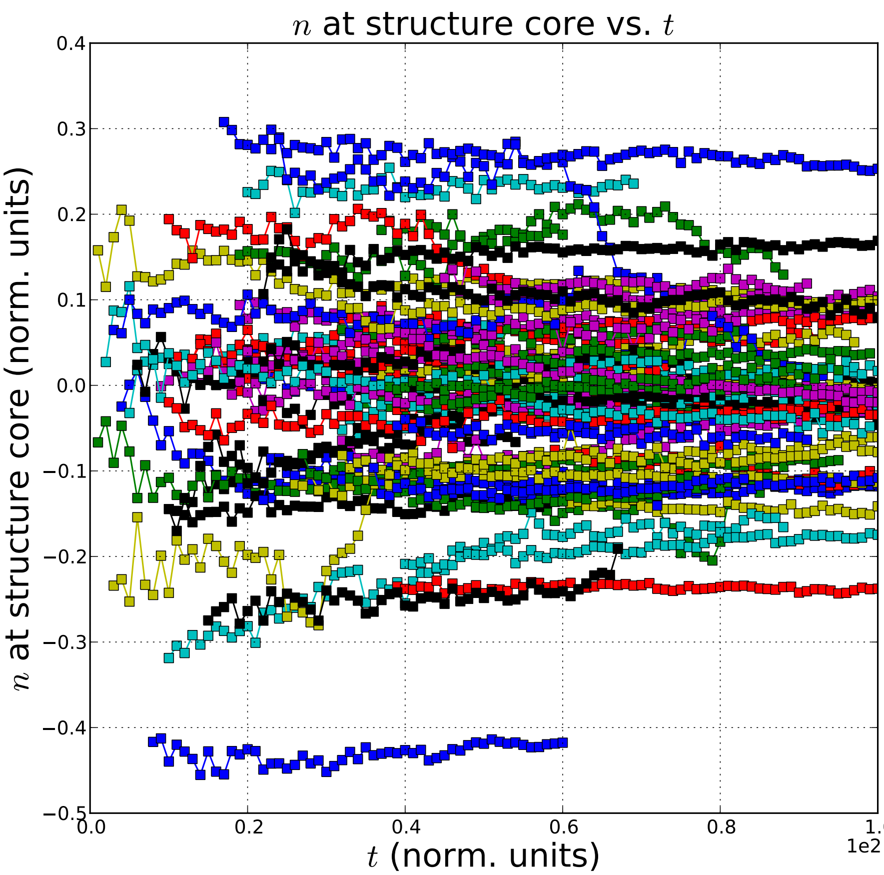

Figure 4.26: n field at structure O points vs. time. The n O-point values have fluctuations of about 5% to 10%, particularly for time values $t \lesssim 20$. This is during the initial phase correlation stage of the simulation, when coherent structures are forming. For later times, the density values at O points are quiescent, consistent with the ψ values at O points as shown in figure 4.25. To reduce clutter, traces that last fewer than 40 time steps are not shown.

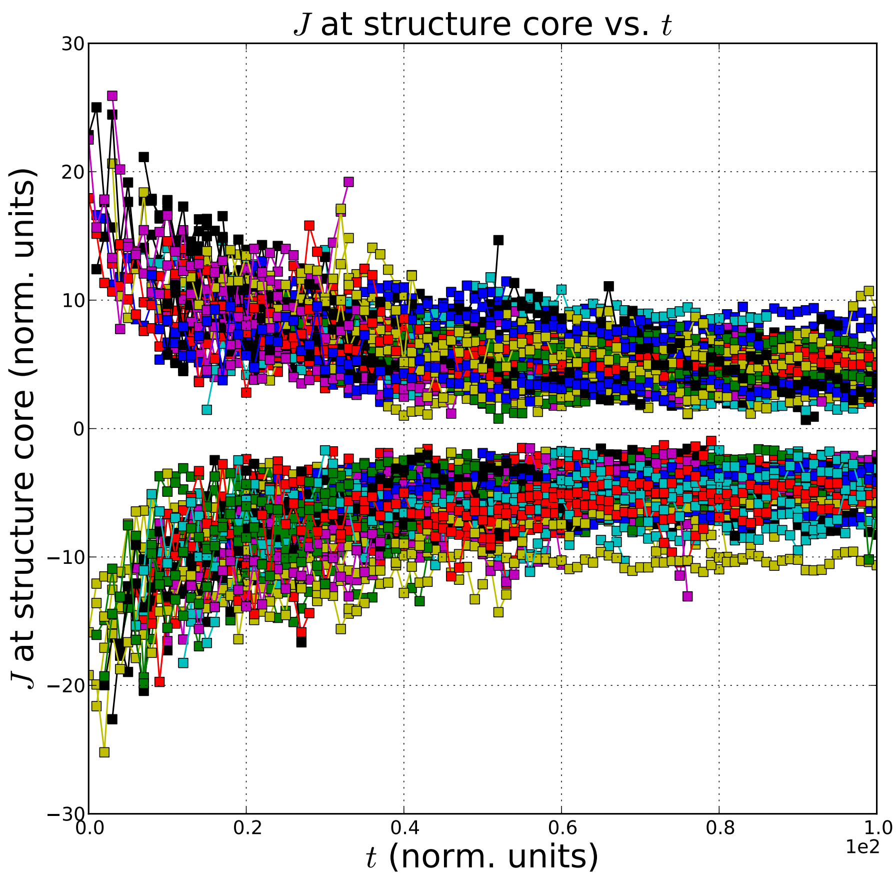

Figure 4.27: J field at structure O points vs. time. The J O-point values have fluctuations of about 10% to 15%, particularly for early time values. To reduce clutter, traces that last fewer than 20 time steps are not shown. There is an absence of O points with absolute J values less than some threshold; the threshold decreases in time and asymptotes. This suggests there is an absolute minimum J value at structure cores, below which no structure can form or persist.

> The tracking algorithm has an especially difficult time in regions with a high density of O points. Despite these fluctuations, regions of quiescent density cores are evident.

The theory proposes a current threshold at the structure core, below which a coherent structure cannot sustain sufficient radial shear in B_θ to preserve itself in the midst of turbulence. Figure 4.27 plots the J core value at a structure O point versus time, with structures less than 20 time units in longevity omitted. The core current absolute values are consistently greater than $\sim 2-3$ for all time values shown, suggesting that there is, indeed, a core current threshold below which coherent quasi-circular structures are not found. For $t = 0$, the threshold is greater, around $J \sim 10$ in normalized units for this instance of a simulation. The threshold value of $J \sim 10$ is an approximate threshold value below which coherent structures will not form from randomized initial conditions.

4.9 Discussion and Summary

The analysis presented in this chapter serves to demonstrate several significant features of flux-tube regions, which we summarize here:

Structure significance relative to background: Flux-tube regions contain a greater fraction of the total energy of the system than can be attributed to the area they occupy. This total increase in energy density is as much as 1.3 times the background for magnetic energy, and nearly 1.2 times as much for internal energy. In spite of the increase in energy levels, these regions evolve on a longer timescale.

Longer evolution timescale: Flux-tube regions evolve on a longer timescale than the background. Nonlinearity densities inside flux-tube regions are suppressed, indicating a decrease in nonlinearity evolution inside these regions. The rate of increase in alignment between $\nabla\psi$ and ∇n is smaller than the same rate for the background, indicating again that the flux tube regions evolve on a longer timescale.

Structures have greater degree of alignment: The parallel or anti-parallel alignment inside flux-tube regions is greater than for the background, a signature of the coherence of the flux-tube regions.

Derivative fields within structures have smaller radii than integral fields: The characteristic radii for derivative fields of structures, $\langle r_J \rangle$ and $\langle r_{\nabla n} \rangle$, are generally smaller than for $\langle r_B \rangle$ and $\langle r_n \rangle$, respectively, as indicated by the trend lines.

Density field less localized than B, $\langle r_n \rangle$ scales with $\langle r_B \rangle$: The characteristic radii for B and n scale linearly, suggesting that density structures and magnetic field structures align. Further, the observation that $\langle r_n \rangle$ is generally greater than $\langle r_B \rangle$ suggests that density structures are less localized than their corresponding magnetic field structure, which is in turn less localized than $\langle r_J \rangle$.

Wide variety of structure shapes within core regions: Detailed analysis of individual structures reveals a variety of structure shapes—circular, elliptically distorted—and non-monotonic variations in n and ∇n inside the cores of structures.

These characteristics support key features of the theory of coherent structures in KAW turbulence. Specifically:

- Coherent structures evolve on a longer time scale than the background.
- Inside coherent filaments, the KAW nonlinearities are suppressed in relation to the background and the coherent structures are highly aligned.
- Coherent structures are regions with a large, localized J filament at their core, and a correspondingly large B and n mantle surrounding the J

filament. The B field around the J filament is less localized than J, and the n mantle is also less localized.

- A large J filament generates a B field with larger energy density than its surroundings. The KAW equipartition between B and n suggests that the internal energy density is larger in regions associated with filaments as well.

We demonstrated in this chapter a physically-based selection process to distinguish all flux-tube regions from sheets and turbulent regions. We showed examples of four coherent structures that give a sample of the variety of structure shapes and the field relations within structures. Characteristics of the flux-tube regions were shown to correspond with key features of the theory. In summary, we claim that the cores of flux-tube regions correspond with the coherent filamentary structures described in chapter 2.

In the next chapter we investigate the global statistical properties of decaying KAW turbulence, where intermittent and non-Gaussian fluctuations are expected to contribute strongly to the scattering of radio frequency pulsar signals in the interstellar medium.

5 GLOBAL STATISTICS OF DECAYING KAW TURBULENCE

In chapter 4, the focus was on the analysis of localized flux tubes that have a well-defined boundary, and it was established that quasi-circular structures are contained within flux-tube regions. Further, quasi-circular structures were shown to have qualities that suggest they may strongly influence the statistics of KAW fields of interest, and may yield non-Gaussian pulsar signal broadening.

Pulsar scintillation is not, of course, biased towards any type of structure. It is possible that large-scale and large-amplitude sheet-like structures strongly influence pulsar scintillation. Fluctuations that influence pulsar scintillation may be found at significantly larger length scales than ρ_s. For example, a scintillation model was proposed by Boldyrev and Königl (2006), whereby pulsar signals are refracted by the compressed density shells of supernova remnants. This process occurs at larger scales than small-scale KAW turbulence. The non-Gaussian fluctuations under current consideration are an alternate pathway to yield anomalous scintillation scaling.

We investigate in this chapter the means by which non-Gaussian electron density gradients may arise in small-scale KAW turbulence under varying damping parameters. First, simulations of density structures with r^{-1} and r^{-2} mantles are presented, and are shown to yield non-Gaussian statistics. This suggests a connection between the non-localized circular structures studied in chapter 4 and the non-Gaussian statistics predicted in chapter 2. Numerical solutions of the two-field KAW system, [1] Eqns. (2.15)—(2.16), are shown to yield non-Gaussian statistics for the cases of correlated and uncorrelated initial conditions, and under variations in damping parameters, η and μ. Also, non-Gaussian statistics in ∇n are shown to be robust to variations in the damping

[1] The two-field study in this chapter is based on a study that used a two-field code. The code used in chapter 4 is a full three-field code. The results in this chapter for these values of α are consistent with the results in chapter 4 for values of α near 1.

parameters. For specific regimes of damping parameter space, the KAW system evolves such that elongated, non-localized density gradient sheets are strongly favored over coherent, localized flux-tube structures. Regardless, non-Gaussian statistics still result.

In the KAW system used here, the (unnormalized) resistivity takes the form $\eta = m_e \nu_e / ne^2$ and the density diffusion coefficient is $\mu = \rho_e^2 \nu_e$, where m_e is the electron mass, ν_e is the electron collision frequency, n is the electron density, e is the electron charge, and $\rho_e = v_{Te}/\omega_{ce}$, with v_{Te} the electron thermal velocity, and ω_{ce} the electron gyrofrequency. The ratio of these terms, $c^2\eta/4\pi\mu = 2/\beta$, where $\beta = 8\pi nkT/B^2$ and is the ratio of plasma to magnetic pressures. When we vary this ratio, we have in mind that we are representing regions of different β. However, as a practical matter in the numerical solutions, we must vary the damping parameters independently of the variation of β, since the kinetic Alfvén wave dynamics require a small β to propagate. For the warm ionized medium, typical parameters are $T_e = 8000$ K, $n = 0.08$ cm^{-3}, $|B| = 1.4$ μG, $\delta B = 5.0$ μG (Ferrière, 2001). With these parameters, the plasma β formally ranges from $0.05 - 1.2$, spanning a range of plasma magnetization.

5.1 Simulated r^{-1} and r^{-2} Density Structure PDFs

The quasi-circular structures described in chapter 2 and studied in chapter 4 are expected to generate non-Gaussian PDFs. To isolate the effect of these structures on density and density gradient PDFs from the effect of sheets and turbulence, we generated random ensembles of circularly symmetric structures with either an r^{-1} or an r^{-2} mantle outside of the structure core. PDFs for the ensembles were generated, and are shown in figures 5.1 and 5.2. Figure 5.1 is the PDF for an ensemble of structures with r^{-1} mantles outside the structure cores. Two scenarios are shown: one with a packing fraction of 64 structures per

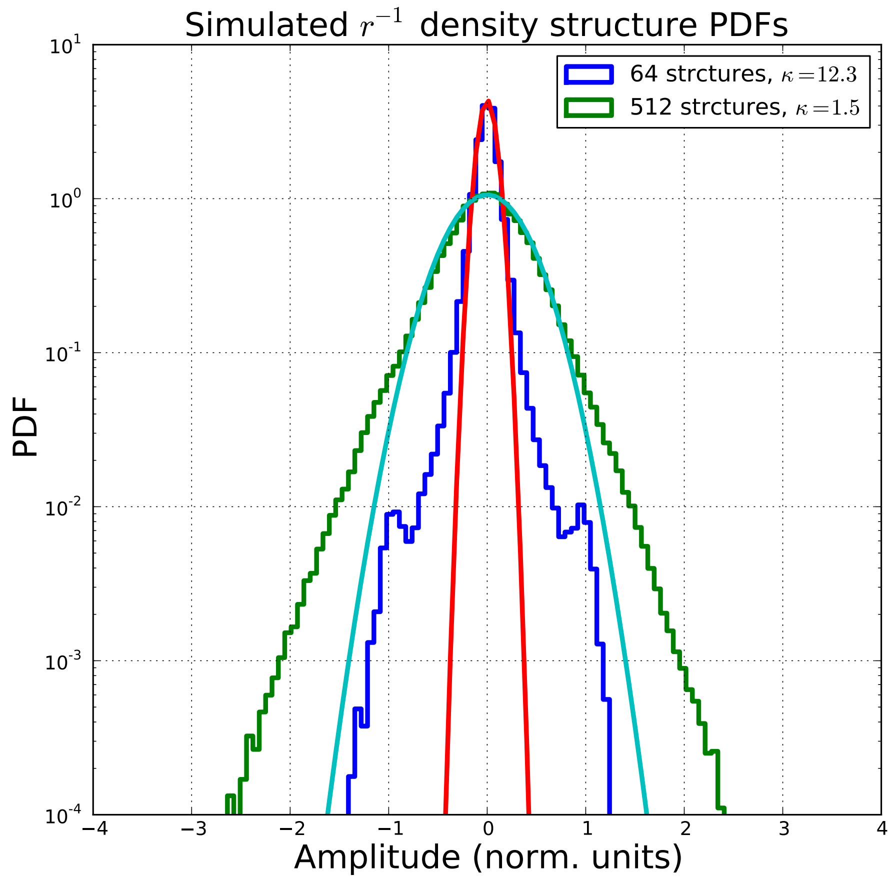

Figure 5.1: PDFs of ensembles of circular structures like the one shown in figure 2.5 with r^{-1} mantles and varying packing fractions: 64 per unit area and 512 per unit area. Best-fit Gaussian PDFs are shown. In both packing fraction cases, the kurtosis excess indicates non-Gaussian statistics, with enhanced tails.

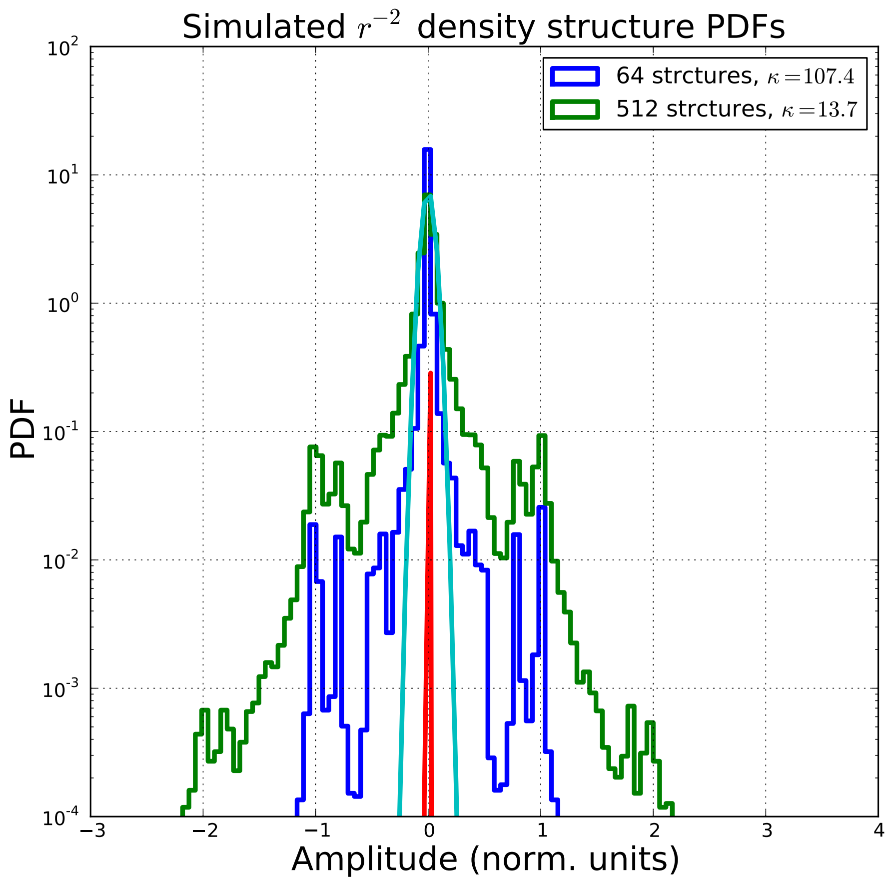

Figure 5.2: PDFs of ensembles of circular structures like the one shown in figure 2.5 with r^{-2} mantles. The radial exponent of -2 serves as a proxy for the density gradient field. Packing fractions of 64 per unit area and 512 per unit area are shown. Best-fit Gaussian PDFs are shown. The kurtosis excess is consistently an order of magnitude larger than for the r^{-1} mantle structures.

unit area, the other with 512 structures per unit area. The PDFs and Gaussian best fits are plotted. Both packing fractions demonstrate clear non-Gaussian tails, with the smaller packing fraction being more non-Gaussian, as measured by kurtosis excess. The kurtosis excess for the 64 structures per unit area is $\kappa = 12.3$; for 512 structures per unit area, $\kappa = 1.5$, both indicating enhanced tails relative to a best-fit Gaussian. As the structure areal density increases above 512 per unit area, the kurtosis excess asymptotes to zero.

For a density structure with an r^{-1} mantle, its gradient has a mantle with an r^{-2} dependence. Shown in figure 5.2 are the PDFs for an ensemble of structures with an r^{-2} mantle. The r^{-2} mantle structure ensemble serves as a proxy for the gradient of density structures with an r^{-1} mantle, as proposed in chapter 2. It also demonstrates the effect of greater structure localization on the PDFs of the density field. The only difference between the PDFs in figures 5.1 and 5.2 are the radial exponents of the mantles. For the r^{-2} structures, the PDFs are significantly broadened relative to a Gaussian best-fit. The PDF tails have larger fluctuations, owing to the greater degree of localization of the r^{-2} structures relative to their less-localized r^{-1} cousins. The kurtosis excesses for the r^{-2} structure ensemble are an order of magnitude larger than the r^{-1} structure ensemble. In every way the density gradient field is expected to have enhanced non-Gaussian statistics relative to the density fields. Further, these ensemble PDFs suggest that the non-localized density and density gradient fields associated with circular KAW structures are sufficient to yield strongly non-Gaussian statistics.

The results in this section consider only the effect of circular structures on the PDF of a density field. They ignore the effect that turbulence and sheets have on the density PDF. We expect that turbulence—residing between circular structures—makes the PDFs more nearly Gaussian in comparison to

PDFs generated from the circular structures alone. Sheets, like coherent quasi-circular structures, are capable of generating structures with extended mantles, and may contribute to the non-Gaussian statistics of the system. The interplay between all three components and how they affect the global PDFs of the KAW system is not obvious.

To account for these effects, we must investigate the PDFs of the physical KAW system. In addressing the statistics of the physical KAW system, we also need to address the question of whether the initial phase relation between the n and ψ fields has a dominant effect on the non-Gaussian statistics; this is discussed in the next section.

5.2 Effect of Initial Phase Correlation on Statistics

It is of interest to examine whether cross-correlated or uncorrelated initial conditions affect the statistics of the fields of interest. Two representative numerical solutions are presented here that reveal the KAW system's tendency to form spatially-correlated structures in electron density and current regardless of initial phase correlations. This study establishes the robustness of density structure formation in KAW turbulence and lends confidence that such structures should exist in the ISM under varying circumstances. The first numerical solution has cross-correlated initial conditions between the n and ψ fields; the second, uncorrelated. Damping parameters η and μ are equal and large enough to ensure numerical stability while preserving structures in density, current, and magnetic fields. These examples also serve to explore the intermediate η/μ regime.

The energy vs. time histories for both numerical solutions are given in figures 5.3 and 5.4. Total energy is a monotonically decreasing function of time. The magnetic and internal energies remain in overall equipartition throughout

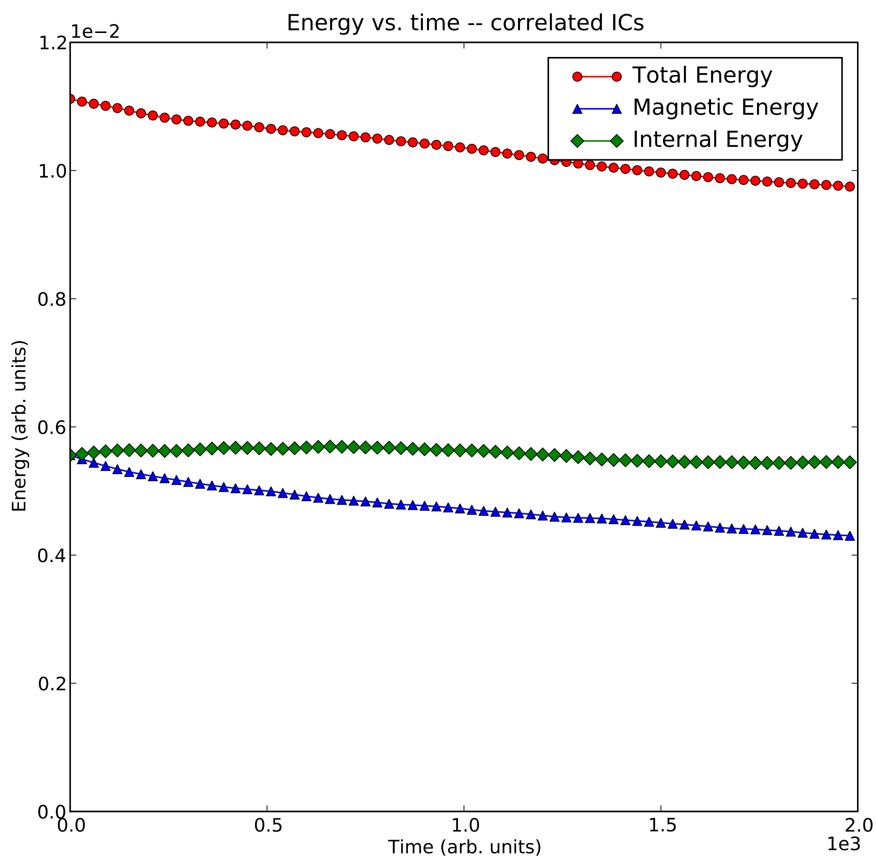

Figure 5.3: Energy vs. time for cross-correlated initial conditions. Total energy is monotonically decreasing with time, and magnetic and internal energies remain in rough equipartition.

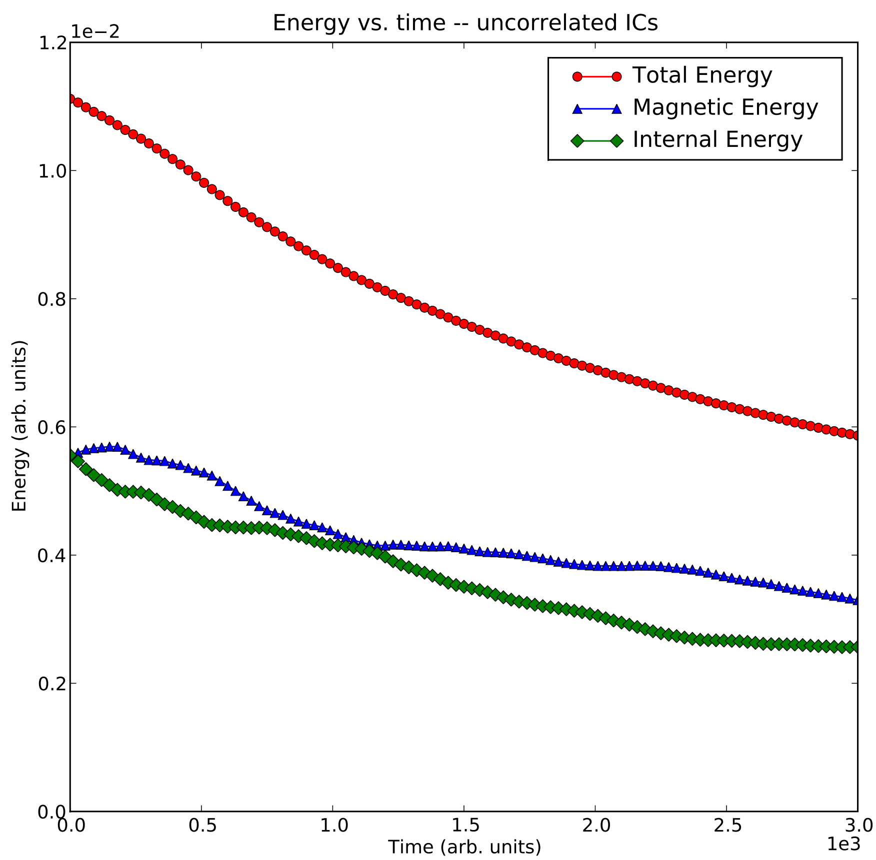

Figure 5.4: Energy vs. time for uncorrelated initial conditions. Total energy is monotonically decreasing with time, and magnetic and internal energies remain in rough equipartition.

the numerical solutions. Magnetic energy increases at the expense of internal energy and *vice versa*. This energy interchange is consistent with KAW dynamics and overall energy conservation in the absence of resistive or diffusive terms. The exchange is crucial in routinely producing large amplitude density fluctuations in this two-field model of nonlinearly interacting KAWs.

The total energy decay rates for the uncorrelated and correlated initial conditions in figures 5.4 and 5.3 differ, with the latter decaying more strongly than the former. The damping parameters are identical for the two numerical solutions, and the decay-rate difference remains under varying randomization seeds. The magnitudes of the nonlinear terms during the span of a numerical solution in Eqns. (2.9) and (2.11) for uncorrelated initial conditions are consistently larger than those of correlated initial conditions by a factor of 5. This difference lasts until 2500 Alfvén times, after which the decay rates are roughly equal in magnitude. The steeper energy decay during the run of numerical solutions with uncorrelated initial conditions (figure 5.4) suggests that the enhancement of the uncorrelated nonlinearities transports energy to higher k (smaller scale) more readily than the nonlinearities in the correlated case. Relatively more energy in higher k enhances the energy decay rate as the linear damping terms dissipate more energy from the system. The initial configuration, whether correlated or uncorrelated, is seen to have an effect on the long-term energy evolution for these decaying numerical solutions. It will be shown below, however, that the correlation does not significantly affect the statistics of the resulting fields.

For cross-correlated initial conditions, we expect there to be a strong spatial relation between current, magnetic field, and density structures through time. Figures 5.5 and 5.6 show the n and $|\mathrm{B}|$ contours at various times. For the latest time contour, the spatial structure alignment is evident. Further, in figure 5.7, the circular magnetic field structures (magnetic field direction and intensity

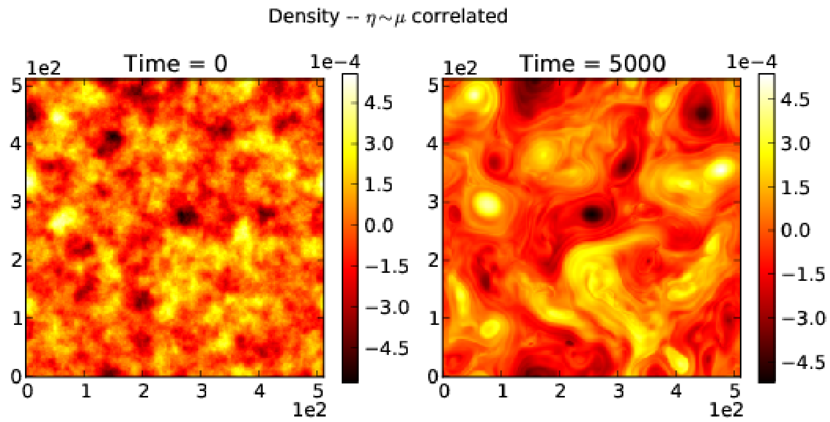

Figure 5.5: Contours of n for various times in a numerical solution with correlated initial conditions.

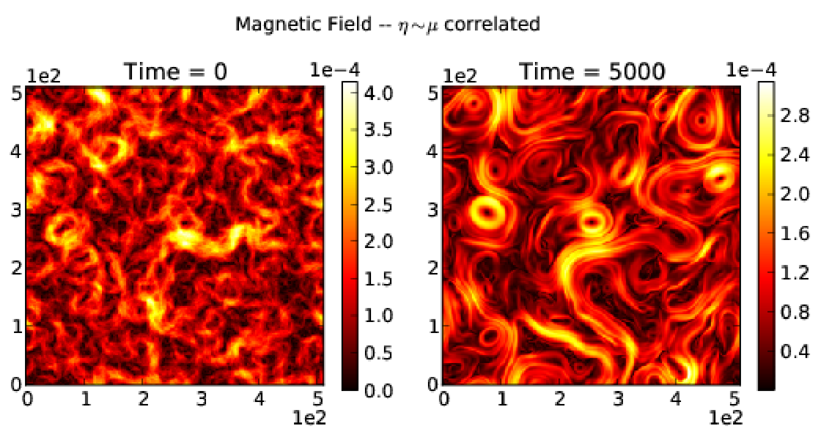

Figure 5.6: Contours of $|\mathrm{B}|$ for various times in a numerical solution with correlated initial conditions.

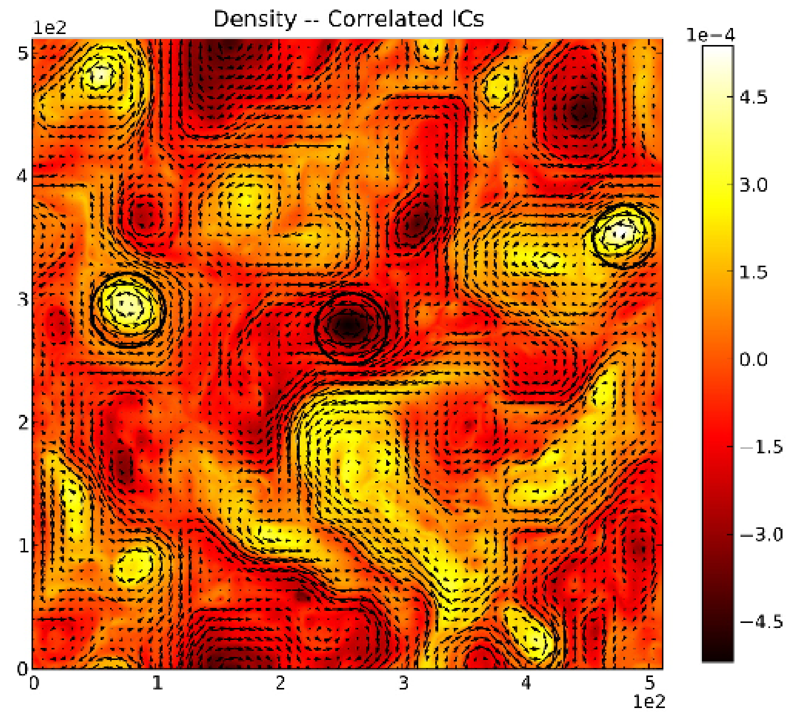

Figure 5.7: Contour plot of n with $\mathbf{B}$ vectors overlaid. The positive, circularly-symmetric density structures correspond to counterclockwise-directed $\mathbf{B}$ structures; the opposite holds for negative circularly-symmetric density structures. These spatial correlations are to be expected for correlated initial conditions.

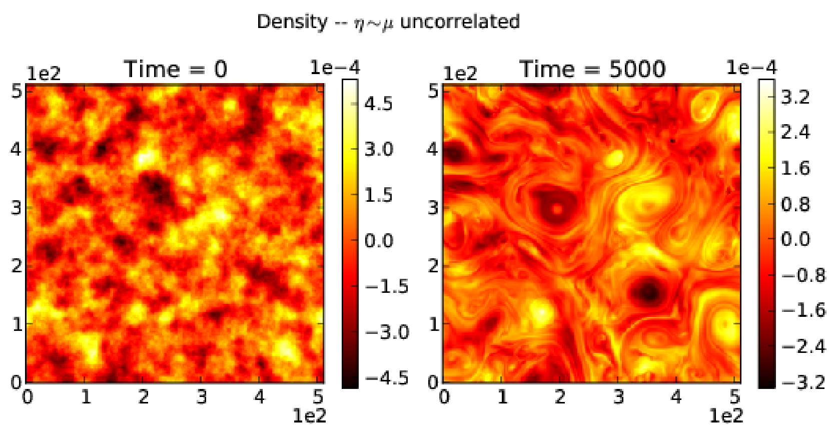

Figure 5.8: Contours of n for various times in a numerical solution with uncorrelated initial conditions.

indicated by arrow overlays) align with the large-amplitude density fluctuations. The correlation is evident once one notices that every positive-valued circular n structure corresponds to counterclockwise-oriented magnetic field, and *vice versa*. Figure 5.7 is at a normalized time of 5000 Alfvén times, defined in terms of the large B_0. The system preserves the spatial structure correlation indefinitely, even after structure mergers.

The second representative numerical solution is one with uncorrelated initial conditions. Contour plots of density and $|B|$ are given in figures 5.8 and 5.9, respectively. It is noteworthy that, similar to the cross-correlated initial conditions, spatially correlated density and magnetic field structures are discernible at the latest time contour.

In figure 5.10 the circular density structures correspond to circular magnetic structures. Unlike figure 5.7 the positive density structures may correspond to clockwise or counterclockwise directed magnetic field structures. This serves to illustrate that, although the initial conditions have no phase relation between fields, after many Alfvén times circular density structures spatially correlate

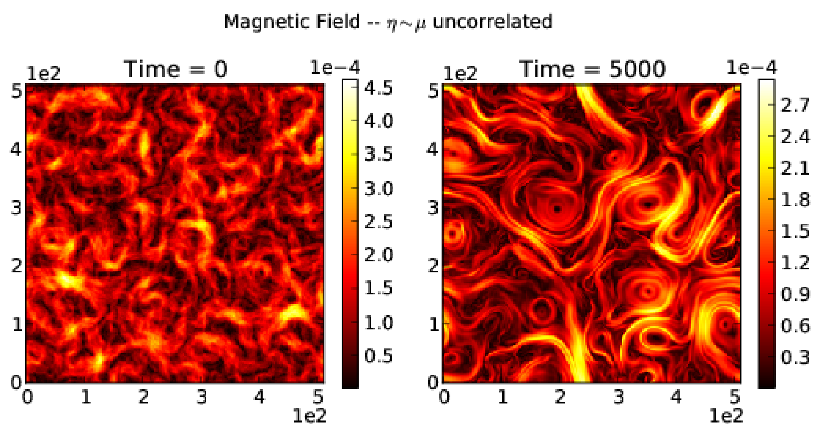

Figure 5.9: Contours of $|\mathrm{B}|$ for various times in a numerical solution with uncorrelated initial conditions.

with magnetic field structures and persist for later times.

The kurtosis excess as a function of time, defined as $K(\xi) = \left\langle \xi^4 \right\rangle / \sigma_\xi^4 - 3$, is shown in figures 5.11 and 5.12 for correlated and uncorrelated initial conditions, respectively. Positive K indicates a greater fraction of the distribution is in the tails as compared to a best-fit Gaussian. These figures indicate that the non-Gaussian statistics for the fields of interest are independent of initial correlation in the fields. In particular, the density gradients, $|\nabla n|$, are significantly non-Gaussian as compared to the current. Because scintillation is tied to density gradients, this situation is expected to favor the scaling inferred from pulsar signals.

The tendency of density structures to align with magnetic field structures regardless of initial conditions indicates that the initial conditions are representative of fully-developed turbulence. After a small number of Alfvén times the memory of the initial state is removed as the KAW interaction sets up a consistent phase relation between the fluctuations in the magnetic and density fields. The theory in chapter 2 presented a mechanism whereby these spatially

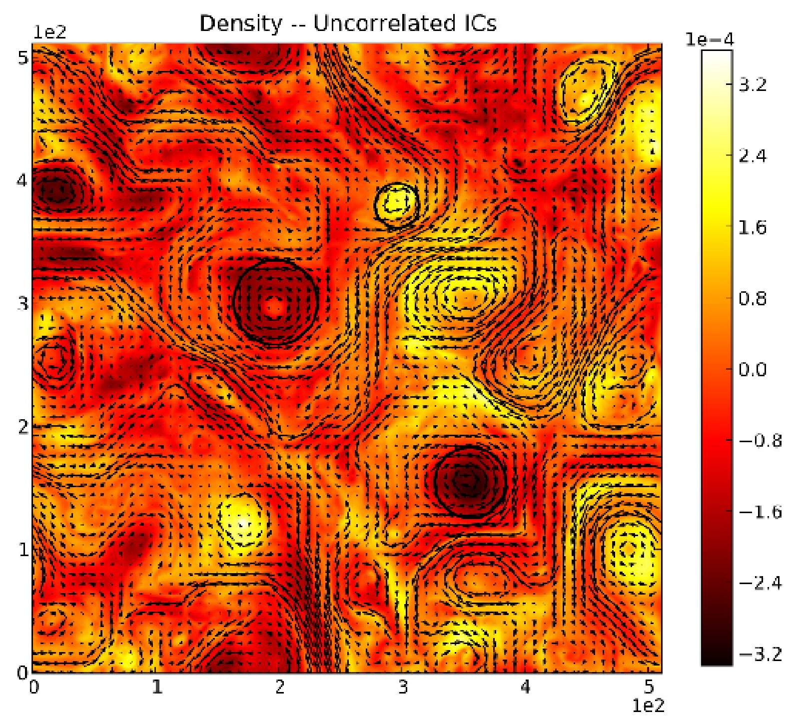

Figure 5.10: Contour plot of n with $\mathbf{B}$ vectors overlaid for a numerical solution with initially uncorrelated initial conditions. The positive, circularly-symmetric density structures correspond to magnetic field structures, although the sense (clockwise or counterclockwise) of the magnetic field structure does not correlate with the sign of the density structures. Circled in black are symmetric structures that display a high degree of spatial correlation. The circle gives an approximate indication of the separatrix for the structure.

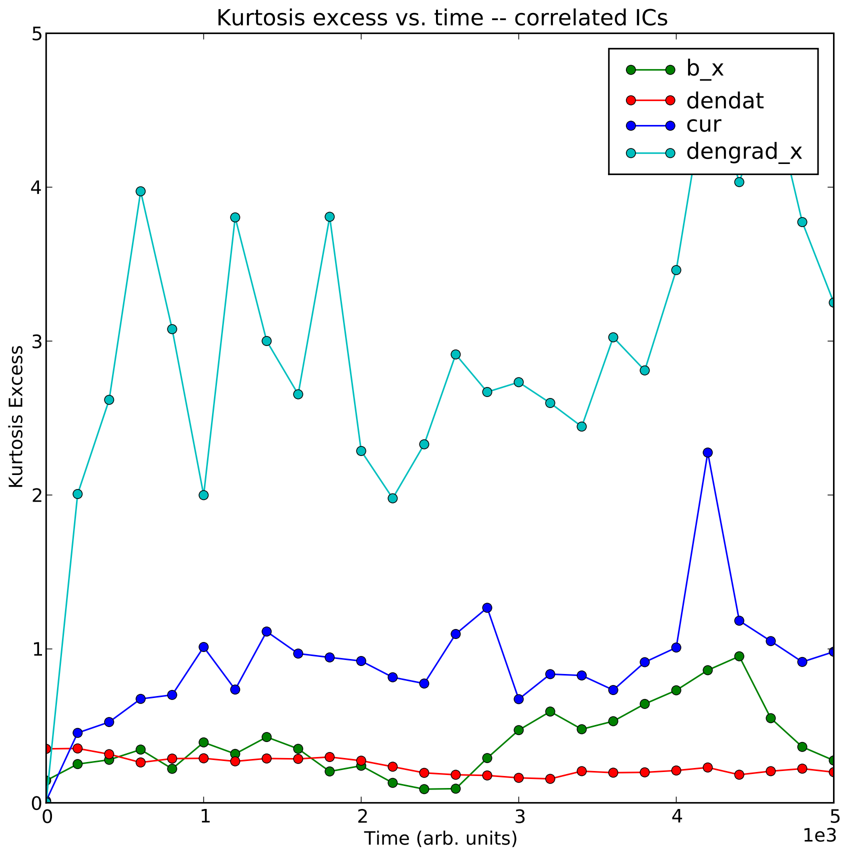

Figure 5.11: Kurtosis excess for a numerical solution with phase-correlated initial conditions and $\eta/\mu = 1$.

correlated structures can be preserved via shear in the periphery of the structures. Figures 5.11 and 5.12 indicate that this mechanism is in play even in cases where the initial phase relations are uncorrelated.

The preceding results were for a damping regime where $\eta/\mu \sim 1$, an intermediate regime. Numerical solutions that explore the regime $\mu/\eta \to 0$ with η small is the opposite regime used in Craddock et al. (1991), which used $\eta = 0$ and μ large enough to preserve numerical stability. In the $\mu \to 0$ regime, circularly symmetric current and magnetic structures are not as prevalent; instead,

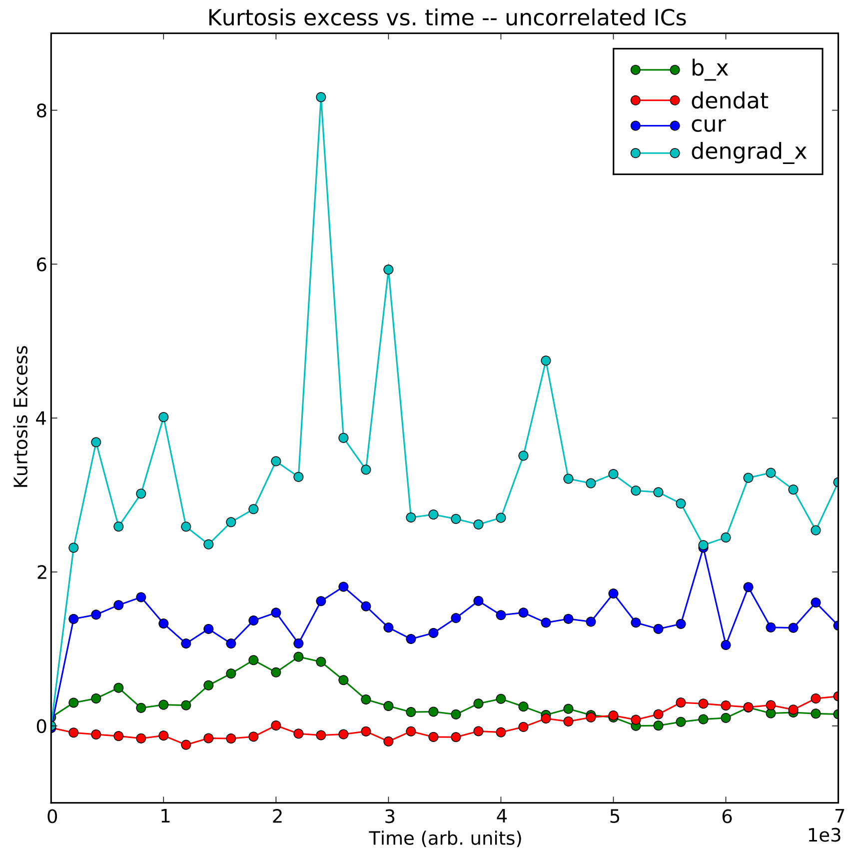

Figure 5.12: Kurtosis excess for a numerical solution with phase-uncorrelated initial conditions and $\eta/\mu = 1$.

sheet-like structures dominate the large amplitude fluctuations. Current and magnetic field gradients are strongly damped, and the characteristic length scales in these fields are larger.

Contours of density for a numerical solution with $\mu = 0$ are shown in figure 5.13. Visual comparison with contours for runs with smaller damping parameters (figure 5.8, where $\eta = \mu$) indicate a preponderance of sheets in the $\mu = 0$ case, at the expense of circularly-symmetric structures as seen above. All damping is in η; any current filament that would otherwise form is unable to

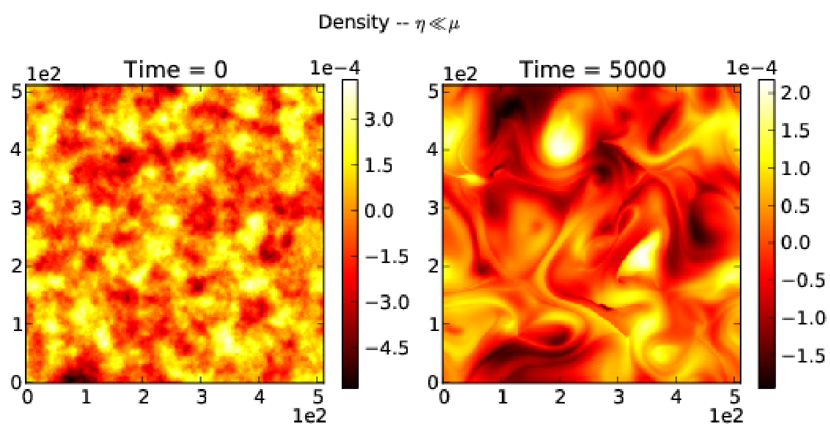

Figure 5.13: Electron density contour visualization with diffusive damping parameter $\mu = 0$ for various times.

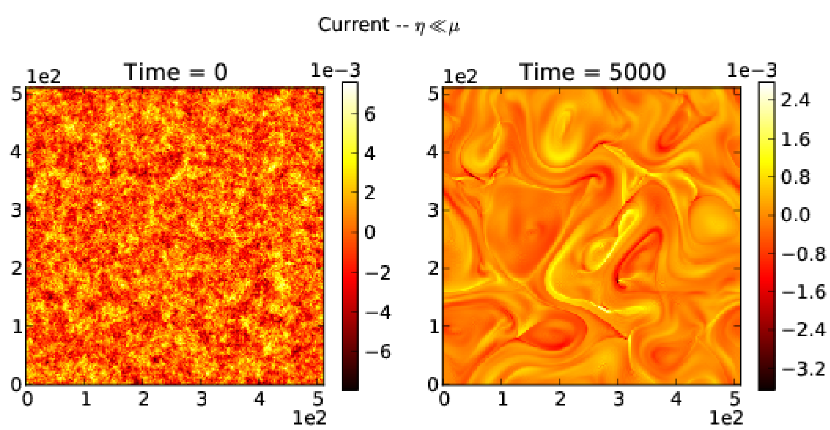

Figure 5.14: Current density contour visualization with diffusive damping parameter $\mu = 0$ for various times.

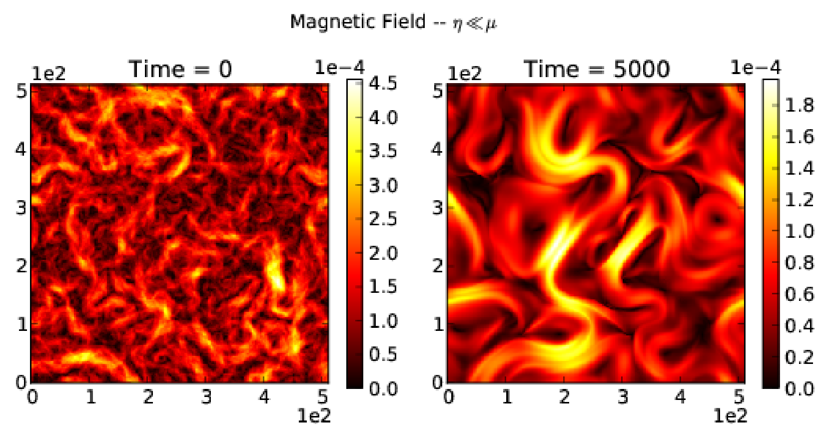

Figure 5.15: Magnitude of magnetic field contour visualization with diffusive damping parameter $\mu = 0$ for various times.

preserve its small-scale, large amplitude characteristics before being resistively damped. Inspection of the current and $|B|$ contours for the same numerical solution [figures 5.14 and 5.15] reveal broader profiles and relatively few circular current and magnetic field structures with a well-defined separatrix as in the small η case. Since there is no diffusive damping, gradients in electron density are able to persist, and electron density structures generally follow the same structures in the current and magnetic fields.

Kurtosis excess measurements for the $\mu = 0$ numerical solutions yield mean values consistent with the $\eta = \mu$ numerical solutions, as seen in figure 5.16. Magnetic field strength and electron density statistics are predominantly Gaussian, with current statistics and density gradient statistics each non-Gaussian. Perhaps not as remarkable in this case, the density gradient kurtosis excess is again seen to be greater than the current kurtosis excess – this is anticipated since the dominant damping of density gradients is turned off. With fewer filamentary current structures, however, the mechanism proposed in chapter 2 is not likely to be at play in this case, since few large-amplitude filamentary

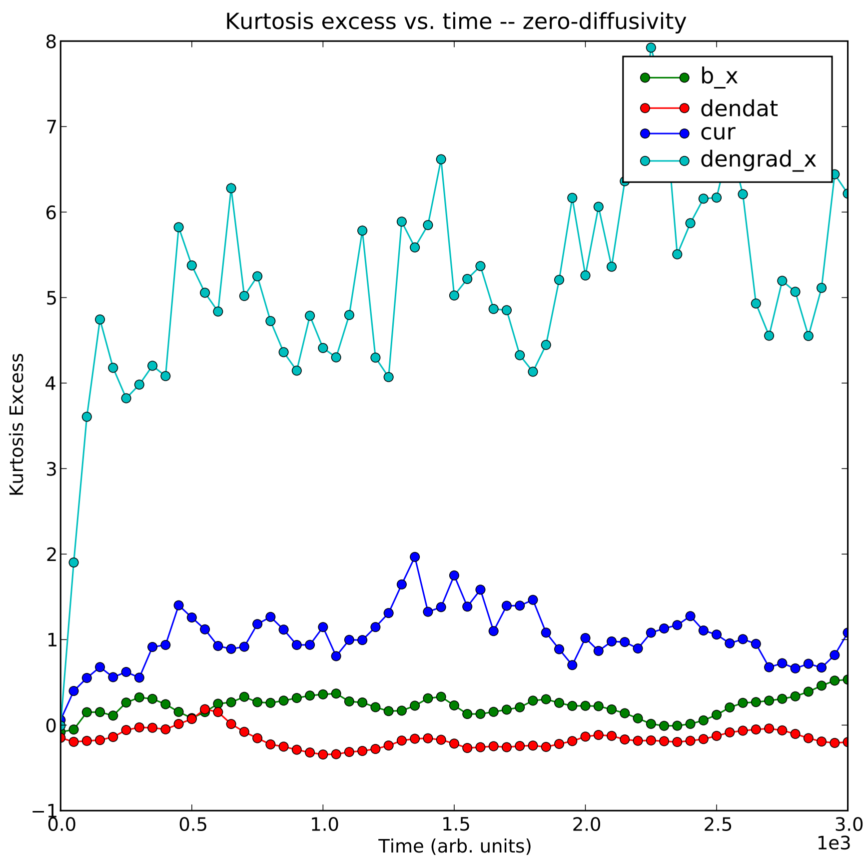

Figure 5.16: Kurtosis excess for a numerical solution with diffusive parameter $\mu = 0$. Density gradient kurtosis remains greater than current kurtosis for the duration of the numerical solution.

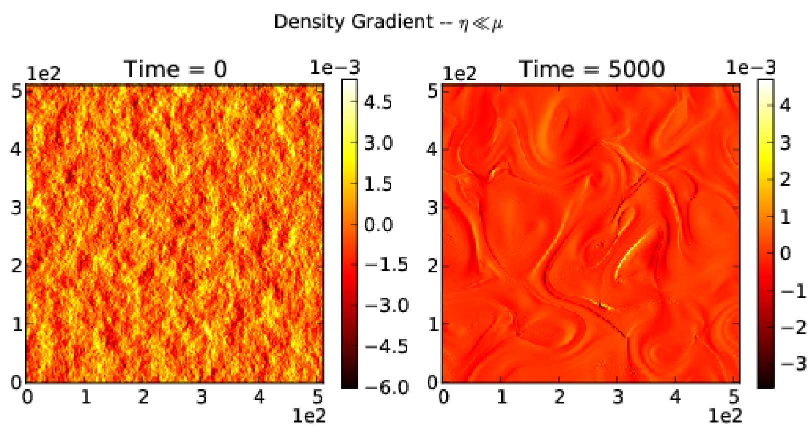

Figure 5.17: Electron density gradient (x direction) contour visualization with diffusive damping $\mu = 0$ for various times.

current structures exist. Sheets, evident in the density gradients in figure 5.17 and in the current in figure 5.14 are the dominant large-amplitude structures and determine the extent to which the density gradients have non-Gaussian statistics. The current and density sheets are well correlated spatially. The largest sheets can extend through the entire domain, and evolve on a longer timescale than the turbulence. Sheets exist at the interface between large-scale flux tubes, and are regions of large magnetic shear, giving rise to reconnection events. With η relatively large, the sheets evolve on timescales shorter than the structure persistence timescale associated with the long-lived flux tubes.

Sheets and filaments are the dominant large-amplitude, long-timescale structures that arise in the KAW system. Filaments arise and persist as long as η is small, with their amplitude and statistical influence diminished as η increases. Sheets exist in both regimes, becoming the sole large-scale structure in the large-η regime. Density gradients are consistently non-Gaussian in both regimes as long as μ is small, although the density structures are different in both regimes. Density gradient sheets arise in the large-η regime and these

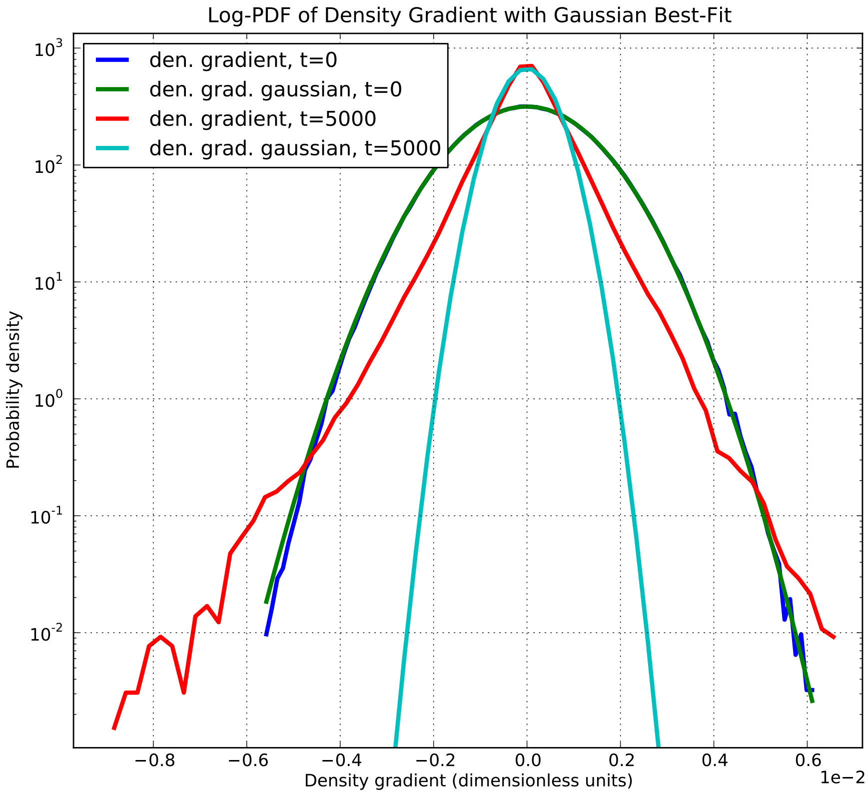

Figure 5.18: Log-PDF of density gradients for an ensemble of numerical solutions with $\eta/\mu = 1$ at $t = 0$ and $t = 5000$. The density gradient field at $t = 0$ is Gaussian distributed, while for $t = 5000$ the gradients are enhanced in the tails, and deviate from a Gaussian. A best-fit Gaussian for each PDF is plotted for comparison.

density gradient sheets are large enough to yield non-Gaussian statistics.

5.3 Ensemble Statistics and PDFs

To quantify the extent to which the decaying KAW system develops non-Gaussian statistics, ensemble runs were performed for both the $\eta/\mu \sim 1$ and $\eta/\mu \ll 1$ regimes, and PDFs of the fields were generated.

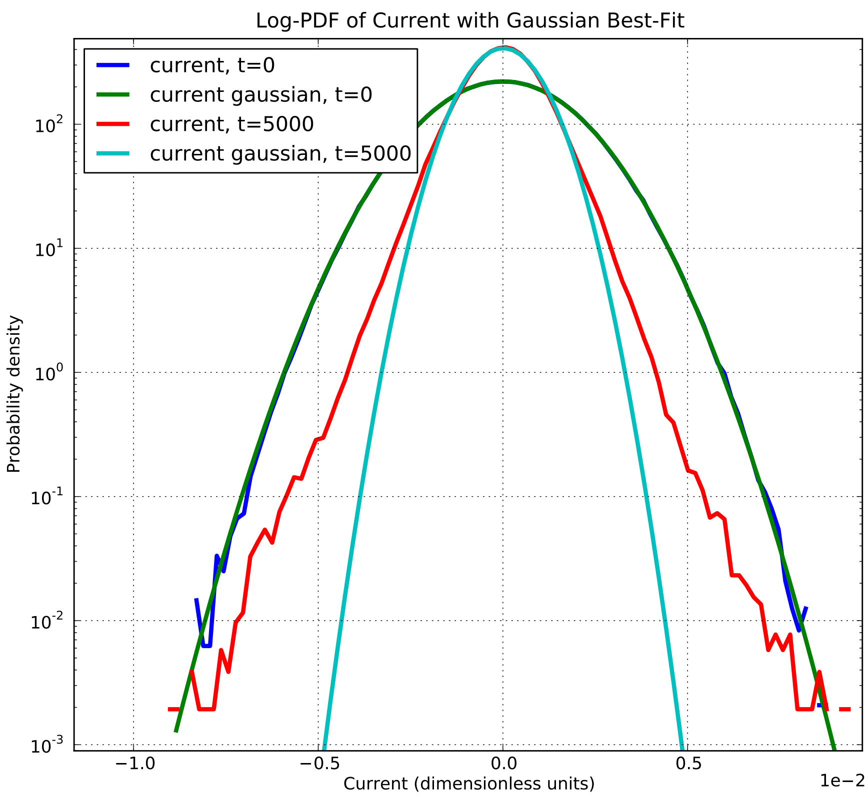

Figure 5.19: Log-PDF of current for an ensemble of numerical solutions with $\eta/\mu = 1$ at $t = 0$ and $t = 5000$. The current at $t = 0$ is Gaussian distributed. For $t = 5000$ the current is non-Gaussian. Unlike the density gradient, the current is not enhanced in the tails of the PDF for later times relative to its initial Gaussian envelope.

For the $\eta/\mu \sim 1$ regime, 10 numerical solutions were evolved with identical parameters but for different randomization seeds. In this case $\eta = \mu$ and both damping parameters have minimal values to ensure numerical stability. The fields were initially phase-uncorrelated. The density gradient ensemble PDF for two times in the solution results is shown in figure 5.18. Density gradients are Gaussian distributed initially. Many Alfvén times into the numerical solution the statistics are non-Gaussian with long tails. These PDFs are consistent with the time histories of density gradient kurtosis excess as shown above. The distribution tail extends beyond 15 standard deviations, almost 90 orders of magnitude above a Gaussian best-fit distribution. Similar behavior is seen in the current PDFs – initially Gaussian distributed tending to strongly non-Gaussian statistics with long tails for later times. Figure 5.19 is the current PDF at an advanced time into the numerical solution. It is to be noted that the density gradient PDF has longer tails at higher amplitude than does the current PDF. One would expect these to be in approximate agreement, since the underlying density and magnetic fields have comparable PDFs that remain Gaussian distributed throughout the numerical solution. The discrepancy between the density gradient and current PDFs suggests a process that enhances density derivatives above magnetic field derivatives. Future work is required to explore causes of this enhancement. This result is significant for pulsar scintillation, which is most sensitive to density gradients. Although interstellar turbulence is magnetic in nature, the KAW regime has the benefit of fluctuation equipartition between n and B. The density gradient, however, is more non-Gaussian than the magnetic component, suggesting that this type of turbulence is specially endowed to produce the type of scintillation scaling observed with pulsar signals.

Ensemble runs for the $\eta/\mu \ll 1$ regime yield distributions similar to the

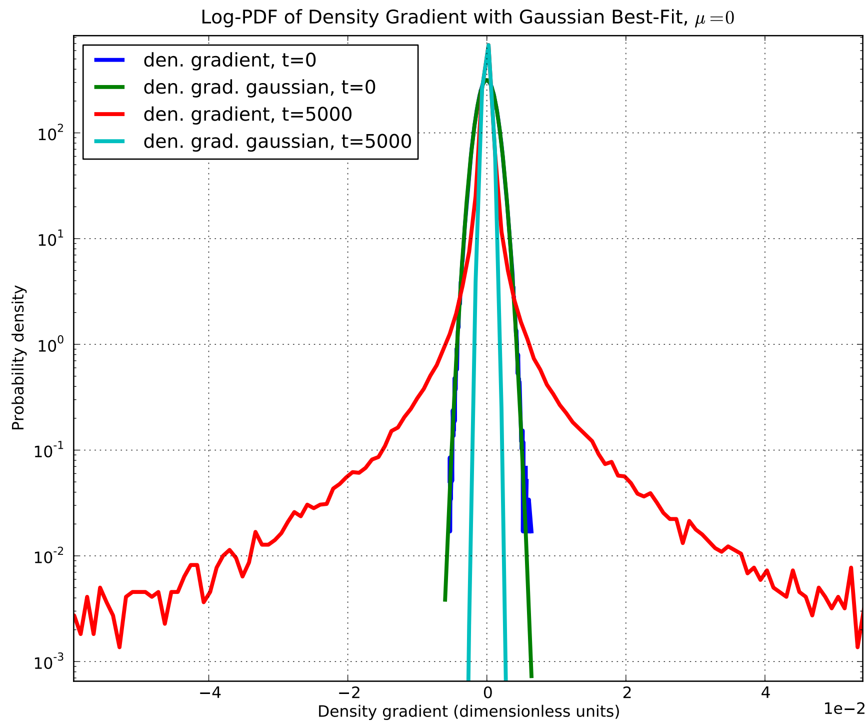

Figure 5.20: Log-PDF of density gradient for an ensemble of numerical solutions with $\mu = 0$ at $t = 0$ and $t = 5000$. The density gradient field at $t = 0$ is Gaussian distributed, while for $t = 5000$ the gradients are enhanced in the tails, and deviate from a Gaussian. A best-fit Gaussian for each PDF is plotted for comparison.

$\eta/\mu \sim 1$ regime in all fields. The ensemble PDF for two times is shown in figure 5.20. The initial density gradient PDF is Gaussian distributed. For later times long tails are evident and consistent with the kurtosis excess measurements as presented above for the $\mu = 0$ case. The density gradient distribution has longer tails at higher amplitude than the current distribution; the overall distributions are similar to those for the $\eta/\mu \sim 1$ regime, despite the absence of filamentary structures and the presence of sheets. The strongly non-Gaussian statistics are insensitive to the damping regime, provided that the diffusion coefficient is small enough to allow density gradients to persist.

5.4 Discussion

Physical damping parameter values

Using the normalizations for Eqns. (2.9)—(2.11) and using $B = 1.4\mu$G, $n = 0.08$ cm^{-3} and $T_e = 1$ eV, η_{norm}, the normalized Spitzer resistivity, is 2.4×10^{-7} and μ_{norm}, the normalized collisional diffusivity, is 1.9×10^{-7}. For a resolution of 512^2, these damping values are unable to keep the system numerically stable. The threshold for stability requires the simulation η to be greater than 5×10^{-6}, which is almost within an order of magnitude of the ISM value. The numerical solutions presented here, while motivated by the pulsar signal width scalings, more generally characterize the current and density gradient PDFs when the damping parameters are varied. We would expect the density gradients to be non-Gaussian when using parameters that correspond to the ISM.

Behavior as $t \to \infty$

The non-Gaussian distributions presented here are strongly tied to the fact that the system is decaying and that circular intermittent structures are preserved from nonlinear interaction. Once a large-amplitude structure becomes sufficiently circularly symmetric and is able to preserve itself from background turbulence via the shear mechanism, that structure is expected to persist on long timescales relative to the turbulence. Structure mergers will lead to a time-asymptotic state with two oppositely-signed current structures and no turbulence. As structures merge, kurtosis excess increases until the system reaches a final two-filament state, which would have a strongly non-Gaussian distribution and large kurtosis excess.

Corrections from driven turbulence

If the system were driven, energy input at large scales would replenish large-amplitude fluctuations. New structures would arise from large amplitude regions whenever the radial magnetic field shear was large enough to preserve the structure from interaction with turbulence. One could define a structure-replenishing rate from the driving terms that would depend on the energy injection rate and scale of injection. The non-Gaussian measures for a driven system would be characterized by a competition between the creation of new structures through the injection of energy at large scales and the annihilation of structures by mergers or by erosion from continuously replenished small-scale turbulence. If erosion effects dominate, the kurtosis excess is maintained at Gaussian values, diminishing the PDF tails relative to a Lévy distribution. If replenishing effects dominate, however, the enhancement of the tails of the density gradient PDF may be observed in a driven system as it is observed in the present decaying system. We note that structure function scaling in hydrodynamic turbulence is consistent with the replenishing effects becoming more dominant relative to erosion effects as scales become smaller, i.e., the turbulence is more intermittent at smaller scales. The large range of scales in interstellar turbulence and the conversion of MHD fluctuations to kinetic Alfvén fluctuations at small scales both support the notion that the structures of the decaying system are relevant to interstellar turbulence at the scales of KAW excitations. This scenario is consistent with arguments suggested by Harmon and Coles (2005). They propose a turbulent cascade in the solar wind that injects energy into the KAW regime, counteracting Landau damping at scales near the ion Larmor radius. By doing so they can account for enhanced small-scale density fluctuations and observed scintillation effects in interplanetary scintillation.

We also observe that, although the numerical solutions presented here are decaying in time, the decay rate decreases in absolute value for later times (figures 5.3 and 5.4), approximating a steady-state configuration as measured by energetics. The kurtosis excess (figures 5.11 and 5.12) for the density gradient field is statistically stationary after a brief startup period. Despite the decaying character of the numerical solutions, they suggest that the density gradient field would be non-Gaussian in the driven case.

Merger sheets and scintillation

The kurtosis excess—a measure of a field's spatial intermittency—is itself intermittent in time. The large spikes in kurtosis excess correspond to rare events involving the merger of two large-amplitude structures, usually filaments. A large-amplitude short-lived current sheet grows between the structures and persists throughout the merger, gaining amplitude in time until the point of merger. The kurtosis excess during this merger event is dominated by the single large-amplitude sheet between the merging structures. This would likely be the region of dominant scattering for scintillation, since a corresponding large-amplitude density gradient structure exists in this region as well. The temporal intermittency of kurtosis excess suggests that these mergers are rare and, hence, of low probability. The heuristic picture of long undeviated Lévy flights punctuated by large angular deviations could apply to these merger sheets.

5.5 Conclusions

Simulations of an ensemble of circular density structures with r^{-1} and r^{-2} mantles are shown to yield non-Gaussian PDFs with enhanced tails and large excess kurtosis values. The PDF of an isolated structure with r^{-1} or r^{-2} was shown to have non-Gaussian PDFs in chapter 2. The non-Gaussian statistics for an ensemble of structures suggest that density and density gradient structures with non-localized mantles are sufficient to yield non-Gaussian scattering structures, although the areal density of structures is shown to influence the degree of non-Gaussianity.

To understand the PDFs of the physical KAW system, decaying kinetic Alfvén wave turbulence is shown to yield non-Gaussian electron density gradients, consistent with non-Gaussian distributed density gradients inferred from pulsar width scaling with distance to source. With small resistivity, large-amplitude current filaments form spontaneously from Gaussian initial conditions, and these filaments are spatially correlated with stable electron density structures. The electron density field, while Gaussian throughout the numerical solution, has gradients that are strongly non-Gaussian. Ensemble statistics for current and density gradient fields confirm the kurtosis measurements for individual runs. Density gradient statistics, when compared to current statistics, have more enhanced tails, even though both these fields are a single derivative away from electron density and magnetic field, respectively, which are in equipartition and Gaussian distributed throughout the numerical solution.

When all damping is placed in resistive diffusion ($\eta/\mu \to 0$ regime), filamentary structures give way to sheet-like structures in current, magnetic, electron density, and density gradient fields. Kurtosis measurements remain similar to those for the small η case, and the field PDFs also remain largely unchanged, despite the different large-amplitude structures at play.

The kind of structures that emerge, whether filaments or sheets, is a function of the damping parameters. With η and μ minimal to preserve numerical stability and of comparable value, the decaying KAW system tends to form filamentary current structures with associated larger-scale magnetic and density structures, quasi-circular and long-lived. Each filament is associated with a flux tube and can be well separated from the surrounding turbulence. Sheets exist in this regime as well, and they are localized to the interface between flux tubes. With η small and $\mu = 0$, the system is in a sheet-dominated regime. Both regimes have density gradients that are non-Gaussian with large kurtosis.

The conventional picture of a Lévy flight is a random walk with step sizes distributed according to a long-tailed distribution with no defined variance. This gives rise to long, uninterrupted flights punctuated by large scattering events. This is in contrast to a normally-distributed random walk with relatively uniform step sizes and small scattering events. The intermittent filaments that arise in the small η and μ regime suggest the presence of structures that could scatter pulsar signals through large angles; however, the associated density structures are broadened in comparison to the current filament and would not give rise to as large a scattering event. Even broadened structures can yield Lévy distributed density gradients (Terry and Smith, 2007), but it is not clear how the Lévy flight picture can be applied to these broad density gradient structures. In the $\mu = 0$ regime, the large-aspect-ratio sheets may serve to provide the necessary scatterings through refraction and may map well onto the Lévy flight model.

An alternative possibility, suggested by the *temporal* intermittency of the kurtosis (itself a measure of a field's *spatial* intermittency), is the encounter between the pulsar signal and a short-lived sheet that arises during the merger of two filamentary structures. These sheets are limited in extent and have very large amplitudes. At their greatest magnitude they are the dominant structure in the numerical solution. Their temporal intermittency distinguishes them from the long-lived sheets surrounding them. It is possible that a pulsar signal would undergo large scattering when interacting with a merger sheet. This scattering would be a rare event, suggestive of a scenario that would give rise to a Lévy flight.

6 CONCLUSIONS AND FUTURE WORK

The foci of this thesis are twofold: (1) to provide a general study of the emergence and persistence of intermittent structures in decaying small-scale plasma turbulence and (2) to argue that intermittent density structures influence the non-Gaussian statistics inferred from pulsar signal broadening in the ISM.

Chapter 2 presented the theoretical framework for a nonlinear kinetic Alfvén wave model, and established that the nonlinear model captures the essential physics of kinetic Alfvén waves. Further, we argued in chapter 2 that KAWs are one means by which density fluctuations are generated at small scales, and the KAW model, simple as it is, is an appropriate approximation of the processes that generate active density fluctuations at scales near $10\rho_s$ and smaller. The nonlinear model provides for the nonlinear interaction of KAWs; of particular importance is the propagation of small-wavelength KAWs along the magnetic field of a large-scale perturbation. The nonlinear KAW model captures the nonlinear interaction between small-scale KAW turbulence and large-scale coherent structures. Presuming a time-separation *ansatz* between long time scale circular structures and short time scale, low amplitude turbulent fluctuations, it was shown that radial shear in the $\hat{\theta}$-directed magnetic field at the edge of a coherent structure can preserve the structure when immersed in a turbulent bath, if the radial shear in B_θ is large enough. The conditions for sufficient radial shear in B_θ were derived from asymptotic analysis of the two-timescale formulation of Eqns. (2.15)–(2.16).

Having established a means by which coherent structures can persist when interacting with turbulence, the PDFs of the density and density gradient for an ideal coherent structure were derived. Arguing from energy equipartition, it was presumed that the density field outside the core of a structure follows the same r^{-1} radial falloff as the magnetic field surrounding a large-amplitude current filament. Combined with the relation between area and probability density, it was shown that the density PDF scales as $P(n)\ \mathrm{d}n \propto n^{-3}\ \mathrm{d}n$ for the region outside the structure core. The density gradient for such an idealized structure was shown to have a PDF which scales as $P(n')\ \mathrm{d}n' \propto (n')^{-2}\ \mathrm{d}n'$, which follows a Lévy distribution. PDFs for the density and density gradient in a physical realization of decaying KAW turbulence were addressed in chapter 5.

Chapter 3 presented a general formalism for a straightforward numerical scheme for evolving a nonlinear PDE in time. The constraints on the PDE are that (1) the boundary conditions are periodic and (2) the coefficients of the linear terms are time-independent. These constraints are in place to allow the system to be evolved using a pseudospectral scheme and to allow the use of an integrating factor transform. The rationale for using an integrating factor is that the linear terms are able to be evolved exactly. The transformation incurs computational cost, having to compute a transcendental function of an array multiple times per time step. The cost is reduced or in some cases eliminated by the removing of the CFL stability constraints for the linear terms, and the integrating factor allows arbitrary values of parabolic damping parameters to be used in the simulation. If, as in Eqns. (2.9)—(2.11), the linear terms are diagonal, then the integrating factor transformation takes a particularly simple and efficient form, Eqn. (3.16). Particulars of the initial conditions for the three-field KAW model were then presented. Comparison with simulations of a two-field KAW model (Craddock et al., 1991) were given.

Chapter 4 was concerned with the detailed analysis of coherent localized structures in decaying KAW turbulence. It was shown that the Hessian of ψ, $H(\psi)$, has a particular signature for coherent, quasi-circular structures that quantifies the combination of a large current filament at the structure core, surrounded by an annulus of large radial B_θ shear. A structure selection procedure based on the topological features of the ψ field was then presented. This procedure allows the separation of flux tubes from the rest of the turbulent domain. It was argued that at the core of large flux tubes is a coherent structure described in chapter 2, hence, the union of all flux tubes includes the quasi-circular structures. Examples of specific flux tubes were shown, indicating the variety of forms that coherent structures take. Noteworthy features of flux-tube regions and the coherent structures they encompass are:

- The flux-tube regions have enhanced energy densities, up to 30% more, when compared to the background. The enhancement holds for both magnetic and internal energy densities.
- The structures have suppressed total nonlinearity amplitudes and, specifically, suppressed KAW nonlinearity amplitudes. This suggests that the structures evolve on a longer timescale than the background turbulence.
- The flux-tube regions have a greater degree of alignment between $\nabla\psi$ and ∇n, indicating a greater degree of coherence.
- The density field in the vicinity of a flux tube is less localized than B as indicated by the characteristic radii $\langle r_n \rangle$ and $\langle r_B \rangle$. The quantities $\langle r_n \rangle$ and $\langle r_B \rangle$ scale linearly and correlate with each other.

The above list of features of flux-tube regions correspond with the theoretical description of structures given in chapter 2.

Simulations of ensembles of ideal density structures with r^{-1} and r^{-2} mantles were presented in chapter 5. The PDFs for these ideal structures indicate that r^{-1} and r^{-2} structures are sufficient to yield strongly non-Gaussian statistics with heavy tails. Variations in the initial phase relation between ψ and n

fields were shown to change the energy evolution and n-J parity inside coherent structures, but the PDFs of density and density gradients were shown to be non-Gaussian regardless of initial phase relations.

The kurtosis excess and PDFs for simulations with varying damping parameters were then presented. Non-Gaussian density gradient and current PDFs were shown to be robust to variations in damping parameters. These findings support the central claim that intermittent structures can be found in small-scale turbulence in the ISM.

6.1 Future Work

The numerical simulation and analysis presented in this thesis have corroborated key components of the theory of coherent filamentary structures in KAW turbulence. We identify at least three areas to be addressed in future work that will generalize the conclusions presented here: simulating a driven KAW turbulence system, simulating a three-dimensional KAW turbulence system, and generalizing the model to a hybrid fluid-particle system (Yin et al., 2007).

Driven turbulence

The electron density power spectrum in the local interstellar medium follows a power law that spans many decades (Armstrong et al., 1995), an observation that is often interpreted as an inertial range in a turbulent cascade. This suggests that a turbulence model at scales near ρ_s and smaller should account for driven turbulence, if energy is indeed cascading from larger scales. The decaying turbulence system in the present work does achieve a quasi-steady state as indicated by energy evolution. (See figures 5.3 and 5.4.) Coherent structures persist in the midst of small-scale turbulence; simulations with driven turbulence can address the effect that large-scale flow shear has on structure coherence and persistence. If filamentary structure lifetimes are shortened by driven turbulence, it may be the case that sheet-like structures are favored instead, and the density gradient PDFs may still be non-Gaussian. The robustness of non-Gaussian statistics in decaying KAW turbulence lends credence to this conjecture. For more details on driven turbulence in the context of the present work, see the conclusion of chapter 5.

Three-dimensional considerations

The simulations in this work are two-dimensional, a simplification that was exploited by the flux-tube extraction procedure that is based on critical points in the two-dimensional ψ field. This assumes that gradients along the mean B field equilibrate quickly so that gradients along $\mathbf{B}_0$ are quickly smoothed. Generalizing the model to a fully three-dimensional simulation will allow coherent filamentary structures to develop variations along $\mathbf{B}_0$. The relation $k_\parallel \ll k_\perp$ still holds at scales near ρ_s for KAWs, so the fluctuation spectrum in the $\mathbf{z}$ direction will have a cutoff at smaller $k_\parallel$ than the cutoff in $k_\perp$. The present approach for filament segmentation will not work in three-dimensional turbulence, and another method to separate coherent structures from turbulence will be required.

Hybrid or fully kinetic simulation

Lastly, to more accurately capture kinetic effects for dissipation-range KAW turbulence, it is recommended to use either a fully kinetic simulation, or a hybrid particle-fluid simulation, treating the electrons as a continuous fluid and the ions as individual particles. A fully kinetic or hybrid simulation is required to capture wave-particle interactions and to fully address collisionless damping effects on structure formation and persistence. It is desirable to simulate with a fully kinetic simulation the same length scales ($0.1 < L/\rho_s < 10$) used in the present work, a scale regime which is challenging to achieve with kinetic simulations of the present day.

A Critical Point and Flux-tube Selection on a Discrete Grid

In this appendix we give computational details for selecting critical points and flux-tube regions on a discrete grid. For more details on the methods and topological definitions described herein, see Rana (2004) for an overview, and Carr (2004); Carr et al. (2003) for an alternative method.

Critical points of a two-dimensional ψ field correspond to locations within a plasma with physical significance, and the flux-tube regions are defined in terms of the ψ field and the critical points only. Consequently, there are no external tuning parameters that define the flux-tube regions. The absence of tuning parameters is preferable to techniques that use threshold values to define significant regions, as the flux tubes are defined in terms of the physics of the system.

A.1 Critical Point Selection on a Discrete Grid

For a C^2 scalar field $\xi(x, y)$, the set of all *interior critical points of* ξ, S_{cp} is defined to be $S_{cp} = \{(x_0, y_0) \mid \nabla\xi|_{x_0,y_0} = 0\}$. This definition captures all local maxima (peaks), local minima (pits), and saddle points (passes). Together, the peaks and pits comprise the set of O points, and the set of all saddle points comprise the X points. The non-critical points in ξ are such that $\nabla\xi \neq 0$ and exist on the slopes of the two-dimensional ξ surface. We do not consider boundary critical points as we have doubly periodic BCs in our domain. It is possible to handle boundary critical points in a natural way, and omitting them in the discussion below is not limiting. See Rana (2004) and Carr (2004) for details.

Consider the set of all points ϵ_s around a saddle point s within a Euclidean distance $\epsilon > 0$ of s. Let $\epsilon_+ = \{x \in \epsilon_s \mid \xi(x) > \xi(s)\}$, and let $\epsilon_- = \{x \in \epsilon_s \mid \xi(x) < \xi(s)\}$. The sets ϵ_+ and ϵ_- partition ϵ_s into disjoint regions. In the limit $\epsilon \to 0$, ϵ_+ and ϵ_- are each the union of disjoint simply connected regions themselves. A saddle point has at least two ϵ_+ regions and at least two ϵ_- regions that alternate as one traverses these regions clockwise around s. A *Morse function* is one where all ϵ_+ and ϵ_- sets are comprised of 2 disjoint simply connected regions each. This excludes so-called monkey saddles from the domain, and removes complication from future analysis with little loss in generality. A *Morse saddle point* is a point at which two regions greater than the point meet, and simultaneously the point at which two regions less than the point meet.

When considering critical points on a discrete computational grid, complications arise from the loss of continuity when approximating the surface. A number of approaches to approximate the X and O points on a computational grid have been proposed (Rana, 2004), each with advantages and disadvantages. The primary consideration is how precise the approximate X and O point locations need to be. If it is possible to approximate the X and O points by their nearest grid location, then a significant simplification in the selection routine is possible. If one requires higher precision then it is necessary to interpolate between grid points to locate X and O points, with a commensurate increase in computational effort.

For our purposes, we take the computationally more efficient path and keep the X and O points "on the grid." The O points are easier to select computationally. A grid maxima O point is a grid location x_O such that $\xi(x_O) > \xi(x)$ for all x neighboring x_O, with grid minima O point defined analogously.

To define grid X points, consider the set of all immediate neighbors x_n to a grid point x_i. Let $\Delta x_n = x_n - x_i$ for all x_n neighbor points. Order the Δx_n points such that they are in clockwise order around x_i. Let N be the number of sign changes in the ordered Δx_ns. If $N = 4$, then x_i is classified as an X point.

This algorithmic formulation is a discretized means of finding the ϵ_+ and ϵ_- regions defined above.

Locating the critical points more precisely requires interpolation between grid points. One approach described in Rana (2004) considers a 4×4 or 6×6 patch centered on every cell in the grid. The patch is used to solve for a zero point within the cell domain, using bicubic interpolation or other interpolation schemes.

We choose to use grid critical points rather than interpolated critical points for the following reasons:

1. The error in the grid critical point loci is bounded by the grid point spacing, which is sufficient for the simulations presented here.

2. Critical points are located in regions where $|\nabla\xi| \sim 0$, and locating them requires the subtraction of values already near zero in absolute value. As such, these calculations are sensitive to loss of significant digits. In nearly flat regions, we find that interpolation-based methods often overlook critical points that grid-based methods find. Contrariwise, grid critical points often give a number of false positives, but these critical points are easily marked as such based on post-processing techniques.

3. Computational efficiency is paramount, as critical point identification is a central element of defining flux tubes. This favors the grid method.

4. Tracing the connections between critical points is simple, robust, and not prone to the difficulties of rounding errors as compared to the techniques required when tracing trajectories between grid points.

```
Input: Set of O points, X points and ξ[N] array
Output: Set of flux-tube regions
Let regions be an empty container;
foreach O point x_O do
    Let frontier be a priority queue;
    Let region be a set;
    frontier.enqueue(x_O, priority = ξ[x_O]);
    region.empty();
    while True do
        pt, val = frontier.dequeue();
        region.add(pt);
        if pt ∈ X points then
            break;
        end
        foreach neighbor nbr of pt do
            if nbr ∉ region and nbr ∉ frontier then
                frontier.enqueue(nbr, priority = ξ[nbr]);
            end
        end
        regions.add(region);
    end
    return regions
end
```

Algorithm 1: Flux-tube selection algorithm

A.2 Flux-Tube Selection on a Discrete Grid

For every grid O point, it is possible to associate with that point a simply connected region that delineates a flux tube with the O point at its center in ξ iso-contours. An algorithm for doing so is given in algorithm 1.

In algorithm 1, the $region$ set grows each iteration of the while loop. Each new addition is the next grid point in the $frontier$ priority queue that is nearest to $\xi[x_O]$ in value. The priority queue structure ensures that every time a grid point is removed from $frontier$ it is the grid point with the ξ value nearest $\xi[x_O]$. The while loop is terminated after the first X point is added to the $region$ set. During the while loop, the $region$ set always contains a simply connected set of points that includes the O point. Once the $region$ set expands to include the nearest X point in ξ contours, that delineates the entire flux-tube region.

Servidio et al. (2010) described a flux-tube selection algorithm that yields results essentially the same as algorithm 1. The critical points in that work were interpolated between grid points, but the results are the same. The algorithm in that work, however, requires many restarts and retries, as they do not employ a priority queue, but rather add neighboring points without ordering them in ξ values. The restarts are required when an X point is encountered that is closer in ξ value to $\xi[x_O]$ than the previously considered closest X point. The restarts ensure that their method considers each point multiple times before defining the flux tube region. The method described above requires no restarts and need consider each new point only once.

Armstrong, J. W., B. J. Rickett, and S. R. Spangler. 1995. Electron density power spectrum in the local interstellar medium. *Astrophysical Journal* 443(209).

Bale, S. D., P. J. Kellogg, F. S. Mozer, T. S. Horbury, and H. Reme. 2005. Measurement of the Electric Fluctuation Spectrum of Magnetohydrodynamic Turbulence. *Physical Review Letters* 94(215002).

Bender, C. M., and S. Orszag. 1978. *Advanced Mathematical Methods for Scientists and Engineers*. McGraw-Hill, Inc.

Binmore, K., and J. Davies. 2007. *Calculus: Concepts and Methods*, 190. Cambridge University Press.

Biskamp, D., and H. Welter. 1989. Dynamics of decaying two–dimensional magnetohydrodynamic turbulence. *Physics of Fluids B* 1(1964).

Boldyrev, S., and C. R. Gwinn. 2003a. Scintillations and Lévy Flights through the Interstallar Medium. *Astrophysical Journal* 584(791).

———. 2003b. Lévy Model for Interstellar Scintillations. *Physical Review Letters* 91(131101).

———. 2005. Radio-Wave Propagation in the Non-Gaussian Interstellar Medium. *Astrophysical Journal* 624(213).

Boldyrev, S., and A. Königl. 2006. Non-Gaussian Radio-Wave Scattering in the Interstellar Medium. *Astrophysical Journal* 640(344).

Canuto, C., M. Hussaini, A. Quarteroni, and T. Zang. 1990. *Spectral Methods in Fluid Dynamics*. Springer.

Carpenter, M. H., and C. A. Kennedy. 1994. Fourth-Order 2N-Storage Runge-Kutta Schemes. NASA Technical Memorandum 109112, NASA Langley Research Center.

Carr, H. 2004. Topological Manipulation of Isosurfaces. Ph.D. thesis, The University of British Columbia.

Carr, H., J. Snoeyink, and U. Axen. 2003. Computing contour trees in all dimensions. *Computational Geometry* 24(75).

Carter, T. A. 2006. Intermittent turbulence and turbulent structures in a linear magnetized plasma. *Physics of Plasmas* 13(010701).

Courant, R., K. Friedrichs, and H. Lewy. 1967. On the partial difference equations of mathematical physics. *IBM Journal* 215–234. English traslation of the 1928 German original.

Craddock, G. G., P. H. Diamond, and P. W. Terry. 1991. The observation of isolated long-lived current filaments in two-dimensional microtearing turbulence. *Physics of Fluids B* 3(304).

Fernandez, E., and P. W. Terry. 1997. Numerical measurement of turbulent responses in drift-Alfvén turbulence. *Physics of Plasmas* 4(2443).

Fernandez, E., P. W. Terry, and D. E. Newman. 1995. Energy partitions in saturated compressible electron magnetoturbulence. *Physics of Plasmas* 2(4204).

Ferrière, K. M. 2001. The interstellar environment of our galaxy. *Reviews of Modern Physics* 73(1031).

Frisch, U., P.-L. Sulem, and M. Nelkin. 1978. A simple dynamical model of intermittent fully developed turbulence. *Journal of Fluid Mechanics* 87(719).

Goertz, C. K. 1984. Kinetic Alfvén Waves on Auroral Field Lines. *Planetary and Space Science* 32(1387).

Goldreich, P., and S. Sridhar. 1995. Toward a theory of interstellar turbulence. 2: Strong Alfvénic turbulence. *Astrophysical Journal* 438(763).

Harmon, J. K., and W. A. Coles. 2005. Modeling radio scattering and scintillation observations of the inner solar wind using oblique Alfvén/ion cyclotron waves. *Journal of Geophysical Research* 110(A03101).

Haynes, A. L., and C. E. Parnell. 2010. A method for finding three-dimensional magnetic skeletons. *Physics of Plasmas* 17(092903).

Hazeltine, R. D. 1983. Reduced magnetohydrodynamics and the Hasegawa-Mima equation. *Physics of Fluids* 26(3242).

Hollweg, J. V. 1999. The Kinetic Alfvén Wave Revisited. *Journal of Geophysical Research* 104(14811).

Howes, G. G., S. C. Cowley, W. Dorland, G. W. Hammett, E. Quataert, and A. A. Schekochihin. 2006. Astrophysical Gyrokinetics: Basic Equations and Linear Theory. *Astrophysical Journal* 651(590).

Kinney, R., J. C. McWilliams, and T. Tajima. 1995. Coherent structures and turbulent cascades in two-dimensional incompressible magnetohydrodynamic turbulence. *Physics of Plasmas* 2(3623).

Kolmogorov, A. N. 1941. *C. R. Acad. Sci. U.R.S.S.* 30(301).

Laval, J-P., B. Dubrulle, and S. Nazarenko. 2001. Nonlocality and intermittency in three-dimensional turbulence. *Physics of Fluids* 13(1995).

Leamon, R. J., C. W. Smith, N. F. Ness, W. H. Matthaeus, and H. K. Wong. 1998. Observational constraints on the dynamics of the interplanetary magnetic field dissipation range. *Journal of Geophysical Research* 103(4775).

Lee, L. C., and J. R. Jokipii. 1975a. Strong scintillations in Astrophysics. I - The Markov approximation, its validity and application to angular broadening. *Astrophysical Journal* 196(695).

———. 1975b. Strong scintillations in Astrophysics. II - A theory of temporal broadening of pulses. *Astrophysical Journal* 201(532).

Lysak, R. L., and W. Lotko. 1996. On the kinetic dispersion relation for shear Alfvén waves. *Journal of Geophysical Research* 101(5085).

Marcus, P. S. 1988. Numerical simulation of Jupiter's Great Red Spot. *Nature* 331(693).

Marrelli, L., L. Frassinetti, P. Martin, D. Craig, and J. S. Sarff. 2005. Reduced intermittency in the magnetic turbulence of reversed field pinch plasmas. *Physics of Plasmas* 12(030701).

McWilliams, J. 1984. The emergence of isolated coherent vortices in turbulent flow. *Journal of Fluid Mechanics* 146(21).

Orszag, S. A. 1971. On the Elimination of Aliasing in Finite-Difference Schemes by Filtering High-Wavenumber Components. *Journal of the Atmospheric Sciences* 28(1074).

Politano, H., A. Pouquet, and P. L. Sulem. 1989. Inertial ranges and resistive instabilites in two-dimensional magnetohydrodynamic turbulence. *Physics of Fluids B* 1(2330).

Porteous, I. R. 1994. *Geometric Differentiation*. Cambridge University Press.

Rahman, H. O., and J. Weiland. 1983. Nonlinear coupling of drift waves, convective cells, and magnetic drift modes in finite-β plasmas. *Physical Review A* 28(1673).

Rana, S., ed. 2004. *Topological Data Structures for Surfaces*. Wiley.

Saito, S., S. P. Gary, and Y. Narita. 2010. Wavenumber spectrum of whistler turbulence: Particle-in-cell simulation. *Physics of Plasmas* 17(122316).

Schekochihin, A. A., S. C. Cowley, W. Dorland, G. W. Hammett, G. G. Howes, G. G. Plunk, E. Quataert, and T. Tatsuno. 2008. Gyrokinetic turbulence: a nonlinear route to dissipation through phase space. *Plasma Physics and Controlled Fusion* 50(124024).

Servidio, S., W. H. Matthaeus, M. A. Shay, P. Dmitruk, P. A. Cassak, and M. Wan. 2010. Statistics of magnetic reconnection in two-dimensional magnetohydrodynamic turbulence. *Physics of Plasmas* 17(032315).

She, Z. S., and E. Leveque. 1994. Universal Scaling Laws in Fully Developed Turbulence. *Physical Review Letters* 72(336).

Smith, K. W., and P. W. Terry. 2011. Damping of Electron Density Structures and Implications for Interstellar Scintillation. *Astrophysical Journal* 730(133).

Stéfant, Robert J. 1970. Alfvén Wave Damping from Finite Gyroradius Coupling to the Ion Acoustic Mode. *Physics of Fluids* 13(2).

Sutton, J. M. 1971. Scattering of pulsar radiation in the interstellar medium. *Monthly Notices of the Royal Astronomical Society* 155(51).

Terry, P. W. 1989. Two-timescale analysis of coherent vortex evolution in turbulence. *Physica D: Nonlinear Phenomena* 37(542).

———. 2000. Suppression of turbulence and transport by sheared flow. *Reviews of Modern Physics* 72(109).

Terry, P. W., E. Fernandez, and A. S. Ware. 1998. A Drift-Alfvén Model for Interstellar Turbulence. *Astrophysical Journal* 504(821).

Terry, P. W., C. McKay, and E. Fernandez. 2001. The role of electron density in magnetic turbulence. *Physics of Plasmas* 8(2707).

Terry, P. W., and K. W. Smith. 2007. Coherence and Intermittency of Electron Density in Small-Scale Interstellar Turbulence. *Astrophysical Journal* 665(402).

———. 2008. Intermittency of electron density in interstellar kinetic Alfvén wave turbulence. *Physics of Plasmas* 15(056502).

Waleffe, F. 1998. Three-Dimensional Coherent States in Plane Shear Flows. *Physical Review Letters* 81(4140).

———. 2003. Homotopy of exact coherent structures in plane shear flows. *Physics of Fluids* 15(1517).

Williamson, I. P. 1972. Pulse Broadening due to Multiple Scattering in the Interstellar Medium. *Monthly Notices of the Royal Astronomical Society* 157(55).

———. 1973. Pulse Broadening due to Multiple Scattering in the Interstellar Medium—II. *Monthly Notices of the Royal Astronomical Society* 163(345).

———. 1974. Pulse Broadening due to Multiple Scattering in the Interstellar Medium—III. *Monthly Notices of the Royal Astronomical Society* 166(499).

Yin, L., D. Winske, and W. Daughton. 2007. Kinetic Alfvén waves and electron physics. II. Oblique slow shocks. *Physics of Plasmas* 14(062105).